AN ABSTRACT OF THE DISSERTATION OF

Robyn L. Wangberg for the degree of Doctor of Philosophy in Physics presented on June 5, 2008.

Title: Sub-diffraction Light Propagation and Imaging in Planar Negative Refraction Waveguides

Abstract approved: _____

Viktor A. Podolskiy

In this dissertation we study the electromagnetic properties of planar waveguides with non-magnetic strongly anisotropic dielectric cores. We develop an analytical description of the mode propagation in these systems and show that the index of refraction can be either positive or negative depending on the specific material parameters. Propagating modes are supported even when the waveguide size is much smaller than the wavelength allowing light propagation and beam steering in micro- and nano-scale areas. We further demonstrate that it is possible to combine same-sized planar waveguide structures to build a planar lens. We determine the far-field resolution limit of such a lens and show that it is feasible to achieve resolution better than the free-space diffraction limit. For example, with incident light at the optical wavelength, $\lambda = 1.5\mu m$, we obtain an image with resolution $\Delta \approx 0.3\mu m$.

We further study the coupling to and from sub-wavelength planar waveguides of different sizes and compare the transmission through a negative-index structure to the behavior of positive index waveguides. We use numerical simulations to model electromagnetic wave propagation in arbitrary waveguide configurations. Included is a derivation of analyical expressions for the transmission and reflection coefficients along with a comparison of these expresssions to our numerical results. The extension of the planar lens is explored with three-dimensional imaging in chosen waveguide configurations with a focus on designing and optimizing planar-waveguide based beam-steering photonic devices. These results bring forth

applications including sub-diffraction planar lens imaging, photonic funnels, high-performance optical sensing, and all-optical computing.

Sub-diffraction Light Propagation and Imaging in Planar Negative Refraction Waveguides

by

Robyn L. Wangberg

A DISSERTATION

submitted to

Oregon State University

in partial fulfillment of
the requirements for the
degree of

Doctor of Philosophy

Presented June 5, 2008
Commencement June 2009

Doctor of Philosophy dissertation of Robyn L. Wangberg presented on June 5, 2008.

APPROVED:

Major Professor, representing Physics

Chair of the Department of Physics

Dean of the Graduate School

I understand that my dissertation will become part of the permanent collection of Oregon State University libraries. My signature below authorizes release of my dissertation to any reader upon request.

Robyn L. Wangberg, Author

ACKNOWLEDGEMENTS

I would like to sincerely thank my advisor, Prof. Viktor A. Podolskiy, for his honest advice, counsel, and contribution to this work. His dedication to the study of physics and his research is truly admirable. I also express gratitude for the mentoring guidance and support of Prof. Rubin Landau and Prof. Corinne Manogue throughout my graduate career. I also thank my research group and physics colleagues, especially Justin Elser, Sasha Govyadinov, Peter Sprunger, and Nicholas Kuhta for valuable discussions and collaborative learning.

Wholehearted appreciation is given to my family, whose endless faith, encouragement, and support provides me with the solace and confidence to achieve *all* of my goals, both scholastically and athletically. I am especially grateful for the constant love and support of my husband, Aaron. No one believes in me more and I could not have done this without him in my life, whether he was near or far.

This research was partially supported by American Chemical Society (ACS-PRF Grant No. 43924-G10), National Science Foundation (Grant No. ECCS-0724763), Office of Naval Research (Grant No. N00014-07-1-0457), Army Research Laboratory, and the Physics Department at Oregon State University.

TABLE OF CONTENTS

TABLE OF CONTENTS (Continued)

LIST OF FIGURES

LIST OF FIGURES (Continued)

LIST OF FIGURES (Continued)

Figure | Page

LIST OF TABLES

Chapter 1 – Introduction

In recent years, materials with a negative index of refraction have been researched extensively due to their physical realization using structured electromagnetic composite materials and their unusual interaction with electromagnetic waves. A negative refractive index is characteristic of materials for which both the dielectric permittivity and magnetic permeability are simultaneously negative. This distictive negative material property provides new physical phenomena such as reversed Snell's law, Cherenkov radiation, etc [2, 3] and the ability to enhance evanescent wave components [4]. Unique applications such as subwavelength imaging and planar lens design can be derived from a negative index of refraction [2, 5]. Negative index materials (NIMs) provide exciting opportunities for the field of photonics including applications for imaging and sensing devices, optical cloaking structures, and electro-plasmonic circuits [4, 6, 7, 8, 9, 10]. To actively engage in this promising class of materials and applications we study the electromagnetic properties of nanoscale[1] planar waveguides with non-magnetic strongly anisotropic dielectric cores in this dissertation. The index of refraction in these systems is shown to be either positive or negative depending on the material parameters. We primarily focus on the potential negative refractive index effects in order to design and optimize planar-waveguide based beam-steering photonic devices. The goal is to answer the fundamental question of coupling between micron-sized telecom fibers and nanoscale waveguides in order to make photonic circuits realizable.

The first chapter is an overview of negative index media including the fundamental differences between positive and negative index materials. We briefly discuss the discovery of some of the phenomena related to NIMs. We review the physics behind obtaining the essential simultaneous negative permittivity and negative permeability and the proposed manufactured solutions achieving these negative parameters as no naturally occuring material has been found to demonstrate

[1] Wavelength is the commonly used size scale unit in electrodynamics. The terms *nanoscale* refers to sizes much smaller than the optical wavelength ($\lambda \sim 1\mu m$) region while and *microns* to larger sizes. The descriptions, *nano* and *subwavelength* will be interchanged throughout this work when referring to optical systems.

them in the same frequency range. We explain how negative refraction provides opportunities for reversed physical effects and subwavelength imaging- novel imaging that surpasses the conventional *diffraction limit*. This common optical problem prevents the resolution of features in an image to better than the order of the a wavelength of incident radiation [11]. Due to the wave nature of light, focusing can only occur to a point as small as half the light wavelength by traditional methods. Thus, in order to obtain optical resolution below the wavelength of the light, this barrier, known as the Abbe barrier, must be surpassed [12]. It is this limited resolution of light that currently restricts the exciting optical field of photonic circuits. Optical circuits, which employ the use of light instead of electricity, provide the promise to advance the progress of electronic devices. Travelling massless light particles (photons) are much "faster" than the comparatively massive electrons, conceivably allowing faster information processing by a factor $\sim 10^6$ for visible light. Overheating is the major obstacle facing electronic circuits today optical circuits providing faster oscillations will also aid in eliminating that problem. The current limitation for optical elements is their size; they are currently on the order of microns (μm) for visible light, which is still two orders of magnitude bigger than the electronic circuits made today ($\sim 10nm$) [13, 14, 15, 16].

A particular realization of negative index materials are non-magnetic planar waveguides with anisotropic cores. Such a system is studied in detail in Chapter 3. These unique structures provide a new approach to producing a negative index material without needing a negative magnetic material response and are not limited by diffraction[2]. In the first part of this chapter we develop the analytical formalism to describe mode structure and propagation of light in these strongly anisotropic systems. Section 3.4 studies the effects related to finite conducting waveguide cladding on the modal structure and index of refraction inside the waveguide. Section 3.5 gives an analytical description of the electromagnetic properties of nanostructured metal-dielectric composites, including the nanolayered and nanowired metamaterials used for the numerical simulations of planar lens imaging presented in Section 3.6. These simulations demonstrate results using a low-loss, far-field, negative index planar lens that obtain image resolution better than the conventional free-space diffraction limit for $\lambda = 1.5\mu$m.

[2]As we will show in Chapter 3, the diffraction limit still applies to such waveguides but it is delayed rather than eliminated.

A practical extension of the proposed waveguide system is found in Chapter 4. We investigate the coupling to and from our subwavelength waveguide system with various sizes of surrounding waveguides and are motivated by the goal to find transmission through and reflection from the combined system. Section 4.1 presents the design of the numerical simulations employed to model electromagnetic wave propagation in arbitrary waveguide configurations. The case of multiple coupled waveguides is explored using the relaxation technique found in Section 4.3, including a comparison in the behavior between isotropic, positive index and anisotropic, negative index waveguides. The derivation of analytical expressions for the transmission and reflection coefficients is found in Section 4.2 along with a comparison of these expressions to our numerical results. Finally, we investigate the extension of the planar lens with imaging in chosen coupled waveguide configurations. Using imaging to focus light at the nanoscale aids in the ongoing pursuit for smaller and faster processors, sensors, and related devices.

Chapter 2 – Negative Index Media

This chapter overviews the physics and history of negative index materials starting with the electromagnetism basics involved. Section 2.2 explains what it means to have a negative electromagnetic response and reviews recent experiments performed to develop materials with this necessary response in various frequency ranges. Section 2.3 explains some of the unusual physics demonstrated by NIMs including reversed effects, imaging with NIM lenses, and experiments validating negative refraction in manufactured materials.

The same mathematical formalism is used throughout this dissertation. We model the electromagnetic wave in the proposed planar waveguide system as a series of *modes*. Choosing a single frequency $\omega = 2\pi c/\lambda_0$, where λ_0 is the vacuum wavelength, these modes can be written as,

$$\psi_l = C_l(\kappa_l) e^{i(k_y y + k_z z - i\omega t)} \tag{2.1}$$

where $C_l(\kappa_l)$ designates the structure of the mode in the x-direction and is a linear combination of $\cos(\kappa_l x)$ and $\sin(\kappa_l x)$ in the most general case. The modes are numbered by the κ parameter which is π times an integer multiple (depending on the symmetry of the mode) divided by the size of the waveguide[1]. Each individual mode is a solution to Maxwell's equations, which in Gaussian units are stated as,

$$\begin{aligned} \nabla \cdot \vec{D} &= 4\pi\rho \\ \nabla \cdot \vec{B} &= 0 \\ \nabla \times \vec{H} &= \frac{4\pi}{c}\vec{J} + \frac{1}{c}\frac{\partial \vec{D}}{\partial t} \\ \nabla \times \vec{E} &= -\frac{1}{c}\frac{\partial \vec{B}}{\partial t} \end{aligned} \tag{2.2}$$

With each mode satisfying these fundamental equations, the general solution for the electromagnetic fields can be represented as a linear combination of individual

[1]The κ parameter is described explicitly in Chapter 3.

modes (2.1) with coefficients calculated from boundary conditions using advanced numerical calculations involving delicate matrix manipulations.

In general, the electric field $\vec{E}$ and the magnetic flux density $\vec{B}$ are the basic vectors and $\vec{D}$ and $\vec{H}$ are obtained from them by adding the polarization $\vec{P}$ or subtracting the magnetization $\vec{M}$, respectively. If $\vec{P}$ and $\vec{M}$ are proportional to the applied field, then $\vec{D}$ and $\vec{B}$ are related to $\vec{E}$ and $\vec{H}$ through the material parameters; the dielectric constant $\overline{\epsilon}$ and the permeability $\overline{\mu}$.

$$\vec{D} = \overline{\epsilon}\vec{E} \tag{2.3}$$

$$\vec{B} = \overline{\mu}\vec{H}. \tag{2.4}$$

The tensors of dielectric permittivity ($\overline{\epsilon}$) and magnetic permeability ($\overline{\mu}$) describe the linear response and electromagnetic properties of the medium. The simplest case is for isotropic media, where the tensors are diagonal with three identical entries. In this case, the parameters can be replaced with scalars ϵ and μ.

Together, Eqs. (2.2, 2.3, 2.4) determine how electromagnetic waves propagate within a medium. These equations can be combined to obtain the electromagnetic wave equation,

$$\nabla^2\vec{E}(\vec{r},t) = \frac{\epsilon\mu}{c^2}\frac{\partial^2\vec{E}(\vec{r},t)}{\partial t^2}, \tag{2.5}$$

where $c = 2.9979 \times 10^{10} cm/s$ is the speed of light in a vacuum. Solutions of this equation are waves of the form; $\exp[i(\vec{k}\vec{x} - \omega t)]$. The phase velocity of the individual wave fronts is then given by $v_{ph} = \omega/k = c/n$ where n is the index of refraction of the material in which the wave propagates. From this one can easily derive the conventional index of refraction definition: the ratio of the speed of light to the speed of light in the material, $n = c/v_{ph}$. Putting the solutions back into Eq. 2.5 reveals the wave vector, $k = \pm\sqrt{\epsilon\mu}\omega/c$. Combining this with the definition of the phase velocity, the index of refraction is,

$$n = \pm\sqrt{\epsilon\mu}. \tag{2.6}$$

2.1 Left Handed versus Right Handed Media

All transparent or translucent materials that we know of possess a positive refractive index. Optical materials usually have a positive ϵ and μ so that the positive

$\sqrt{\epsilon\mu}$ is typically taken for n. It is interesting to consider the case where both ϵ and μ are negative and the negative sign is chosen for n. Following the simple analysis from Pendry [3]: if $\epsilon = -1$ and $\mu = -1$ are instead written as $\epsilon = \exp(i\pi)$ and $\mu = \exp(i\pi)$, then $n = \sqrt{\epsilon\mu} = \sqrt{(}\epsilon)\sqrt{(}\mu) = \exp(i\pi/2)\exp(i\pi/2) = \exp(i\pi) = -1$. Furthermore, if these materials are uniform, $\vec{k}, \vec{E}, \vec{H}$ form a left-handed set of vectors. Hence, these materials are referred to as "left-handed", because the wave vector, k, is antiparallel to the energy propagation of the wave determined by the Poynting vector, $\vec{S} = \vec{E} \times \vec{H}$. $\vec{S}$ always forms a right-handed cross product with the electric field and magnetic field even in left-handed materials. These materials are called left-handed materials (LHM), doubly negative materials (DNG), or negative index of refraction materials (NIM). We will primarily use the latter convention in this work to avoid confusion with the notation for optical chirality [17, 18]. NIMs also exhibit antiparallel phase, v_p and group, v_g velocities which we will discuss in detail in Sec 2.3.1.

Victor Veselago is known to first consider and predict the effects of lossless NIMs in his 1968 paper [2], but some concepts and phenomena related to materials with a negative refractive index were discovered as early as 1904. Horace Lamb (1904) and Henry Pocklington (1905) both found antiparallel phase and group velocities in mechanical systems [19, 20]. Near the same time, Arthur Schuster derived similar behavior in optical systems as well as the resulting negative refraction [21]. In the 1950's antiparallel energy flux and phase velocity were theoretically recognized by Dmitriy Sivukhin in materials with $\epsilon < 0$ and $\mu < 0$ although he noted that these materials were not known to exist [22].

2.2 Electromagnetic Material Response

The dielectric constant ϵ and magnetic permeability μ characterize the macroscopic response of a homogeneous material to applied electric and magnetic fields. Therefore, simultaneously negative values of ϵ and μ imply the material has a negative response to the driving field [3]. Conceptually one can use the Drude-Lorentz model visualize this response by picturing the material as harmonically bound electrons and magnetic moments, oscillating with frequency ω_0 in response to applied electromagnetic fields of the form, $\vec{E}(\vec{r}, t) = \vec{E}\exp(-i\omega t)$. First consider the bound electron resonant system as known in insulators; for frequencies

far below ω_0, a polarization is induced in the same direction as the applied field because the field displaces the electrons from the positive sites. As the frequency of the driving field is varied across the resonance frequency, the material polarization flips from in-phase to out-of-phase with the driving field, demonstrating a negative response. A negative magnetic response is achieved when the material response is due to harmonically bound magnetic moments [3].

Conductors can be viewed as insulators with charges free to move larger distances from the atoms where only the applied field frequency, ω, effects the material parameters (not the individual oscillator frequencies, ω_0). The Drude form for the dielectric function in metals responding to high frequencies (e.g. light) is dominated by the plasma-like response as described in Refs. [17, 23]. This form is given by,

$$\epsilon(\omega) = 1 - \frac{{\omega_{\rm pl}}^2}{\omega(\omega + i\,\tau)} \tag{2.7}$$

where τ represents the EM losses due to damping by a frictional force in the material and $\omega_{\rm pl}^2 = 4\pi(\frac{ne^2}{m_{eff}})$ is the definition of the effective plasma frequency. This electrostatic oscillation frequency is in response to a small charge separation. Here, e and m_{eff} are the charge and effective mass of the electron respectively, and n is the density of conduction electrons. Typical values for $\omega_{\rm pl}$ are on the order of several eV, and τ is small [23, 24]. Note that for $\omega < \omega_{\rm pl}$ the real part of the permittivity of the metal becomes negative. This occurs in the optical to GHz frequencies when using metals like Ag, Al, and Au, where the plasma frequency is on the order of 10 eV. The losses, given by ratio of the imaginary part of ϵ to the absolute value of the real part, are typically small in these spectral ranges [25].

To adhere with causality between the polarization and the applied electric field, NIM's must necessarily be both dispersive and absorptive. As in Eq. 2.7, their dielectric permittivity and magnetic permeability are generally complex functions of the frequency. It can be shown with the Kramers-Kronig relations that the real part of the dielectric function can be used to find the imaginary part and vice versa, connecting the dispersive and absorptive aspects of the process [23, 26]. Absorption of radiation in the material is directly related to the imaginary parts of $\epsilon(\omega)$ and $\mu(\omega)$. The material frequency dispersion is related primarily to the real part of ϵ and μ as seen in Eq. 2.7. There is no fundamental reason the real parts of ϵ and μ cannot be negative, however there is a restriction on the sign of

the imaginary parts. The imaginary parts of ϵ and μ must remain positive so that the total energy absorbed in a volume of the medium remains positive definite assuming the medium is dissipative, which we will assume in the remainder of this work [17, 27]. Causality, along with the possibility of materials with gain and the resulting signs of ϵ, μ, and n are further discussed in Section 2.3.1.

The fact that the negative response and the resulting negative material parameters happen near a resonance gives reason for why no naturally occurring material or compound has ever been demonstrated with negative values for both ϵ and μ in the same frequency range. Negative material parameters will vary as a function of frequency thus exhibiting frequency dispersion [2]. The frequency bandwidth for which negative materials transpire is relatively narrow compared to the positive material bandwidth. A negative electric response due to electric polarizations typically occurs at higher frequencies than for the magnetic counterpart. $\epsilon < 0$ is found rather easily at optical frequencies for metals like silver, gold, and aluminum, and in the terahertz to IR region for semiconductors and insulators. It is rare to achieve a natural negative magnetic response, but it is found in resonant ferromagnetic, ferromagnetic, and antiferromagnetic systems at a few hundred gigahertz. The fundamental processes causing the resonance and resulting negative magnetic polarization are either unpaired electron spins or orbital electron currents, both of which tend to occur at low frequencies, falling off toward the THz and IR range [3, 27].

Although overlapping negative material parameters are necessary to achieve a negative refractive index in uniform, isotropic materials, other natural materials can exhibit negative refraction without this requirement. For example, birefringent crystals with dielectric anisotropy display negative refraction at some incident angles [28], and at all angles with a strong enough anisotropy, having a negative permittivity in the direction transverse to the surface and positive in-plane permittivity [29]. However, the phase velocity remains in the same direction as the energy flux in birefringent materials so all attributes of a NIM are not obtained.

The revived interest in negative index materials led to the development of artificial materials, known as *metamaterials*, which have an electromagnetic response that is unachievable in conventional materials [30]. This class of inhomogenous materials was primarily developed as arrays of repeated subwavelength elements that possessed a strong response to applied electromagnetic fields. The inhomogeni-

eties, or size and spacing of the repeated elements, must have length scales smaller than the wavelength of the incident radiation. Typically, the size is 5 to 10 times smaller than the free-space wavelength. Then the incident radiation cannot distinguish the individual elements but rather reponds to the macroscopic features (ie. ϵ, μ) and resonances of the structure [3, 27, 31, 32]. Therefore global electromagnetic parameters can be used to describe the material. Some metamaterial designs are best described by effective-medium theory or derivations thereof [30, 33, 34]. Effective-medium theory (EMT) calculates the effective macroscopic properties for a medium based on its components and is a continuous approximation.

It is noteworthy to mention that the Kramers-Kronig relations mentioned above involve integrations over the frequency from negative infinity to infinity and the effective-medium theories will break down at high frequencies. This is especially important to realize when working with metamaterials because the scale of the structures is only one to two orders smaller than the wavelength. Thus, the homogenization of the metamaterials becomes invalid at the high frequency limit and care must be taken when evaluating the Kramers-Kronig integrals [27].

Metamaterials are different from other structured photonic materials such as photonic crystals or photonic band-gap materials that have been popularly used to produce negative refractive phenomenon [35, 36, 37]. Photonic crystals are a media with a periodic structure on dielectric or metallic body, usually produced by drilling or etching holes [3]. These structures are capable of achieving a negative phase velocity and therefore negative refraction. However, it is the multiple Bragg scattering in these periodic structures that produces the band-gaps and resulting negative refraction near the band edges [38, 39]. The periodicity of these structures is actually on the order of the incident radiation wavelength, therefore homogeneity is effectively lost and single values of the bulk parameters, ϵ and μ can not easily describe these media. The near-wavelength periodicity blurs the line between refraction and diffraction in experiments done with photonic crystals. Also, fabrication defects have a large impact on material performance, particulary for three-dimensional systems [27]. In the case of metamaterials, the periodicity is not as important and the properties depend mainly on single scatterer resonances so this paper will focus on those structures and not photonic band-gap materials. Specific designs and experiments demonstrating negative refraction using metamaterials will be discussed in Section 2.3.2.

2.2.1 Negative Dielectric Permittivity

It is easier to find materials with a negative dielectric permittivity than negative permeability so we will start with them. Some metals and plasmas already have a negative ϵ at optical frequencies because the conduction electrons can be assumed to be free in the background of static positive ion cores. This plasma-like behavior is reponsible for obtaining a negative permittivity at frequencies less than the plasma frequency as seen in Eq. 2.7. Above ω_p the medium behaves as a positive dielectric. This is the Drude-Lorentz model for dispersion in a plasma. For many metals, the plasma frequency is near ultraviolet frequencies and τ is small compared to ω_p, so they possess a negative ϵ at optical frequencies [24]. Because most metals have large dissipation, it is hard to extend this theory to lower frequencies where the dissipation dominates. It should be noted that for a band of frequencies above the resonance frequency, negative ϵ can be found in ordinary dielectrics with bound charges. Here the electrons are bound to positive nuclei and respond accordingly to an applied electric field. In effect, this adds a restoring force term to the equation of motion for an electron and leads to the Lorentz dielectric function,

$$\epsilon = 1 + \frac{\omega_p^2}{{\omega_0}^2 - \omega^2 - i\tau\omega}. \tag{2.8}$$

It is clearly seen that setting $\omega_0 = 0$, we obtain the Drude form for ϵ (Eq. 2.7). Now with a sharp enough resonance, the dielectric permittivity can be negative for a small frequency range above ω_0 [27].

Metal-dielectric composites have been studied extensively for their electromagnetic response [40]. When the wavelength of incident radiation is much larger than the length scales of the structures, effective medium theories can be used to describe these composite systems. Independently both Pendry *et. al.* [41, 42] and Sievenpiper *et. al.* [43] demonstrated that metallic wire-mesh structures have a low frequency stop band from zero frequency up to a cutoff frequency due to the movement of electrons in the metallic wires. A negative dielectric permittivity is thought to be the reason behind the low frequency stop band and provides a way to obtain negative ϵ at microwave frequencies [27]. The position and direction of the wires is important to consider because wires in only one direction will make the medium anisotropic with negative ϵ only for waves with their electric field in

that specific direction. An effective isotropic response can be acquired by placing a three-dimensional lattice of wires oriented along three orthogonal directions. In the limit of large wavelengths, the incoming light will not resolve the cubic symmetry and the medium appears to be isotropic, resulting in a true low-frequency plasma.

Pendry [3] proposed an array of wire elements with periodic cuts to achieve a negative ϵ metamaterial. Similar to the Drude-Lorentz model, the effective permittivity is given by,

$$\epsilon(\omega) = 1 - \frac{{\omega_p}^2 - {\omega_0}^2}{\omega^2 - {\omega_0}^2 + i\tau\omega}, \tag{2.9}$$

where the plasma frequency, ω_p, and the resonant frequency, ω_0, are determined by the geometry of the lattice rather than by the charge, effective mass, and density of electrons as is the case with the metals and plasmas described above. The dielectric permittivity is negative when $\omega_0 < \omega < \omega_p$, and since the resonant frequency can be set to almost any value in a metamaterial, this cut-wire medium can obtain negative ϵ at frequencies as low as a few megahertz.

2.2.2 Negative Permeability

A negative magnetic response is tougher to obtain as magnetic activity in most materials falls off for frequencies higher than a few gigahertz. A first consideration for obtaining the negative μ was the diamagnetic screening effect found in the response of a stack of metallic cylinders to an incident electromagnetic field. Percolation metallodielectric composites have also been used to produce a diamagnetic effective medium [40]. The problem with the cylinders is that the system only had an inductive response. Pendry uses the basic definition of a magnetic dipole moment, $\vec{m} = 1/2 \int \vec{r} \times \vec{j} d^3\vec{r}$, with current density $\vec{j}$, to prove that a magnetic response is achievable if current can be induced in closed loops [3]. Introducing a resonance (capacitative elements) at the same time will envoke a strong magnetic response and a possiblity of negative μ.

In 1999 Pendry and colleagues predicted magnetic metamaterials could be formed from a proposed variety of structures consisting of loops or tubes of conductors with a gap inserted (for illustration see Ref. [44]). These elements can be viewed as miniature circuits where a time-varying magnetic field polarized perpen-

dicular to the plane of the elements, induces an electromotive force in the plane, driving currents around the conductor. Charges accumulate at the gaps in the conductor, building up capacitance. This capacitance gives rise to a resonance with frequency like that of an LC circuit, $\omega_0 \sqrt{1/LC}$ where the inductance, L, is determined by the geometry of the element. These structures are known as split-ring resonators (SRR) and have been built with numerous designs [45, 46, 47]. The negative magnetic response occurs from the resonance. For frequencies far below ω_0 the currents in the conductor can keep up with the driving force caused by the external magnetic field producing a positive response. As the frequency of the applied field increases, the currents start to lag, resulting in an out-of-phase, negative response. The SRR can be thought of as the metamaterial version of a collection of magnetic atoms with an effective frequency-dependent magnetic permeability,

$$\mu(\omega) = 1 - \frac{F\omega^2}{\omega^2 - {\omega_0}^2 + i\omega\Gamma} \tag{2.10}$$

[3, 48].

The SSR systems were first successful in the GHz range, and are a viable solution for microwave frequencies, but are currently only scaled down to THz frequencies. These artificial materials, used in microwave experiments, are used to make an array of unit cells consisting of a SRR ($\mu < 0$) and a thin wire spanning the cell ($\epsilon < 0$) to yield a medium with $n < 0$. This repeated structure is designed to have a strong response to an applied electromagnetic field and has demonstrated negative refraction. However, the practical applications for NIMs are in the optical to infrared frequency ranges $(10^{13} - 10^{16})$ Hz. This is impossible to reach with present SRR designs because the size of the conductor tubes and gap would need to be on the order of 10 nanometers which is currently too small to build. Additionally, because the negative effective magnetic response of the SRR depends on the "bulk" conductivity of a metal they are predicted to break down at the higher optical and ultra-violet wavelengths when metals become transparent to light and no longer have the free-electron conductivity [48].

Negative magnetic permeability has been experimentally shown with several other structures. Another Pendry design is the double SRR [44]. This structure involves two subwavelength-sized concentric SRRs, facing opposite directions, which can be regarded as an LC circuit. The rings are considered as inductors and

the gaps as well as the space between the rings are the capacitive elements. Orienting a magnetic field perpendicular to the plane of the rings induces an opposing magnetic field in the loop due to Lenz's law. This diamagnetic response leads to negative real μ and the double SRR has been scaled to 1 THz. An alternative approach is to use a staple-structure facing a metallic mirror proposed by Zhang *et. al.* [49], pushing the resonant frequency range to 60 THz. Single SRRs have been shown to exhibit electric response at 85 THz and will provide a magnetic response in that frequency range as well [50].

In 2005, U-shaped structures were reportedly found by Enkrich to have a magnetic response at the telecommunications wavelength of 1.5 μm [51]. Lastly, Yuan *et. al.* used arrays of pairs of parallel silver strips demonstrated a negative magnetic response ($\mu' = -1.7$) in the red portion of the visible spectrum ($\lambda = 725$ nm) [52]. Asymmetric currents in the metal structures, induced by a perpendicular TM polarized light, give rise to this magnetic response. A strong resonance is required to get the desired negative magnetic response at higher frequencies. These systems therefore have significant resonance losses making them impractical for optical applications.

2.3 Predicted Physics in NIMs

Veselago was the first to publish a full report on negative refraction materials, bringing attention to the unusual physical properties exhibited in such materials. Examples of these properties include modified Snell's law of refraction, reversal of the Doppler shift, and inversed Cherenkov radiation [2]. Recently, left-handed materials have received much more attention as they have been manufactured and have actually demonstrated these exciting new physical phenomena for certain frequency ranges. Furthermore, in 2000, Sir Pendry demonstrated that negative index materials can be used to make planar lenses which do not fall subject to the conventional diffraction limit [4]. In this section these physical effects are explained and explored in detail.

2.3.1 Wave Propagation

Both ϵ and μ are analytic functions of the frequency, ω, with complex values. Together they determine the propagation of electromagnetic waves in the media they paramaterize. In particular, absorption and amplification in the media are accounted for with positive or negative imaginary parts of these parameters respectively. Here and below in this paper, we will use single and double prime ($'$; $''$) to denote the real and imaginary parts of complex numbers, respectively. Thus we can write, $\epsilon = \epsilon' + i\epsilon''$ and $\mu = \mu' + i\mu''$. A passive medium is absorbing (dissipative or lossy) and is characterized by a parameters $(|\epsilon|\mu'' + |\mu|\epsilon'') > 0$, whereas an active dielectric medium is said to have gain (amplifying) and has $(|\epsilon|\mu'' + |\mu|\epsilon'') < 0$ [53].

As discussed above, with both ϵ and μ negative in Maxwell's equations, the wave vector $\vec{k}$ has a reversed sign and is therefore opposite in direction to the Poynting vector. By definition, the group velocity of a wave with wave vector $\vec{k}$ is $\vec{v}_g = \frac{\partial\omega}{\partial\vec{k}}$. The group velocity is directly proportional to the Poynting vector, and thus conveys the energy of the wave as it describes the undistorted propagation of the wave pulse envelope through space [2, 26]. Therefore, in NIMs the phase velocity and group velocity are also antiparallel.

Considering all field components are proportional to the plane wave form $\exp[i(\vec{k}\vec{r} - \omega t)]$ and applying the second two Maxwell's equations in Eq. 2.2 we arrive at:

$$\begin{aligned} \vec{k} \times \vec{E} &= \frac{\omega}{c}\mu\vec{H} \\ \vec{k} \times \vec{H} &= -\frac{\omega}{c}\epsilon\vec{E} \end{aligned} \tag{2.11}$$

Defining the wave vector as, $\vec{k} = \frac{n\omega}{\hat{n}c}$, where $\hat{n}$ is the unit vector along $\vec{E} \times \vec{H}$, one can verify that the phase vector indeed has a reversed sign when $(\epsilon' < 0)$, and $(\mu' < 0)$, obtaining propagating waves with negative phase velocity. Since ϵ and μ appear as a product in Eq. 2.5, propagating solutions exist for two cases: when their signs are either both positive or both negative. Figure 2.3.1 shows the (ϵ')-(μ') plane with the behavior of the electromagnetic waves in each quadrant. Materials with $\epsilon' > 0, \mu' > 0$ fall in the first quadrant and support right-handed propagating waves with positive phase velocity. Materials with properties in the upper left, or second quadrant, are commonly found as electrical plasmas, metals in the UV

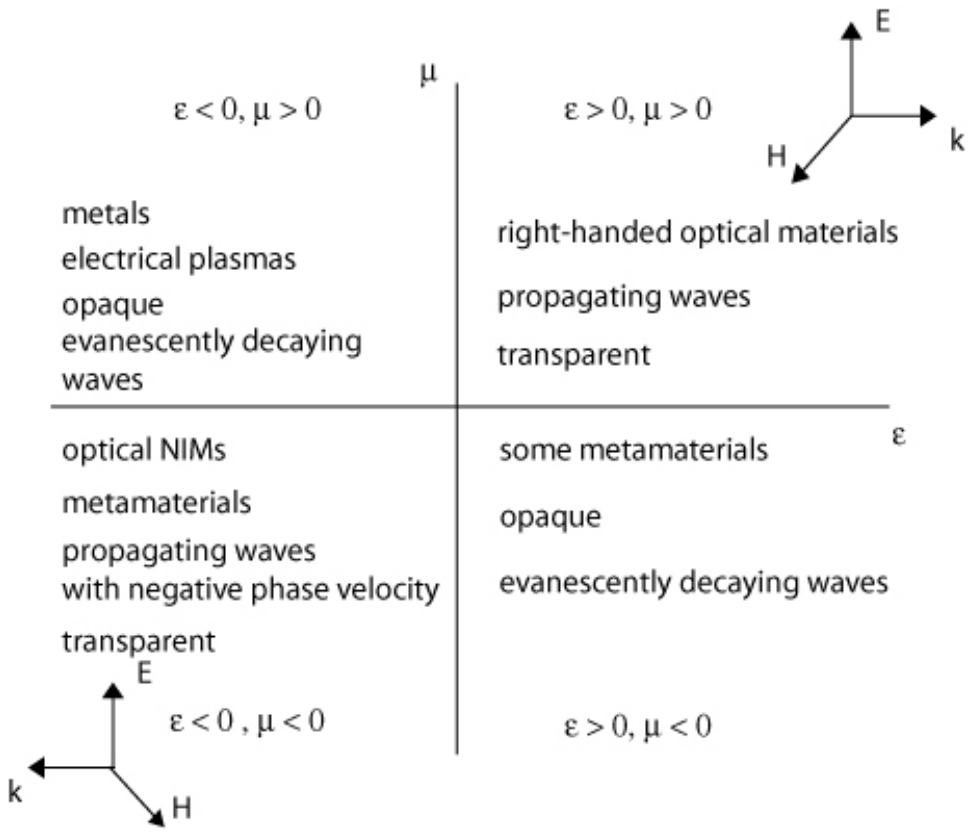

Figure 2.1: A schematic showing the categorization of materials based on the dielectric permittivity and magnetic permeability. The vector sets in the upper right and lower left show the right- and left-handed relationship between $\vec{E}$, $\vec{H}$, and $\vec{k}$.

to optical frequency ranges, and thin wire structures at GHz frequency. However, the electromagnetic waves evenescently decay in these media. Likewise, waves are also damped exponentially in media with parameters in the fourth quadrant. This quadrant classifies structured materials and some natural magnetic materials up to GHz frequency [2, 27]. The third quadrant is of interest as it includes NIM's, which allow propagating waves with a negative phase velocity. The right-handed and left-handed vector triad of $\left\langle \vec{E}, \vec{H}, \vec{k} \right\rangle$ is drawn for the quadrants with propagating waves.

Physically, an electromagnetic wave should decay in amplitude as it propagates in a dissipative medium, like a NIM, therefore we must ensure the correct sign for the propagating wave vector component. We start with the general wave vector

dispersion relation,

$$|\vec{k}|^2 = {k_x}^2 + {k_y}^2 + {k_z}^2 = \epsilon\mu\frac{\omega^2}{c^2}, \tag{2.12}$$

in an assumed homogenous media. Consider an electromagnetic plane wave with wave vector $\langle 0, k_y, k_z\rangle$ incident on an interface at $z = 0$ from a vacuum on the left in the region $(-\infty < z < 0)$ onto a medium with arbitrary ϵ and μ on the right in the region $(0 < z < \infty)$. k_y must be held constant across the interface while k_z is given by,

$$k_z^2 = \epsilon\mu\frac{\omega^2}{c^2} - k_y^2. \tag{2.13}$$

This material dispersion relates the phase velocity to the frequency, and can be used to determine the behavior of electromagnetic pulses in the material, such as attenuation and distortion. The sign of k_z in Eq. 2.13 cannot be determined from Maxwell's equations alone but must be selected to enforce the causality principle, or propagation away from the source. Mathematically, a branch cut in the complex plane for values of k_z^2 must be chosen carefully to describe the optical properties of the system. The behavior of the waves across this cut is discontinuous. To the right of the interface, if $(k_y^2 < Re[\epsilon\mu\omega^2/c^2])$ the waves are propagating and if $(k_y^2 > Re[\epsilon\mu\omega^2/c^2])$ the waves are evanescently decaying. Also, the medium on the right could be amplifying or absorbing depending on the sign of $\mathrm{Im}[\epsilon\mu]$. The treatment of causality for this situation has lead to much controversy [54, 55, 56, 57, 58]. Some argue to select the sign of k_z by enforcing a physically positive energy propagation [54, 56], but this is only physical in transparent materials. Single negative materials, with opposite signs of ϵ and μ reflect most of the incident radiation [26, 53]. Others propose a cut along the positive real axis $(0, \infty)$ which enforces the decay of waves away from the boundary in passive media [55, 59]. This is used when considering metals and dielectrics excited inside a geometry supporting total internal reflection. Regardless of the imaginary part of the dielectric permittivity (ϵ''), $\mathrm{Re}[k_z^2 < 0]$ implies propagating waves are not supported, and the field must exponentially decay away from the source, ie. $k_z'' > 0$ [60]. This branch cut is only valid for passive materials when the causality arguments are reduced. Similary, the cut along the negative real axis as proposed in [7, 54, 61, 62] is not physical for active media.

Rewriting the wave vector equation as $|n| = |\vec{k}|c/\omega$ reveals why the index of

refraction is an important optical property; it's magnitude directly relates the magnitude of the wave vector to the frequency, and therefore the phase velocity within the material [26, 53]. Govyadinov *et. al.* in Ref. [53] propose the simultaneous consideration of material transparency without losses or gains as well as a material in the state of absorption or gain. They assert that a cut in the complex k_z^2 plane will not satisfy all physical situations. There are four cases for an optical material to belong to: it has either a positive or negative refractive index, n', and radiation is either absorbed ($n'' > 0$) or amplified ($n'' < 0$). They claim that a single branch cut finding n from Eq. 2.6 is incorrect as it would limit the combinations of (n', n'') to only two. Therefore, they suggest considering $\sqrt{\epsilon}$ and $\sqrt{\mu}$ separately, cutting the complex plane along the negative imaginary axis for both parameters, and then calculating n as $\sqrt{\epsilon}\sqrt{\mu}$ [53, 60]. This universal approach adheres to causality and correctly determines the direction of wavevectors in optical metamaterials.

2.3.2 Negative Refraction

The most commonly discussed issue associated with a reversed wave vector is the refraction of radiation at an interface between a positive index material and a negative index material. To begin analysis of the passage of light through this interface, we review the boundary conditions derived from Maxwells equations (Eq. 2.2):

$$\begin{aligned} E_{\parallel_1} = E_{\parallel_2}, \qquad H_{\parallel_1} = H_{\parallel_2}, \\ \epsilon_1 E_{\perp 1} = \epsilon_2 E_{\perp 2}, \quad \mu_1 H_{\perp 1} = \mu_2 H_{\perp 2}, \end{aligned} \tag{2.14}$$

where subscript 1 refers to the positive index medium to the left of the interface, and 2 indicates the negative index medium on the right. These boundary conditions must be satisfied regardless of the sign of the index of refraction in the materials. Assume electromagnetic plane wave propagation in the (y, z) plane, with the interface located at $z = 0$ and the normal to the interface in the z-direction. The first two conditions in Eq. 2.14 disclose that the x and y components of the $\vec{E}$ and $\vec{H}$ fields maintain their direction in the refracted ray, independent of the sign of the index of refraction in the media. However, the z (normal) component of the refracted ray will change direction if there is a relative difference in the sign of n

between the two media. From the second set of equations in Eq. 2.14 it is obvious that $\vec{E}$ and $\vec{H}$ change magnitude from the first to second media, but their direction also reflects relative to the media interface. The same is true of $\vec{k}$ and this can be seen in the $\left\langle \vec{E}, \vec{H}, \vec{k} \right\rangle$ vector diagrams in quadrants I and III of Figure 2.3.1. In NIMs the save vector, $\vec{k}$, is directed toward the incident radiation, exactly opposite of $\vec{k}$ in a right-handed medium. Therefore it is understood that there is a negative phase velocity, meaning the phase decreases rather than advances as the wave passes through the medium [2, 3].

A direct consequence of negative refraction at the interface between a positive index material and negative index material is the reversal of the well-known Snell's law of refraction. Consider an electromagentic plane wave incident from a positive index medium with wave vector $\langle 0, k_y, k_z \rangle$ onto a NIM. The boundary conditions in Eq. 2.14 must be satisfied, meaning the fields must be continuous, hence the transmitted wave vector is $(0, k_y, -k_z)$. As mentioned above, the phase vector, $\vec{k}$, and the Poynting vector, $\vec{S}$, are antiparallel in NIMs, hence the refraction of the energy flow an electromagnetic wave at such an interface would be at the "wrong" side relative to the normal, bending away from the normal. This negative refraction angle is seen most easily in Snell's law,

$$n_1 \sin(\theta_1) = n_2 \sin(\theta_2), \tag{2.15}$$

where $n_2 < 0$ implying $\theta_2 < 0$ as well. This is in opposition to what is taught in conventional optics: that the refractive wave may bend very close to the normal, but will never cross it, regardless of how dense the second medium is. It is also noteworthy to mention that the reflected angle remains unaffected by the negative index of the second medium.

To demonstrate, Figure 2.3.2 shows numerical simulation results for the refraction of a mode in free space with the red, green, and blue arrows representing the energy propagation direction of incident, reflected, and refracted waves respectively in non-absorbing media. In (a) isotropic right-handed media is on both sides of the interface and the rays behave as expected for positive index materials. The schematic in (b) has a NIM on the right side of the interface and shows negative refraction.

Fresnel's formulas [26] are often used to find the amplitudes of the reflected

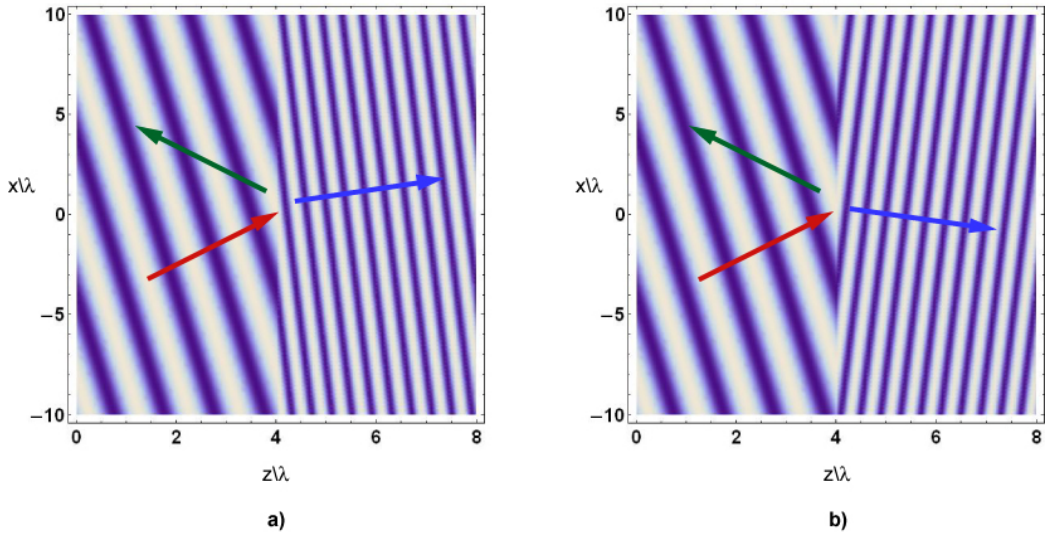

Figure 2.2: Exact numerical calculations of refraction of the mode in free space. In all schematics, the right-handed media ($z\lambda < 4$) has $\epsilon = \mu = 1$, the angle of incidence is $\pi/4$, and red, green, and blue arrows show the direction of incident, reflected, and refracted waves respectively. (a) Isotropic media with region 2 ($z\ /\lambda > 4$) having $\epsilon = 2.5$, $\mu = 2.5$. (b) NIM in region 2 ($z\ /\lambda > 4$) having $\epsilon = -2.5$, $\mu = -2.5$.

and refracted light, knowing the incident radiation at a boundary. These may still be used for the case of NIMs, but it is important to use the absolute values of ϵ, μ, n, θ, and φ to ensure correct answers. A unique and valuable outcome of negative refraction is a new type of optical lens formed with a planar slab of NIM, first proposed by Veselago [2]. We will discuss these planar lenses and imaging through them in Section 2.3.3.

2.3.2.1 Experiments

Now that we've covered how $\mathrm{Re}(\epsilon) < 0$ and $\mathrm{Re}(\mu) < 0$ were obtained using metamaterials, it is necessary and interesting to include a discussion on experiments performed to demonstrate negative refraction with these materials. Experimentally, the first thing to attempt was the demonstration and measurement of transmission through negative index materials. This was done by Shelby *et. al.* in 2001 using a two-dimensional isotropic split-ring NIM structure at microwave frequencies [63]. They performed numerical simulations and analytical transfer-matrix

calculations to verify their experimental transmission measurements. They concluded that it is appropriate to treat the NIM used as a homogenous material with material parameters having appropriate frequency dispersion. The next step was to experimentally verify some of the predicted phenomena of negative refraction media.

Snell's law is the primary basis for measuring the index of refraction directly. The first experiment revealing an actual negative index of refraction was also done by Shelby *et.al.* [47] in 2001. They measured the power refracted from a two-dimensional wedge of a metamaterial sample as a function of angle using microwave frequencies. The material consisted of a two-dimensional array of repeated unit cells of copper strips and split ring resonators on interlocking strips of standard circuit board material. Using Snell's law, they determined the effective n by measuring the scattering angle of the transmitted beam through a wedge of the metamaterial and confirmed that n is indeed given by $-\sqrt{\epsilon\mu}$ when both ϵ and μ are negative. In 2003 Houck *et.al.* at MIT [64] used composite wire and split-ring resonator prisms to measure transmitted two-dimensional profiles of microwave beams. Their transmission results obeyed Snell's law with negative refraction. They admitted the design of the materials was more complicated than they first thought as the composite material exhibited a large sensitivity to the electromagnetic environment, whereas the independent elements designed to obtain negative ϵ and μ did not. It was the discrete nature of the material which adversely affected transmission.

The first experiments demonstrating negative refraction scaled to the optical range were accomplished at almost the same time for pairs of metal rods and for the inverted system of pairs of dielectric voids in metals [61, 65]. Podolskiy *et. al.* first showed that the pairs of metal nanorods are not only capable of diamagnetic response but of obtaining a negative n' in the optical frequency range [62]. The negative response is due to an incident electromagnetic wave on the system. An alternating current parallel electric field causes currents producing the $-\epsilon$ due to resonant or off-resonant oscillations of the electrons in the metal. A magnetic field oriented perpendicular to the plane of the rods causes antiparallel currents in the rods yielding $-\mu$. The magnetic response is either dia- or paramagnetic depending on whether the wavelength of incident radiation is shorter or longer than the magnetic resonance of the coupled rods. The rods are thought of as equivalent

to inductors and gaps to capacitors, so the result is an LC circuit with a current loop at optical frequency. The performance of these structures is measured with a figure of merit, $F = |n'|/n''$, where $F > 1$ is considered high and is usually only obtained when both ϵ' and μ' are negative at the same frequency. An experiment performed in the optical range ($\lambda = 1.5$ μm) resulted in a refractive index with real part $n' = -0.3 \pm 0.1$ using a electron-beam-fabricated sample of paired rods [61]. F for this experiment was only 0.1 due to the large imaginary component of μ.

Another technique for NIM design is to use paired elliptically shaped voids in metal films with a dielectric between the films. This is essentially an inverse of the metal nanorod structure described above so the same idea of obtaining $-n$ can be applied. Typically, gold films are used with a dielectric between on the order of 100 nm. Zhang *et. al.* obtained a negative index of refraction for both circular voids and later for elliptical voids of $n' = -2.0$ and $n' = -4.0$ respectively [65, 66]. The wavelengths used were $\lambda = 1.8$ μm and $\lambda = 2.0$ μm with resulting figure of merits $F = 0.5$ and $F = 2.0$. Similar to the circular or ellipsoidal voids is the fishnet structure, proposed by Dolling, made with pairs of rectangular dielectric voids in parallel metal films. Here, the broader metal strips supporting asymmetric currents give rise to the negative permeability and the narrower metal strips, resembling wires, produce the negative permittivity [67]. The Karlsruhe-Iowa State group obtained the highest figure of merit for negative refractive index materials with $F = 3.0, n' = -1.0$ at $\lambda = 1.4$ μm [67].

2.3.2.2 Alternate Approaches for Obtaining Negative Refraction

The above approaches to designing negative index materials suffer from the limitations imposed by using resonant structures to produce the necessary negative electric and magnetic responses in the same frequency range. For desired optical region applications, low-loss systems using the above approaches are not practical due to the magnetic resonance involved. In addition, the metamaterials described in Section 2.2 are required to be as fine as possible so that incoming electromagnetic fields experience a homogeneous material and often do not achieve better than a 10:1 ratio of wavelength to structure size. Therefore, Pendry [68] suggests using chiral materials, which can exhibit negative refraction of one polarization with only a single resonance. Chiral materials have polarization-dependent refractive

indices. Introducing the chirality tensor, χ,

$$\chi = \begin{bmatrix} \chi_{EE} & \chi_{EH} \\ \chi_{HE} & \chi_{HH} \end{bmatrix} \tag{2.16}$$

the response of the medium to an electromagnetic field is given by:

$$\vec{D} = \chi_{EE}\vec{E} + \chi_{EH}\vec{H} \tag{2.17}$$

$$\vec{B} = \chi_{HE}\vec{E} + \chi_{HH}\vec{H}. \tag{2.18}$$

Pendry proposed a system with only a resonant band gap and chirality necessary to obtain negative refraction and suggested a practical realization for this structure [68]. Others have proposed a chiral material with gyrotropy for optical applications, [69, 70, 71], while Qiu *et al.* focus on chiral medium with magnetoelectric couplings to achieve the backward phase velocity present in NIMs [18]. Magnetoelectric materials have an electric field which may generate magnetization [33] and Qiu claims that even a material with a weak or non-existant magnetic response may exhibit negative index behavior. They theoretically demonstrate a negative phase velocity and/or negative refraction within specific frequency ranges in both isotropic and anisotropic magnetoelectric materials, resulting in a NIM without artificial magnetic materials or resonant permittivity and permeability.

The next chapter offers another approach to producing negative index materials using a non-magnetic anisotropic dielectric filling in a planar waveguide proposed by Podolskiy and Narimanov [1]. This design does not rely on any resonances for the negative electric and magnetic response, nor does it fall subject to fabrication defects like photonic crystals.

2.3.3 Imaging and Lenses

Conventional optical systems have a single optical axis, limited aperture, and fall subject to the diffraction limit. This fundamental law of physics prohibits the focusing of electromagnetic radiation onto an area smaller than a square light wavelength. Also, the positive refractive index of conventional optical lenses means that they need curved surfaces to form an image, and fall subject to spherical

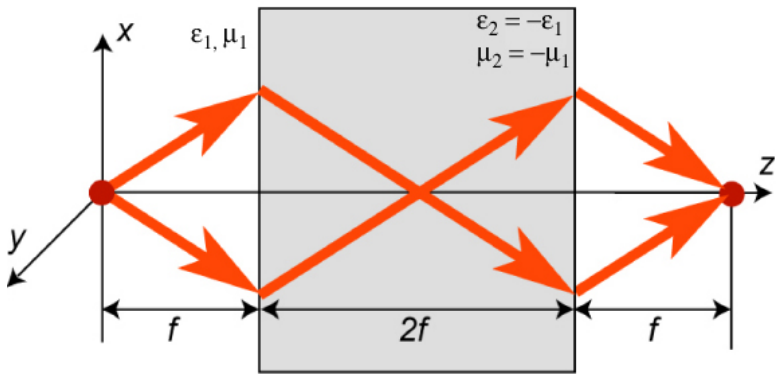

Figure 2.3: A symmetric planar NIM-based lens with two real foci outside and inside the slab. The source is placed a distance f to the left of the slab at the origin. The arrows depict the ray paths from the object to the image.

abberations. A negative index of refraction allows a flat slab of a material to behave as a lens and focus electromagnetic waves to produce a real image, known as a planar lens [2, 4]. A planar lens with a NIM, $\epsilon_2 = -\epsilon_1$, $\mu_2 = -\mu_1$, in the region acting as the lens does not have reflection from the interface as seen in Figure 2.3.3. It is noteworthy to mention that planar lenses can only focus the radiation from a point source at a point, and are not capable of focusing a collection of rays from infinity as conventional lenses can [2]. When one places a NIM inside actual concave and convex lenses, with the lenses placed in a vacuum, the traditional lensing effects are interchanged as concave lenses then converge the rays and convex lenses diverge.

Pendry was the first to predict and show the extraordinary consequence that negative refraction provides the possibility of a perfect lens, obtaining an image resolution that exceeds the traditional diffraction limit as all components of the source are restored [4]. This application is both exciting and controversial as sub-diffraction imaging has been shown to amplify the evanescent, non-propagating components of the radiation that are usually confined to the locality of the source, known as the near-field. As stated in Ref. [72], the spatial resolution of any monochromatic optical system can be related to its ability to restore the wave vector (k_y) spectrum emitted by the source. This spectrum contains two fundamentally different types of waves. The waves which propagate away from the source have $|k_y| < |n\omega|/c$. As the distance between the point of observation and the source is increased, the relative phase difference between these waves will increase. They

are known to carry the information about the commonly called "thick" features of the source with size $\geq \lambda/|2n|$, which can be reconstructed if the phase difference is reconciled. The other type of waves have $|k_y| \geq |n\omega|/c$, decay exponentially away from the source, and are known as evanescent waves. They contain the information about the "fine" sub-wavelength structure of the source, or features $\leq \lambda/|2n|$, and can be directly restored in the near-field only. The far-field reconstruction of these features is limited by the conventional diffraction limit. The defining boundary between propagating and evanescent waves depends on both wavelength, λ, and the index of refraction, n, of the material surrounding the source. Therefore it is possible to achieve subwavelength far-field resolution when materials with relatively large index of refraction are used and we will discuss this in Section 3.6 [25].

As Pendry states in Ref. [4] the evanescent waves decay in amplitude but not in phase as they fall away from the source, so it is their amplification that results in their transmission. Energy remains conserved because the evanescent waves do not propagate any energy. The amplification of these waves is due to their coupling with well-defined surface states existant on the NIM [27, 73, 74].

Electromagnetic resonant states or surface waves known as *surface plasmons* are supported in materials obeying Eq. 2.7 with a negative ϵ at UV to optical frequencies. These surface plasmons were first reported by Ritchie in 1957 and are the collective vibrations of an electron gas or plasma surrounding the atomic lattice sites of a metal. At a metal-dielectric interface, they are longitudinal modes whose fields decay exponentially into the metal and dielectric on either side, leaving a surviving charge density wave on the surface with wave vector,

$$k = \frac{\omega}{c}\sqrt{\frac{\epsilon_{metal}\epsilon_{dielectric}}{\epsilon_{metal} + \epsilon_{dielectric}}}, \tag{2.19}$$

where ω is the oscillation frequency and c is the speed of light [24]. Surface plasmons can be excited by both electrons and photons (light) but do require a coupling mechanism such as surface roughness, a grating structure, or a dielectric coupler because surface plasmons cannot be excited on a perfectly flat surface [24, 75]. By altering the structure of the metallic surface, one can control properties of surface plasmons, in particular their interaction with light, opening the potential for developing new types of photonic devices. This has led to a new field of photonics including miniaturized photonic circuits with length scales that are much

smaller than those currently achieved, data storage, light generation, microscopy, and subwavelength imaging [76].

A major advantage of using a planar lens is the lack of a necessary specific focal length per wavelength. The size of the system can be varied to optimize the image resolution, but it does not depended specifically on the exactly incident radiation wavelength. Additionally, these lenses have the near field capacity to excite short wavelengths. NIM lenses are also lighter, easier to make and have greater resolution in the near field [3].

Photonic crystals have been used to experimentally observe imaging through a flat slab of negative index material [36, 77]. Low material absorption is necessary along with all-angle negative refration in order to focus a diverging beam from a point source. Parmani *et. al.* obtained plane-wave negative refraction at specific incident angles and demonstrated it at microwave frequencies by using a metallic photonic crystal prism. The microwave point source had a frequency of 9.3 GHz (wavelength, 3.22 cm) was placed 2.25 cm from a two-dimensional flat lens made of a photonic crystal fabricated from an array of cylindrical alumina rods. They published images of their results and claimed that photonic crystals were key to this advanced observation because they have the necessary dispersion characteristics to achieve negative refraction over a wide range of angles [36].

Much work has been done researching imaging performed with lenses made of resonant-based, negative ϵ-negative μ, NIMs. Podolskiy *et. al.* have derived a resolution limit for the "real" absorbing NIM lens and demonstrated that the sub-diffraction imaging is limited to the near-field, while the far-field resolution gains no advantage over traditional optics [72]. They have also identified the optimal configuration for the near-field superlens, and have shown that even these lenses are impractical when the NIM absorption is greater than 30%. The absorption in the NIM is measured by the ratio of ϵ'' to ϵ' [78]. This limitation of NIM lenses along with a proposed solution of using non-magnetic NIMs to focus subwavelength signals in the far-field are discussed in further detail in Section 3.6.

2.3.4 Other Reversed Phenomena

Besides Snell's Law, there are a number of classical physical phenomena which are reversed in NIMs. The Doppler effect is one such phenomenon. Assuming a

stationary electromagnetic source with frequency, f_0 and a detector moving away from the source with velocity, v, the shifted frequency measured by the detector is given by,

$$f' = f_0 \frac{1 - nv/c}{1 + nv/c}, \tag{2.20}$$

where c is the speed of light [79]. In ordinary, right-handed materials the frequency is red-shifted or decreased as the distance between the object and the detector increases, ie. they are moving away from each other. Now suppose the detector is in a material with $-n$. This effectively inverts the fraction in Eq. 2.20, causing the shifted frequency to increase, or blue-shift, as the objects move further apart.

The Vavilov-Cerenkov radiation will also be reversed. Traditionally, this effect of emitted electromagnetic radiation occurs only when a charged particle passes through an insulating medium at a speed larger than the phase velocity of the electromagnetic fields with frequency ω following the relation, $v > \frac{c}{\sqrt{\epsilon(\omega)}}$ [26]. As the charged particle travels, the local electromagnetic field in the medium is distrupted. Electrons in the atoms of the medium will be displaced and polarized by the electromagetic field of the passing particle. After the disrupting particle has passed, photons are emitted as the insulator's electrons restore themselves to equilibrium. Usually, the photons interfere with each other destructively and no radiation is detected, but when the charged particle travels faster than light through the medium, the photons interfere constructively and radiation can be observed. The characteristic feature of the Cherenkov radiation is its angle of emission. Only at the specific angle θ, where $\cos(\theta) = \frac{c}{nv}$, does the constructive interference, and resulting cone shaped emission, occur. This angle is acute in conventional, right-handed materials, and the radiation interference is see by an observer at rest as a wavefront in the shape of a cone moving in the same direction of the particle. This is similar to the "shock" wave effect produced by supersonic aircrafts. However, for NIMs the angle is obtuse so that $\theta \rightarrow \pi - \theta$, and the Cherenkov cone of radiation will be directed backward relative to the moving charged particle [2]. Hence, the effect is reversed and the power is propagated backward. It has been mathematically shown that both backward *and* forward power propagation exist for different frequencies due to dispersion [80]. Also, a backward-pointing radiation cone has been experimentally demonstrated in photonic crystals [81].

2.4 Concluding Remarks

Negative refraction and left-handed materials are a subject of continued rising interest. The concept is counter intuitive and has provoked much controversy in recent years [82, 83, 84, 85]. The exploration of the controversies has provided a positive effect on the field as important ideas have been carefully examined and ironed out. This chapter has unfolded the fundamental concepts of negative index materials. We started by discussing the difference between right and left-handed media and how negative index materials can exist. In the following section we provide the background on different approaches to building negative index metamaterials, and describe several experiments done using these materials. Lastly we cover the new physical phenomena that NIMs provide access to, including negative refraction, reversed Doppler effect and Cherenkov radiation, and planar lenses and imaging. Imaging beyond the wavelength limit is a very exciting possiblity of NIMs, which we explore in details later in this work.

Practical applications of NIMs require low-loss materials, causing major concern with many of the current techniques used to build these materials. The problem lies in obtaining a negative dielectric permittivity and negative magnetic permeability in the same frequency range. Many current approaches rely heavily on resonance effects which have inherent losses affecting the resolution of the system. In the next chapter, we propose a new approach utilizing anisotropic metamaterials inside a planar waveguide to achieve a non-magnetic negative index material which is low-loss and scalable to a large range of frequencies. We report numerical simulation results which clarify some of the controversial issues, such a causality violation.

Chapter 3 – A Non-Magnetic Anisotropic Waveguide System

This chapter introduces a new approach to producing a negative index material using nonmagnetic anisotropic materials inside a planar waveguide. Sections 3.1-3.4 address waveguides with strongly anisotropic dielectric cores, introduce some of the unique properties of such structures, and consider the effects of *real* metallic waveguide walls. In particular, we explain the two types of modes which propagate in our system and introduce the nonmagnetic propagation constant, ν. We show that these anisotropic waveguides support propagating modes even when their size is much smaller than the wavelength and that the phase velocity of the propagating modes is negative. Section 3.5 reviews the fabrication approach of strongly anisotropic materials desired for the waveguide core. Finally, we reveal the practical application of far-field planar lens imaging through our system.

3.1 Geometry and Waveguide Propagation

The proposed unique negative-refraction system consists of a two-dimensional planar waveguide, with boundaries at $x = \pm d/2$, parallel to the (y, z) plane. Unbounded propagation is allowed in the y and z directions. We assume a homogeneous material inside the waveguide which is nonmagnetic, meaning $\mu = 1$, and has a uniaxial anisotropic dielectric constant. We have one dielectric constant in the x direction, $(\epsilon_x = \epsilon_\perp)$, along the optical axis, and one in the (y, z) plane, $(\epsilon_y = \epsilon_z = \epsilon_\parallel)$. The waveguide exterior may either be metal, air, or a dielectric. A schematic of the system is shown in Fig. 3.1 [1].

Two kinds of waveguide modes are supported in this system. The first kind of mode polarization is known as a transverse-electric (TE) wave, where the electric field vector is perpendicular to the optical axis and the propagation direction lies only in the (y, z) plane. The anisotropy has no effect on these waves as their propagation depends only on $\epsilon_\parallel$. The second kind of mode polarization is a transverse-magnetic (TM) wave, where the magnetic field vector is perpendicular to propagation, lying in the (y, z) plane, and has a vanishing component along the optical axis, whereas the electric field does not. The propagation of these elec-

tromagnetic waves is affected by both $\epsilon_{\|}$ and $\epsilon_{\perp}$. These waves, which "feel" the anisotropy, are essential for obtaining a negative index of refraction in our system. A helpful depiction of the modes in our system is demonstrated in Fig. 3.2 [1]. As we show further below, the TE and TM waves in our waveguide are fundamentally distinct as they have different dispersion relations and refraction properties. We are most concerned with the TM waveguide modes and the hybrid modes formed when the TE and TM modes mix. A planar waveguide with perfectly conducting walls may also support a transverse electromagnetic wave (TEM mode), where both field components are transverse to the direction of propagation [26]. We do not consider such modes here because they do not couple to the TE or TM modes and they are not supported in our left-handed system.

A linear combination of the TE and TM modes can represent any electromagnetic wave propagating in the system. The $\{x, y, z\}$ components of TE $(E^{(TE)}, H^{(TE)})$, and TM $(E^{(TM)}, H^{(TM)})$ waves propagating in (y, z) direction can be represented by the following expressions:

$$
\begin{aligned}
E^{(TM)} &= \left\{ i\frac{k_z^{(TM)^2} + k_y^{(TM)^2}}{k_z^{(TM)}\varkappa^{(TM)^2}}\frac{\epsilon_{||}}{\epsilon_{\perp}}E_0^{(TM)\prime};\ \frac{k_y^{(TM)}}{k_z^{(TM)}}E_0^{(TM)};\ E_0^{(TM)} \right\} \\
H^{(TM)} &= \left\{ 0;\ i\frac{k\epsilon_{||}}{\varkappa^{(TM)^2}}E_0^{(TM)\prime};\ -i\frac{kk_y^{(TM)}\epsilon_{||}}{k_z^{(TM)}\varkappa^{(TM)^2}}E_0^{(TM)\prime} \right\} \\
E^{(TE)} &= \left\{ 0;\ E_0^{(TE)};\ -\frac{k_y^{(TE)}}{k_z^{(TE)}}E_0^{(TE)} \right\} \\
H^{(TE)} &= \left\{ -\frac{k_z^{(TE)^2} + k_y^{(TE)^2}}{kk_z^{(TE)}}E_0^{(TE)};\ -\frac{ik_y^{(TE)}}{kk_z^{(TE)}}E_0^{(TE)\prime};\ -\frac{i}{k}E_0^{(TE)\prime} \right\}
\end{aligned}
\tag{3.1}
$$

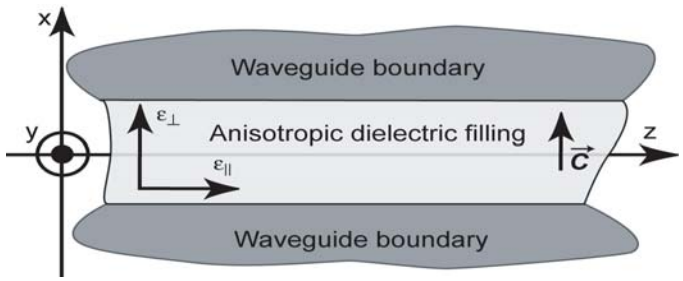

Figure 3.1: Illustration of our nonmagnetic negative-refraction system

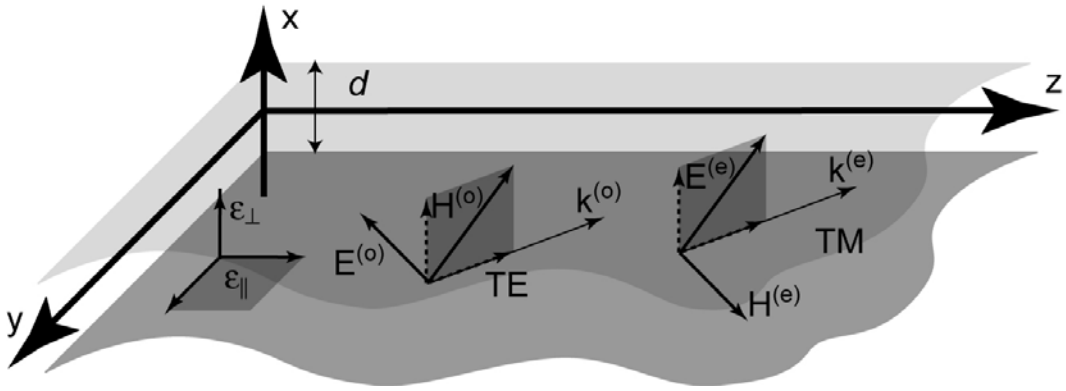

Figure 3.2: System schematic showing how TE and TM modes propagate through the planar waveguide with anisotropic core.

where $k = \omega/c$, and prime ($'$) denotes the differentiation with respect to x. The field $E_0^{(TM|TE)}(x, y, z; t) = E_0^{(TM|TE)}(x)e^{-i\omega t + ik_y^{(TM|TE)}y + ik_z^{(TM|TE)}z}$ is defined from the wave equation resembling that in Ref. [17],

$$E_0^{(TM|TE)''} + \varkappa^{(TM|TE)^2} E_0^{(TM|TE)} = 0. \tag{3.2}$$

Eq. 3.2 satisfies the conventional boundary condition for tangential (y, z) components of the electric field to vanish at the waveguide walls. The above field equations can be verified outright using Maxwell's Equations [1].

To begin understanding wave propagation inside the proposed waveguide, we will consider the case of perfectly conducting waveguide walls and extend this theory to finite conducting boundaries in Section 3.4. In the ideal, perfectly conducting wall case, the energy of the electromagnetic waves is confined to the core of the waveguide. The wave equation (Eq. 3.2) produces a series of symmetric and antisymmetric mode solutions for the x dependence of the fields, $E_0^{(TM|TE)}(x)$. The symmetric modes are of the form $\cos(\varkappa x)$ with $\varkappa = (2j+1)\pi/d$, while the asymmetric modes are of the form $\sin(\varkappa x)$ with $\varkappa = 2j\pi/d$, where j is an integer mode number in both cases. The standing wave structure of the waveguide mode in the x direction is disclosed by $\varkappa$, which in this case only depends on the waveguide thickness, d, and mode number, j, and is completely independent of the dieletric properties of the core. Thus, the $\varkappa$ mode parameter scales as the inverse confinement length of the mode in the x direction and has the same dimension as the wave vector, k. It is actually independent of the TE or TM waveguide mode

polarization.

From Ref. [1], each waveguide mode has its own dispersion relation given by:

$$TM: \quad \frac{{k_x}^2}{\epsilon_{||}} + \frac{{k_y}^2 + {k_z}^{(TM)^2}}{\epsilon_\perp} = k^2 = \frac{\omega^2}{c^2}, \tag{3.3}$$

$$TE: \quad \frac{{k_x}^2}{\epsilon_{||}} + \frac{{k_y}^2 + {k_z}^{(TE)^2}}{\epsilon_{||}} = k^2 = \frac{\omega^2}{c^2}. \tag{3.4}$$

Starting from the dispersion relation for the TM mode (Eq. 3.3) in an anisotropic, non-magnetic ($\mu = 1$) uniaxial crystal, with the x axis defined as the optical axis, as found in Ref. [86], we can derive the mode-dependant equivalent dispersion relation for our two-dimensional wave propagating system. Recall that we only have travelling waves in the y and z directions, so we include the x dependence by replacing k_x with $\varkappa$. Rearranging terms and factoring out $k^2 = \frac{\omega^2}{c^2}$ we have,

$$k_z^{(TM)^2} + {k_y}^2 = \epsilon_\perp k^2 \left(1 - \frac{\varkappa^2 c^2}{\epsilon_{||}\omega^2}\right), \tag{3.5}$$

with a similar version for the TE mode using $\epsilon_{||}$ instead of $\epsilon_\perp$. Now the TM wave equation can be rewritten introducing a new propagation parameter, ν to include the x dependence,

$${k_z}^{(TM)^2} + {k_y}^2 = \epsilon_\perp \nu k^2, \tag{3.6}$$

where

$$\nu = 1 - \frac{\varkappa^2}{\epsilon_{||} k^2} \tag{3.7}$$

Note the resemblance here between the new propagation constant, ν, and the magnetic permeability, μ, from the free space dispersion relation, $k_x^2 + k_y^2 + k_z^2 = \epsilon\mu k^2$. Just as the case of a free space plane wave, the refractive index is a product of two mode-specific scalar constants, now ϵ and ν [1]. The ϵ used depends on the given mode; $\epsilon_{||}$ is used for TE modes and $\epsilon_\perp$ for TM modes. Thus depending on the waveguide mode, our effective index of refraction is defined as,

$$n^{(TM)} = \pm\sqrt{\epsilon_\perp \nu} \tag{3.8}$$

$$n^{(TE)} = \pm\sqrt{\epsilon_\parallel \nu} \tag{3.9}$$

The TM and TE modes presented here deviate from those of the conventional waveguide found in common textbooks [17, 26]. The difference lies in the geometry of the system. Our planar waveguide with anisotropic core is unbounded in the two-dimensional (y, z) plane, versus the isotropic cylindrical (1D) waveguide, which has wave propagation only in the z direction. The traditional TE and TM mode solutions can be found directly as a linear combination of the fields in Eq. 3.1.

As mentioned before, an arbitrary wave inside a planar waveguide can be represented as a linear combination of waveguide modes, each with a different value of $\varkappa$. For the rest of this paper we limit ourselves to the case when only a single mode is excited initially. This assumption does not restrict the generality of our approach since (i) it does not limit (y, z) structure of the solutions or their polarization and (ii) different modes of the waveguide do not couple to each other. The expressions recounted here can easily be generalized for the multimode case [1].

3.2 Strongly Anisotropic Systems

We must now consider all possible solutions for our system depending on the sign of the ϵ and ν parameters. Knowing that imaginary values of the wave vector (k) components correspond to attenuating waves, we need real values for k_y and k_z to ensure propagation in the waveguide. This is only possible when ϵ and ν are of the same sign. The typical, transmitting, isotropic waveguide is described when both parameters are positive, $(\epsilon > 0;\ \nu > 0)$. The case of $\epsilon < 0;\ \nu > 0$ corresponds to a waveguide with a metallic core, which does not support propagating modes. The reverse case, when $\epsilon > 0$ and $\nu < 0$ demonstrates a so-called subcritical waveguide, which reflects all incoming radiation and again does not support propagating waves [1, 87]. Similar to light transmission through a thin metallic film, an exponentially small portion of radiation can penetrate into a finite-sized subcritical waveguide [88].

Our interest in producing a negative index material, gives explanation for the focus of this paper being on the case of negative values for both $\epsilon_\perp$ and ν. This case

is realized only for the TM waveguide mode in anisotropic material, as the TE mode will decay exponentially in such a waveguide. It should be noted that there are various sign combinations of $\epsilon_\perp$ and $\epsilon_\parallel$ for which TM modes exist and propagate in a waveguide. The only combination where TM mode propagation ceases is when $\epsilon_\perp < 0; \epsilon_\parallel < 0$. The reverse combination where both constants are positive, $(\epsilon_\perp > 0; \epsilon_\parallel > 0)$, gives a right-handed waveguide, which is isotropic if $\epsilon_\perp = \epsilon_\parallel$. When either $\epsilon_\perp$ or $\epsilon_\parallel$ is negative with the other positive the dispersion relation describes a hyperbola. In particular, when $\epsilon_\perp < 0$ and $\epsilon_\parallel > 0$, the hyperbolic curve is such that the energy flux in the core is antiparallel to the wave vector, meaning there is a negative index of refraction [86]. We specifically need the case of $\epsilon_\perp < 0$ and $\epsilon_\parallel > 0$ to obtain a negative ν value as seen in Eq. 3.7.

Figure 3.2 shows the absolute value of the real part of the wave vector, k_z as a function of waveguide size for the three propagating cases of $\epsilon_\parallel; \epsilon_\perp$ combinations. The solid, blue line corresponds to the isotropic conventional waveguide and demonstrates the "cut-off" size below which no propagation occurs. The remaining combinations are strongly anisotropic systems with either $n > 0$ or $n < 0$ and both support deep sub-wavelength wave propagation. The green, dashed-dot line refers to the case of a positive index of refraction $(\epsilon_\parallel < 0; \epsilon_\perp > 0)$ and is realized with photonic funnels as in Ref. [88]. Govyadinov and Podolskiy use a tapered cylindrical waveguide with a photonic crystal core to compress and propagate TM light waves below the free-space diffraction limit. As the radius of the waveguide is decreased, the internal wavelength $\lambda/|n|$ also decreases thus effectively removing the diffraction limit. Our negative index waveguide system with $\epsilon_\parallel > 0; \epsilon_\perp < 0$ is described by the red, dashed line and actually has a "cut-on" radius for energy propagation, where propagation does not occur for waveguide sizes on the order of the incident wavelength but does for deep subwavelength sizes. This size restriction comes from the requirement that ν must be negative to obtain a negative index of refraction.

3.3 Negative Phase Velocity

As mentioned in Section 2.3.1, another important characteristic of having a negative index material is the resulting negative phase velocity of the electromagnetic wave inside the material. According to common textbooks, [17, 26], the phase

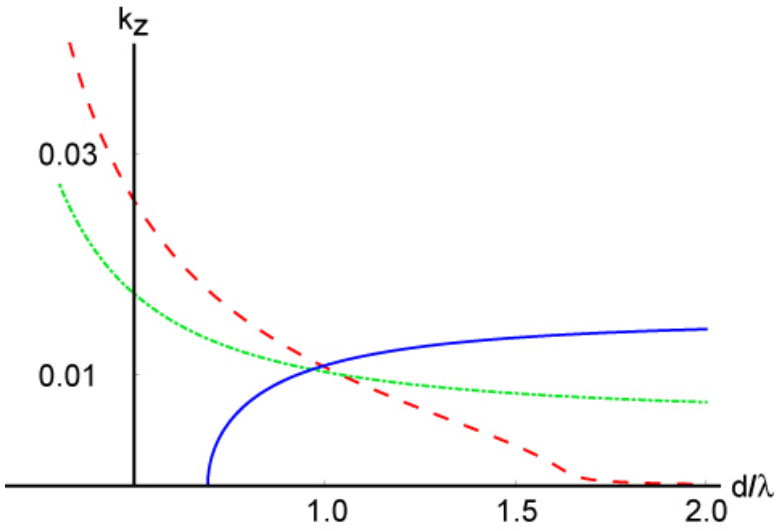

Figure 3.3: Mode propagation in several waveguides. The absolute values of the real parts of the wave vector are shown as a function of waveguide size. The blue (solid) line is for the conventional isotropic waveguide, the green (dashed-dot) line is for the anisotropic photonic crystal core, and the red (dashed) line is for our anisotropic negative index system.

velocity of a travelling wave is defined as,

$$v_p = \omega(k)k = \frac{c}{n(k)}. \tag{3.10}$$

From Eq. 3.10 the negative phase velocity of the propagating wave is easily illustrated since we choose a negative index of refraction in Eq. 3.8 from reasons explained in Sec. 2.3.2. It is this negative phase velocity that enables planar imaging which will be discussed at length later in this chapter.

The negative phase velocity can also be directly derived starting from the definition of the Poynting vector, $\mathbf{S} = \frac{c}{4\pi}[\mathbf{E}\times\mathbf{H}]$ [26]. In the proposed system we select the normal-incidence, propagating, z component of the TM-polarized wave, and assume a symmetric mode solution of the fields so that $E_0^{(TM|TE)}(x) = \cos(\varkappa x)$. The TM mode wave vector is given by,

$$\frac{{k_\perp}^2}{\epsilon_\parallel} + \frac{{k_\parallel}^2}{\epsilon_\perp} = \frac{\omega^2}{c^2} \tag{3.11}$$

The TE mode wave vector is given by,

$$\frac{{k_\perp}^2 + {k_\parallel}^2}{\epsilon_\parallel} = \frac{\omega^2}{c^2} \tag{3.12}$$

The resulting Poynting vector for the TM mode is:

$$S_{TM} = \frac{c^2}{4\pi\omega}\left[\frac{k_\perp}{\epsilon_\parallel}, \frac{k_\parallel}{\epsilon_\perp}, \frac{k_\parallel}{\epsilon_\perp}\right] \tag{3.13}$$

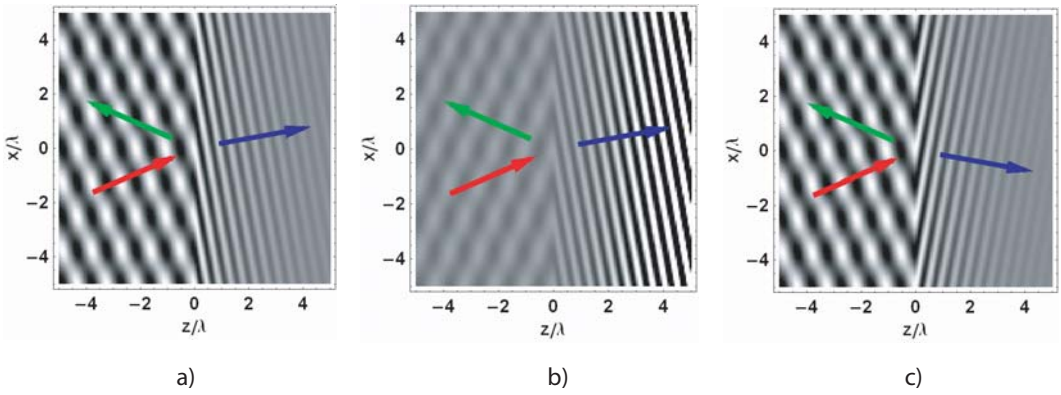

Figure 3.4: Exact numerical calculations of refraction of the mode in a planar waveguide with perfectly conducting walls done by Podolskiy [1]; $\varkappa = k/2$. In all schematics, the right-handed media ($z < 0$) has $\epsilon = \mu = 1/2 + 0.0002i$, the angle of incidence is $\pi/10$, and red, green, and blue arrows show the direction of incident, reflected, and refracted waves respectively. (a) Isotropic media with region 2 ($z > 0$) having $\epsilon = 5$, $\mu = 1$. (b) and (c) NIM in region 2 ($z > 0$) having $\epsilon = 5 + 0.1i$, $\mu = -1$. (b) Positive refraction but an unphysical situation to have the intensity increase in lossy media. (c) Negative refraction with correct physics; attenuation of intensity over distance.

Thus for the TM wave in the proposed system, where $\epsilon_\perp < 0$ and $\epsilon_\parallel > 0$, the Poynting vector is not parallel to the wave vector. Note from Eq. 3.13 that $S_\parallel$ is antiparallel to $k_\parallel$ and this is the reason for negative refraction in the system. To demonstrate, Figure 3.3 shows numerical simulation results for the refraction of a mode in a planar waveguide with perfectly conducting walls for three cases with the red, green, and blue arrows representing the energy propagation direction of incident, reflected, and refracted waves respectively. In (a) isotropic right-handed media is on both sides of the interface and the rays behave as expected for positive index materials. The schmatics in (b) and (c) assume an absorbing ($\epsilon'' = \mu'' > 0$) NIM in the positive z/λ region and reveal the only two possible refracted ray solutions which satisfy the boundary conditions (Eq. 2.14). The solution in (b)

has positive refraction but is not physical because the intensity increases with distance in an inherently lossy medium. Thus, (c) is the correct solution satisfying the boundary conditions with negative refraction and attenuation of wave intensity over distance.

The Poynting vector can then be simplified using Eqs. 3.1 to:

$$S_z^{(TM)} = \frac{c}{4\pi}\frac{k_z}{\epsilon_\perp}\frac{k}{\kappa^2}\epsilon_{||}^2 \sin(\kappa x)^2 \tag{3.14}$$

Note that the z component of the Poynting vector must be a positive value as it denotes energy flux. We can therefore determine the sign of k_z to be negative, since k, κ, $\sin^2$, and $\epsilon_{\|}$ are all positive values, and $\epsilon_\perp$ is negative in our system. This negative k_z indicates the negative phase velocity of the wave, antiparallel to the energy flux and group velocity, which in turn leads to the interesting behavior demonstrated by negative index materials. For the proposed system, this condition holds only for the TM wave with the condition of extreme anisotropy of the electric permittivity of the core material, as mentioned above.

3.4 Effect of Finite Wall Conductance

In practice, the materials used to build these waveguide walls will not have perfect, infinite conductivity, so here we determine the effect of finite metallic wall conductance on the waveguide properties, including the mode structure, ν parameter, and index of refraction. One can start by deriving the structure of the modes in the system using a perturbation approach on the case of perfectly conducting walls. Recall that the z component of the field depends on the x coordinate with $\cos(\kappa x)$ or $\sin(\kappa x)$ behavior based on the symmetry of the modes. We assume an exponential dependence of the field inside the metallic walls, $\exp(-\gamma x)$, where $-\gamma$ is the inverse of the skin depth and measures how far the wave penetrates into the metal [79]. As the fields inside the waveguide attenuate, we match the in-plane (y, z) field components throughout the $x = \pm d/2$ planes to satisfy the conventional electromagnetic boundary conditions assuming no surface charge or surface current [17, 26],

$$\begin{aligned} \hat{n} \times (\vec{E} - \vec{E}_m) &= 0, \\ \hat{n} \cdot (\epsilon_{\|}\vec{E} - \epsilon_m\vec{E}_m) &= 0, \\ \hat{n} \times (\vec{H} - \vec{H}_m) &= 0, \\ \hat{n} \cdot (\vec{B} - \vec{B}_m) &= 0. \end{aligned} \tag{3.15}$$

We then combine the dispersion relations for our waveguide modes (Eqs. 3.5) and the mode in the metal to solve for γ in terms of know variables, $\epsilon_{\|}$, ϵ_m, k, and $\varkappa$,

$$\gamma^{(0)} = \pm\sqrt{k^2(\epsilon_{\|} - \epsilon_m) - \varkappa^{(0)2}}. \tag{3.16}$$

Since we require the wave to decay inside the walls, we assign the positive sign for defining γ. Presuming a symmetric (cos) waveguide mode, we only have to consider a single boundary when satisfying the boundary conditions above. Using only the first and third conditions in Eq. 3.15, along with our γ definition, leads to the relationships in Eq. 3.17 for TM and TE modes respectively. These equations give the exact value of the mode parameter, $\varkappa$, for each type of mode within our planar waveguide made of finite metallic conducting walls. For highly conductive metals, at near-IR to THz frequencies, the physical mode structure changes little [25].

$$\begin{aligned} TM : \tan\left(\frac{\varkappa^{(TM)}d}{2}\right) &= -\frac{\epsilon_m\varkappa^{(TM)}}{\sqrt{\mathrm{k}^2\epsilon_{\|}^2(\epsilon_{\perp} - \epsilon_m) - \varkappa^{(TM)^2}\epsilon_{\|}\epsilon_{\perp}}} \\ TE : \tan\left(\frac{\varkappa^{(TE)}d}{2}\right) &= \frac{\sqrt{\mathrm{k}^2(\epsilon_{\|} - \epsilon_m) - \varkappa^{(TE)^2}}}{\varkappa^{(TE)}} \end{aligned} \tag{3.17}$$

3.4.1 Correction for κ Parameter

From the above mode profile equations (Eq. 3.17) we can determine the exact value of the mode parameter $\varkappa$. Taking the limiting case of $\epsilon_m \to -\infty$ in the profile equations above yields the values $\varkappa_0 = \pi(2j+1)/d$ which match our $\varkappa$ definition from Section 3.1. These values correspond to the modes having a magnitude of

zero at the waveguide boundary as in the ideal case. In the limit of sufficiently large $|\epsilon_m|$ it is possible to use a Taylor expansion to find the correction to the above values of the mode parameter $\varkappa$. Since both $\varkappa$ and ϵ_m appear in Eq. 3.17 we will need the Taylor expansion of two variables. Out to the third term it is given by [89],

$$\begin{aligned} f(a+x,b+y) &= f(a,b)+x\frac{\partial f(a,b)}{\partial x}+y\frac{\partial f(a,b)}{\partial y}+\frac{1}{2!}\left[x^2\frac{\partial^2 f(a,b)}{\partial x^2}+\right. \\ &\quad \left. 2xy\frac{\partial^2 f(a,b)}{\partial x\partial y}+y^2\frac{\partial^2 f(a,b)}{\partial y^2}\right]+... \end{aligned} \tag{3.18}$$

We define $\varkappa = \pi(2j+1)/d + \xi$, where ξ is a small correction term. Recall from Section 3.4 that $\epsilon_m = -1/\gamma$ so $\gamma = -1/\epsilon_m$ and in the limit $\epsilon_m \to -\infty$; $\gamma \to 0$. Thus, we can use both ξ and γ as our parameters approaching zero in Eq. 3.17. Starting with the inverse of Eq. 3.17, expanding both sides of the equation with a Taylor series, and solving for κ_0 gives,

$$\begin{aligned} \kappa^{(TM)} &\approx \kappa_0\left(1-\frac{2\mathrm{k}\epsilon_\parallel}{\kappa_0^2 d\sqrt{-\epsilon_m}}\right) \\ \kappa^{(TE)} &\approx \kappa_0\left(1-\frac{2}{\mathrm{k}d\sqrt{-\epsilon_m}}\right). \end{aligned} \tag{3.19}$$

Considering the inverse confinement scale of the $\varkappa$ definition in Section 3.1, the negative correction in Eq. 3.19 signifies the "mode expansion" into the waveguide wall region, as illustrated in Fig. 3.5 [25].

3.4.2 Correction for Index of Refraction

Starting from the κ corrections above, we can determine how the propagation constant, ν, changes as the waveguide mode structure alters due to finite wall conductivity. We assume $\nu = \nu_0 + \delta$, where δ is a small correction to ν and $\nu_0 = 1 - \frac{\varkappa_0^2}{\epsilon_\parallel k^2}$. Then,

$$\nu = \nu_0 + \delta = 1 - \frac{(\xi+\kappa_0)^2}{\epsilon_\parallel k^2}, \tag{3.20}$$

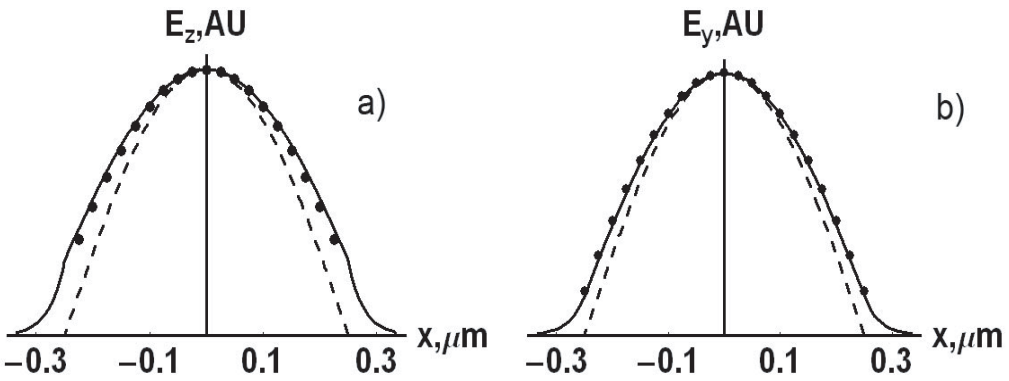

Figure 3.5: The cross-section of the field in the planar waveguide with hollow $d = 0.5$ μm-thick core; dashed line corresponds to the case of $\epsilon_m = -\infty$ (perfect metal boundary); solid line corresponds to Ag boundaries for $\lambda = 0.85$ μm; dots correspond to κ calculated using Eq. (3.19); TM (a) and TE (b) modes are shown

and the right-hand side can be expanded into a Taylor series as $\xi \to 0$. Solving for δ and plugging in the kappa corrections in Eq. 3.19 we arrive at the correction to the ν parameter,

$$\nu^{(TM)} \approx \nu_0 + \frac{4}{k\kappa_0 d\sqrt{-\epsilon_m}} \tag{3.21}$$

$$\nu^{(TE)} \approx \nu_0 + \frac{4\kappa_0}{\epsilon_\parallel k^3 d\sqrt{-\epsilon_m}} \tag{3.22}$$

A similar approach can be taken to find the more revealing modification to the refraction index, n. starting from $n_0 + \eta = \sqrt{\epsilon(\nu_0 + \delta)}$, doing the series expansion, and solving for the index correction term, η, gives:

$$n^{(TM)} \approx \pm\sqrt{\epsilon_\perp \nu_0}\left(1 + \frac{2}{\mathrm{k}\ d\ \nu_0\sqrt{-\epsilon_m}}\right) \tag{3.23}$$

$$n^{(TE)} \approx \sqrt{\epsilon_\parallel \nu_0}\left(1 + \frac{2\kappa_0^2}{\mathrm{k}^3 d\ \epsilon_\parallel \nu_0\sqrt{-\epsilon_m}}\right)$$

As described above, the sign of the refraction index for the TM polarization must be selected *positive* for $\epsilon_\perp > 0$; $\nu > 0$, and *negative* for $\epsilon_\perp < 0$; $\nu < 0$. Table 3.1 shows numerically calculated indices of refraction versus those found analytically

with the correction taken into account. The proximity of the values validates our analytical calculations.

Mode	nTM Modes		nTE Modes	
	Numeric	Analytic	Numeric	Analytic
0	$0.56 + 0.002i$	$0.57 + 0.002i$	$0.528 + 0.001i$	$0.533 + 0.002i$
1	$0.001 + 1.29i$	$0.001 + 1.29i$	$0.001 + 1.219i$	$0.001 + 1.207i$
2	$0.000 + 2.38i$	$0.000 + 2.38i$	$0.001 + 2.23i$	$0.001 + 2.22i$

Table 3.1: Numerically calculated indices of refraction, n, for TM and TE modes compared to the analytically corrected values accounting for finite waveguide wall conductance.

This effective refractive index reveals another effect on wave propagation caused by the mode penetration into the waveguide wall region. Namely, the finite value of the imaginary part of ϵ_m, ϵ_m'', introduces an additional absorption into the system besides that of the core material. As a result, the magnitude of a mode will exponentially decay as it propagates through the system. The imaginary part of the effective refractive index is related to this attenuation through $E \propto \exp(-n''\mathrm{k_z}z)$. In the limit of small absorption in the metal ($\epsilon_m''/|\epsilon_m'| \ll 1$) the mode decay due to the field leakage into the waveguide walls is described by:

$$
\begin{aligned}
n^{(TM)''} &\approx \frac{1}{\mathrm{k}d}\sqrt{\frac{\epsilon_\perp}{\nu_0|\epsilon_m|}}\frac{\epsilon_m''}{|\epsilon_m'|} \\
n^{(TE)''} &\approx \frac{\kappa_0^2}{\mathrm{k}^3 d\sqrt{\epsilon_\parallel \nu_0|\epsilon_m|}}\frac{\epsilon_m''}{|\epsilon_m'|}
\end{aligned}
\tag{3.24}
$$

It is important to notice that despite the sign of the index of refraction the system losses are positive, agreeing completely with the causality principle [1, 17]. Assuming a non-absorbing media, we estimate the losses due to silver waveguide walls for wavelengths $\lambda \geq 850$ nm using Eq. (3.24) to be considerably small ($n''/n \lesssim 0.01$), as shown in Fig. 3.4.2 [25]. This information gives us a good idea for the practical size of the system.

3.5 Metamaterials with Giant Anisotropy

In this section we will consider the fabrication perspectives of the materials with extreme anisotropy of dielectric constant required to build the NIM waveguides described in this paper. We need a material with $\epsilon_{\|}$ and $\epsilon_{\perp}$ of opposite sign. Naturally occurring homogeneous materials with this necessary anisotropy include thin Bi and Sapphire films in the THz and far-IR frequencies. The extreme anisotropy in these systems originates from the anisotropy of the effective electron mass, which translates into anisotropy of the plasma frequency [90]. However, no known natural material exhibits anisotropy exceeding 30% in the optical or IR spectral ranges.

Due to the narrow bandwidth of frequencies for which natural strongly anisotropic materials are available, an approach to fabricating these materials must be considered. Metamaterials, a new class of nanostructured composites, can be used to provide the desired EM properties for a broader range of frequencies. Specifically, we propose using a combination of plasmonic particles ($\epsilon < 0$) and dielectric media ($\epsilon > 0$) to achieve the strong optical anisotropy. If the size and separation of these inhomogeneities is smaller than the incident radiation wavelength, the metamaterial will appear as being homogeneous and will support modes similar to a plane wave. As explained in Ref. [25] these composites produce effects originating from the *effective medium*, or averaged properties. Hence, periodicity of the arranged particles is not required and only the *average concentration* of the inhomogeneities must be controlled during fabrication, indicating a high tolerance to fabrication defects. Here we will describe two ways to contruct these metamaterials thus obtaining strong anisotropy in the optical and IR frequencies.

3.5.1 Nanolayered Composites

The first metamaterial technique we consider is a periodic interchanging layers of dielectric (Si,GaAs) and plasmonic (Ag,Au,Al) materials with dielectric constants $\epsilon_d > 0$, $\epsilon_{pl} < 0$, and thicknesses $a_d,\ a_{pl}$ respectively. Figure 3.5.1(a) demonstrates the layers aligned in the waveguide along the (y, z) plane. The 1D photonic crystal disperion relation can describe the wave propagation in this system,

$$\cos\left[\kappa(a_d + a_{pl})\right] = \cos(k_d a_d)\cos(k_{pl} a_{pl}) - \gamma \sin(k_d a_d)\sin(k_{pl} a_{pl}), \tag{3.25}$$

where $k_d^2 = \epsilon_d\omega^2/c^2 - k_y^2 - k_z^2$, $k_{pl}^2 = \epsilon_{pl}\omega^2/c^2 - k_y^2 - k_z^2$, and the parameter γ is equal to $\gamma_{TE} = \frac{1}{2}\left(\frac{\epsilon_{pl}}{\epsilon_d}\frac{k_d}{k_{pl}} + \frac{\epsilon_d}{\epsilon_{pl}}\frac{k_{pl}}{k_d}\right)$ and $\gamma_{TM} = \frac{1}{2}\left(\frac{k_d}{k_{pl}} + \frac{k_{pl}}{k_d}\right)$ for TE and TM modes respectively [91]. The κ parameter in the above equation is the same as in Sec. 3.1 and describes the mode in the x direction. In the "quasistatic" limit of thin layers and a relatively thick subwavelength waveguide $|\kappa\left(a_d + a_{pl}\right)| << 1$, $|k_d\left(a_d + a_{pl}\right)| << 1$, $|k_{pl|\left(a_d+a_{pl}\right)} << 1$, the dispersion relation above can be further simplified to the form identical to that of Eq. 3.3, with the *effective* values of dielectric constant found with a Taylor expansion to second order as,

$$\epsilon_\perp = \frac{\epsilon_d\epsilon_{pl}\left(a_d + a_{pl}\right)}{a_d\epsilon_{pl} + a_{pl}\epsilon_d}, \epsilon_\parallel = \frac{a_d\epsilon_d + a_{pl}\epsilon_{pl}}{a_d + a_{pl}} \tag{3.26}$$

[34, 92].

These values of effective permittivities derived for the photonic crystal system, are identical to those derived using conventional effective medium theory (EMT) as shown in Ref. [25, 34]. For sufficiently thin layers, EMT was believed to successfully describes quasistatic material properties where the only control parameter is the average volume concentration of the plasmonic layers, $N_{pl} = a_{pl}/\left(a_d + a_{pl}\right)$, and the absolute thickness of the individual layers is not important. Note that the limiting factor of this approach is the condition $|\kappa\left(a_d + a_{pl}\right)| << 1$, which defines the restraint of applying the EMT. Further analysis has revealed that conventional EMT fails to adequately describe electromagnetic wave propagation in a multilayered nanocomposite system due to nonlocal effects originating from strong field oscillations across the system [34]. Nonlocal corrections for the derived effective permittivity are necessary because the length scale of the typical field variation is less than the free-space wavelength, λ. Expanding Eq. 3.25 to the next nonvanishing term in the Taylor expansion gives new effective permittivites with corrections as shown in Ref. [34].

3.5.2 Nanowire Composites

Another technique to create strongly anisotropic metamaterials is to use an array of aligned plasmonic (metallic) nanowires ($\epsilon_{pl} < 0$) embedded in the dielectric (ϵ_d) host as shown in Fig. 3.5.1(b). The exact field structure across the nanowires is required to calculate the electromagnetic properties of the composite. The prob-

lem can be addressed with the Maxwell-Garnett approximation for the case of small plasmonic material concentration [17]. When considering the field inside the metallic wire inclusions, E_{in}, to be homogenous and assuming normal incidence the following effective dielectric constants are found:

$$\begin{aligned} \epsilon_{\parallel} &= \frac{N_{pl}\epsilon_{pl}E_{in} + (1 - N_{pl})\,\epsilon_d E_0}{N_{pl}E_{in} + (1 - N_{pl})\,E_0}, \\ \epsilon_{\perp} &= N_{pl}\epsilon_{pl} + (1 - N_{pl})\,\epsilon_d, \end{aligned} \tag{3.27}$$

where $E_{in} = \frac{2\epsilon_d}{\epsilon_d + \epsilon_{pl}} E_0$, and E_0 is the excitation field. Validation of the Maxwell-Garnett approach is shown in Ref. [25], where the numerical simulations agree closely with analytical results. The effective dielectric constants for some composite nanowired materials are shown in Fig. 3.8. These wired composites are shown to have extremely low absorption in the near-IR spectral range, especially compared to the layered structure above, and hence compensate for a major drawback of the traditional optical NIM designs [25].

The same nonlocal effects described in the nanolayer section above have been discovered for nanowire structures as well and are explored in Ref. [93]. Elser *et. al.* aim to better understand the optical behavior of nanowire structures with anisotropic cross sections beyond the conventional, one-parameter EMT by deriving an analytical description for the permittivity using the Maxwell-Garnett approach. The analytical theory is then verified, solving Maxwell's equations directly, using numerical three-dimensional simulations done with the commercial finite-element partial differential equations solver, COMSOL MULTIPHYSICS 3.2 [94].

Practical applications of nanowire-based optical composites include high energy density waveguides, which are subwavelength structures supporting volume modes [88, 95], polarization-sensitive sensors, and nonmagnetic negative-index systems such as the one presented in this paper. In the next section we will demonstrate how these materials can be used as a planar-lens, achieving sub-diffraction far-field resolution.

3.6 Planar Lens Optical Imaging

As mentioned in Section 2.3.3, sub-diffraction imaging through a planar slab is a novel application of negative index materials (NIMs), and is often referred to as superlensing. The suppression of the evanescent spectrum is the mechanism behind the resolution limit of an imaging system. In first comparing NIM lenses to conventional optical lenses it was shown that the realistic ϵ-μ-based NIM lens does not obtain an advantageous resolution over existing phase optics lenses for the far-field. This performance limit originates from the inherent losses present in real materials, from which an analytical "NIM diffraction limit" was derived [72]. This topic has seen much controversy and recently, Kuhta *et. al.* in Ref. [74] have calculated a quantitative measure of superlensing in a planar NIM lens system and developed a formalism to separate the regimes of superresolution and diffraction in the far-field. They show that far-field imaging is either governed by diffraction theory, where for small enough light wavelength the resolution is independent of absorption, or else by superresolution, which occurs for a critically low absorption. They identify a universal parameter combining absorption, wavelength, and lens thickness to describe the transition between the diffraction-limited and superresolution regimes [74]. Near-field superresolution has been found both theoretically and experimentally [72, 96]. For near-field image resolution, the optimal configuration for the superlens has been identified in Ref. [78] to be when the object distance is equal to the lens width ($a = b$) versus the conventional superlens design, where the lens is symmetrically centered between the object and the image ($2a = b$). They derive an analytical result for the resolution of the generalized planar lens and conclude that the optimal configuration minimizes both the field intensity inside the NIM lens *and* the total absorption in the imaging system. They also demonstrate that near-field imaging becomes inapplicable when the absorption in the NIM region exceeds 30% [78].

In contrast to conventional diffraction-limited, ϵ-μ NIMs, the proposed non-magnetic system can be used to image sources in the far-field. This can be achieved because the effective refractive index $|n|$ is high, in turn reducing the internal wavelength, $\lambda_0/|n|$, and effectively postponing the diffraction limit in the far-field. To demonstrate optical imaging in our system we use a single planar waveguide containing a slab of anisotropic left-handed material.

3.6.1 Simulation Approach

We use exact 3D numerical techniques to simulate imaging in our waveguide system. The electric and magnetic fields are set up as functions as defined in Sec. 3.1. The positive index material, or right-handed media (RHM), is defined with isotropic ($\epsilon_{\parallel}^{RHM} = \epsilon_{\perp}^{RHM}$) permittivities usually for Si ($\epsilon = 13$) or air ($\epsilon = 1$). The values for $\epsilon_{\parallel}$ and $\epsilon_{\perp}$ in the NIM are found using calculated nanowire metamaterial permittivites from the equations in Sec. 3.5.2. Absorption may be considered in the system by adding a small imaginary component to the effective permittivities of the NIM. We assume the telecom wavelength of $\lambda = 1.5$ μm and set the free space wave vector $k = \frac{2\pi}{\lambda}$. The step size, h, is crucial to these simulations as the parameter, κ, is defined as $\frac{\pi}{h}$ in the code. Lastly, ν is defined with separate values for the positive and negative index materials using Eq. 3.7.

Let us first consider the special case of normal (z) propagation of a TM-polarized wave as in done by the authors in Ref. [1]. A normal incidence wave has $k_y = 0$ and because it's TM polarized, $H_z = H_x = 0$, therefore, neither refracted nor reflected TE-polarized waves are excited. According to Eq. 3.1, when $k_y = 0$, the H_y and E_x field components can be related via: $H_y = (k\epsilon_{\perp}/k_z)\, E_x$. Notice from this equation that since tangential fields must be continuous across the $z = 0$ boundary, ($H_y^{RHM} = H_y^{NIM}$), k_z must have the same sign as $\epsilon_{\perp}$. Then for our $\epsilon_{\perp} < 0, \nu < 0$ region, we have confirmed a negative phase velocity and left-handed media. Podolskiy *et. al.* proceed to consider the general, more complicated, case of oblique wave incidence and produce the simulations like those in Fig. 3.3(c)[1].

We start by modeling the incident emitted radiation as a double-slit source with slit size w, positioned at $w \leq |y| \leq 2w$, $z = 0$, and an arbitrary x value, since we are simulating planar imaging in the (y, z) plane. The k_y spectrum of this monochromatic source is shown in Fig. 3.9 and given by,

$$A(k_y) = \frac{2}{k_y} \left[\sin(2wk_y) - \sin(wk_y)\right]. \tag{3.28}$$

First we need to define the variables necessary in order to numerically represent this continuous radiation function using a discrete k_y array. The variable dky defines the periodicity of the double slits, and in this case the occurrence of double

slits is significant because we don't want the radiation from neighboring ones to influence our calculations. Hence, $dky = \frac{0.05}{w}$, to obtain a value smaller than 0.5. The variable, N, defines the scaled y range which controls the smoothness of the system. N is generally on the order of 10^1. Putting these together we create an array of k_y values such that k_y ranges from $k \times -N$ to $k \times N$ in increments of dky. This system supports both TE and TM modes as discussed in Sec. 3.1 and each mode type has its own propagation constant, k_z, which for this case is an array of k_z values corresponding to each k_y. There are M modes for each polarization (TE and TM), hence $2M$ waveguide modes total, where M is equal to the length of the k_y array. The TM and TE type k_z arrays for both the positive and negative index regions are assigned by manipulating Eq. 3.6 and solving for k_z. The k_z array for the TM mode in the NIM is given by,

$$k_z[i] = \sqrt{\epsilon_{\perp}^{NIM} \nu^{NIM} k^2 - k_y[i]^2}. \tag{3.29}$$

To calculate the resulting field distribution we first represent the wavepacket at the $z = 0$ plane as a linear combination of the $2M$ waveguide modes [1, 90]. We then use the first three boundary conditions from Eq. 3.15 at the front and back interfaces of the NIM region; specifically the fact that E_x is continuous, E_y is continuous, D_z is continuous, and H_y is continuous. The boundary conditions are employed as a system of $2M$ equations and $2M$ unknowns which we solve to calculate the reflection and transmission coefficients of individual modes. The reflection and transmission coefficient values are stored in appropriate arrays with each index corresponding to a single mode. The solutions of Maxwell equations are then represented as a sum of solutions for the individual modes [1, 25]. We can illustrate the imaging of the double-slit source through the NIM lens by calculating the total $\vec{E}$ and $\vec{H}$ fields for both the positive and negative index media. The total fields are found by summing TE and TM fields multiplied by the incident, transmission, and reflected coefficients depending on the region. We then plot the intensity of the fields, $|\vec{D} \cdot \vec{E}|$, for a specific x value in the (y, z) plane. The results and performance of imaging through our NIM planar-lens are examined in the following section.

3.6.2 Performance of Imaging

To illustrate the imaging performance of our proposed system we first calculated the propagation of a wave packet formed by a double-slit source through 5 μm long planar layer of 5% Ag, 95% SiO_2 wire-based NIM core described in Sec. 3.5 (see Fig. 3.8(a,b)) embedded in a Si waveguide. We select the thickness of the dielectric core to be $d = 0.3\ \mu m$ and assume the excitation telecom wavelength, $\lambda = 1.5\ \mu$m. Combining Eqs. 3.23 and 3.27 yield the following values of the refraction index: $n^{(+)} \approx 2.6$, $n^{(NIM)} \approx -2.6 + 0.05i$. To better exemplify the imaging properties of the system and distinguish between the effects of a negative refractive index and material absorption, we first neglect losses in the NIM core. Using the simulation code outlined above, the resulting intensity distribution in the system is shown in Fig. 3.10. The image formation in the focal plane ($z = 10\ \mu$m) of the far-field planar NIM lens in clearly seen.

Next we aim to compare the imaging through the planar NIM lens with and without the material absorption and demonstrate that although the presence of weak loss reduces the magnitude of the signal, it does not destroy the far-field imaging. In order to do this we plot the cross section of the intensity distribution at the focal plane. In Fig. 3.11(a) we simulate the same Ag, SiO_2 system described above, with slit size $w = 0.75\ \mu$m. We plot the emitted radiation from our double slit source with the dashed line, the perfect non-absorbing focal plane field intensity with the solid line, and the real, absorbing NIM field intensity magnified five times as shown with the dash-dotted line. For Fig. 3.11(b) we have decreased the slit size to $w = 0.3\ \mu$m in order to demonstrate the far-field resolution limit of the system. The plot shows the emitted radiation with the dashed line and the intensity of the field with absorbing media with the dash-dotted line. The two peaks are no longer distiguishable when the intensity in the region between them is more than half of the the peak intensity [25]. Recall that the index of refraction for this particular nanowire NIM waveguide core is $n^{(NIM)} \approx -2.6 + 0.05i$ and the incident radiation is assumed to be the telecom wavelength, $\lambda = 1.5\ \mu$m. The resolution, Δ, of the non-magnetic NIM structure is limited by the internal wavelength: $\Delta \approx \lambda_{in}/2 = \lambda_0/|2n| \approx \lambda_0/5 = 0.3\ \mu$m. This result is encouraging because it is similar to the resolution of any far-field imaging system as mentioned in Sec. 2.3.3 [17, 72, 90].

To demonstrate the onset of the diffraction limit in our system using two-dimensional imaging simulations, we change parameters to utilize the optimal configuration of the planar-lens as mentioned in Sec. 3.6. The incident radiation occurs at $z = 0$ and the NIM is now located between $z = 2.5$ μm and $z = 5.0$ μm. The far-field image formation in the focal plane ($z = 5$ μm) and the appearance of the diffraction limit can be observed in Fig. 3.6.2. When the slit size is greater than the resolution limit, $\lambda/2n$, two distinct peaks can be seen as in (a) and (b). However, when w approaches this limit as in (c) the contrast at the focal plane is harder to recognize. In the last image, w is obviously below the diffraction limit as the two subwavelength peaks have collapsed into a single diffraction-limited image. To better illustrate the imaging performance of our system, we neglected the material absorption when we calculated the images in Fig. 3.6.2.

3.7 Concluding Remarks

In this chapter, we have laid out a novel approach to use a two-dimensional, planar waveguide with anisotropic dielectric core to build negative index of refraction materials. Our design is advantageous because it is non-magnetic, homogeneous, and has low losses. It is also scalable to a large range of frequencies, including the optical and infrared frequencies, which are important for current practical applications, such as effectively collecting radiation into small, deep subwavelenth waveguides, which ultimately may lead to miniaturization of all waveguide devices.

We define and characterize the proposed waveguide system with the propagation parameter, ν, and use it along with the anisotropic dielectric constant, ($\epsilon_\perp$ or $\epsilon_\parallel$) to define the index of refraction as in Eq. 3.8. In Section 3.2 we clarified the necessity of having an anisotropic electric permittivity and how works with ν to achieve the desired negative index properties. The following section of this chapter explored the effects of finite conducting walls on the modal structure and negative refractive index inside the waveguide. Derivations for corrections to κ, which defines the mode structure, and the index of refraction, n, are examined along with realistic losses in the system.

This chapter included a section on the strongly anisotropic metamaterials we use for the NIM region in simulations of our system. We outlined an analytical description of electromagnetic properties of nanostructured metal-dielectric com-

posites, including nanolayered and nanowired metamaterials. The effective dielectric permittivites of these nanocomposites are presented while acknowledging the nonlocal effects due to field oscillations. The excellent agreement of the developed theory with results of a numerical solution to Maxwell equations is shown.

Finally, we have demonstrated the low-loss far-field planar NIM lens for $\lambda = 1.5$ μm with resolution $\Delta \approx 0.3$ μm. A summary of our simulation approach is given, and we illustrate imaging through a single planar waveguide with a slab of our anisotropic left-handed media. Our system provides far-field image resolution better than the conventional, free space limit, $\frac{\lambda_0}{2}$. This is due to our higher (> 1) index of refraction, which effectively delays the diffraction limit to be $\frac{\lambda_0}{2n}$. A series of images displays the performance of our planar NIM lens.

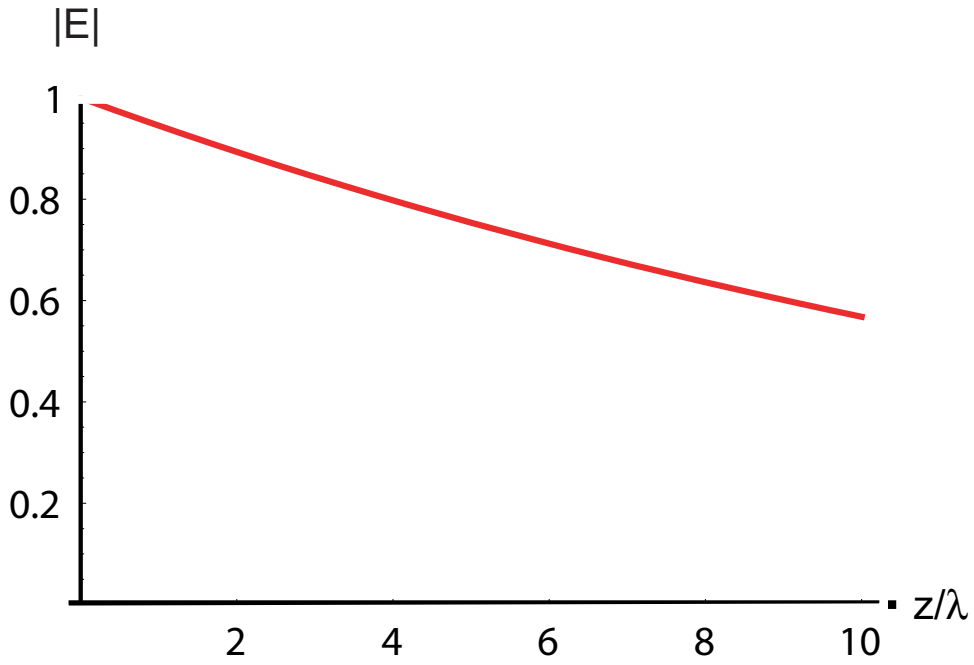

Figure 3.6: Electric field decay due to absorption of field in finite-conducting waveguide walls.

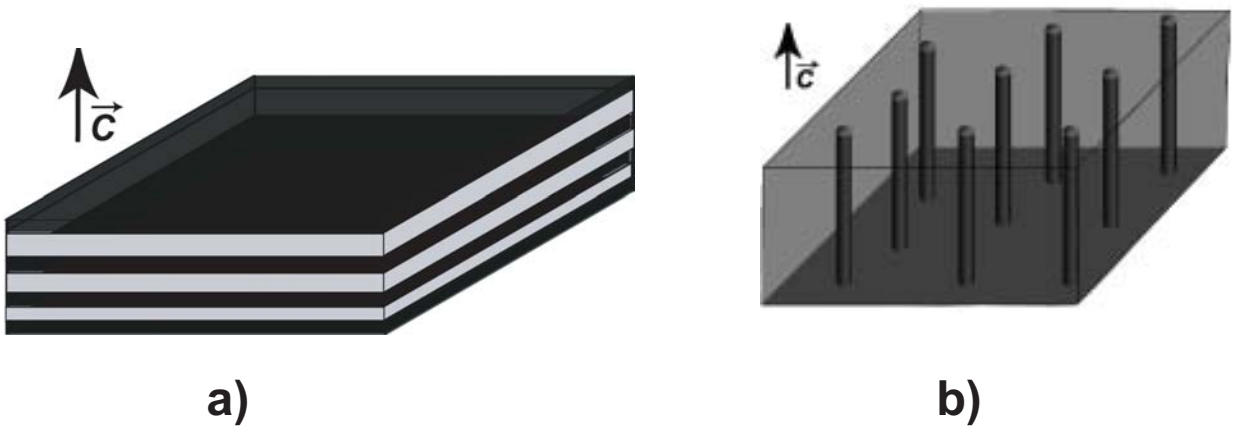

Figure 3.7: (a) Schematic of metamaterial layered structure; (b) Schematic of metamaterial nanowires structure.

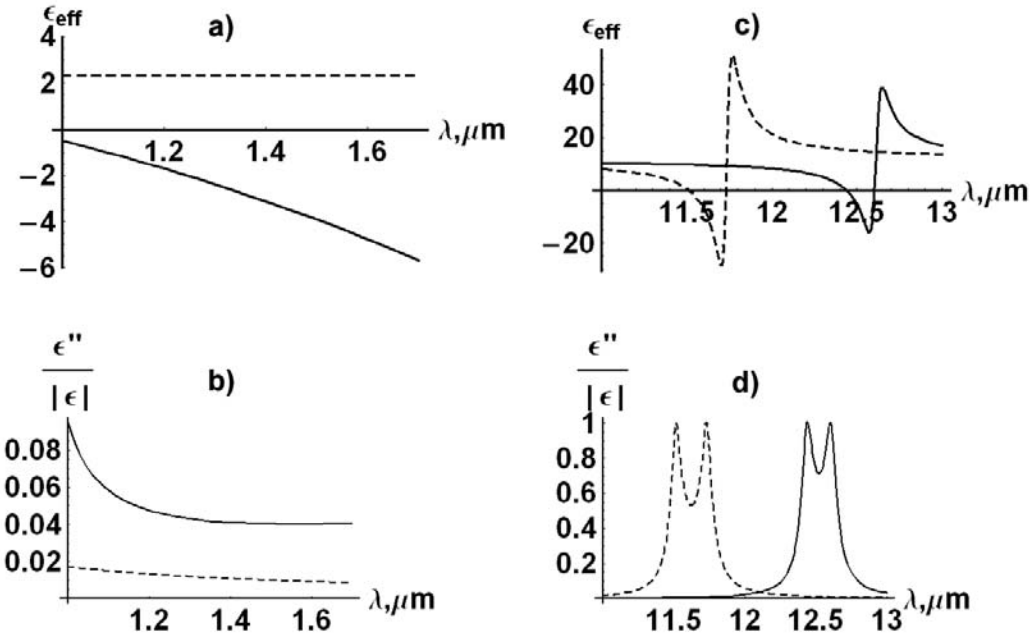

Figure 3.8: Real part (a,c) and absorption (b,d) of effective $\epsilon_\perp$ (solid lines) and $\epsilon_\parallel$ (dashed lines) for wired systems; (a,b): $Ag - SiO_2$ structure (note the relatively small absorption for the NIM regime); $N_{\rm pl} = 0.05$; (c,d): $SiC - Si$ structure; $N_{\rm pl} = 0.1$.

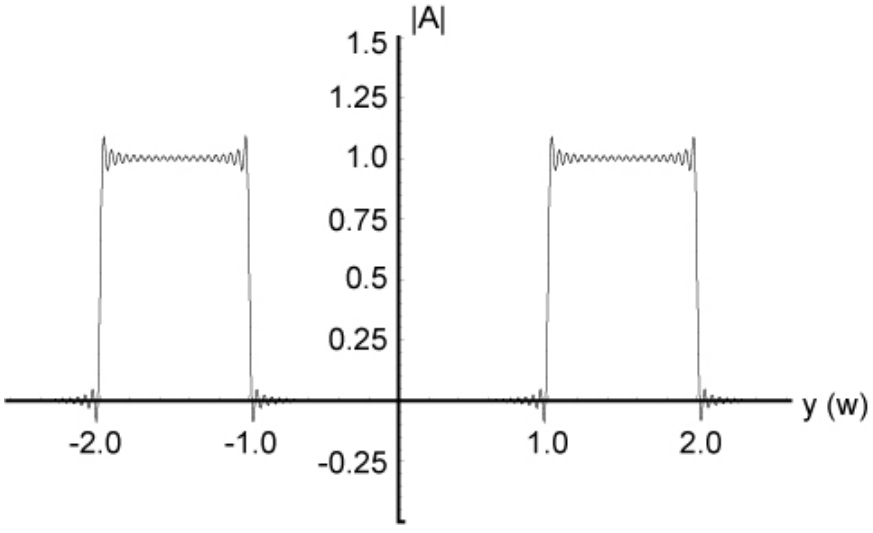

Figure 3.9: Calculated profile of incident radiation for the double-slit source with slit size w.

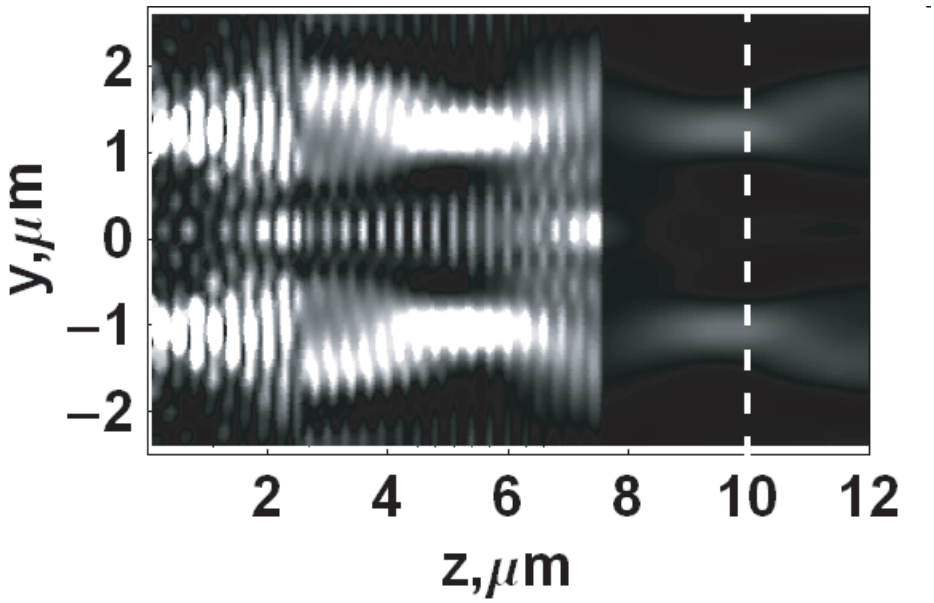

Figure 3.10: Imaging by a planar NIM-based lens. $n > 0$ region: Si-filled planar waveguide; $d = 0.3\ \mu m$; NIM region: planar waveguide with nanowire core material described in Fig. 3.5.1(b); The intensity distribution in the system with absorption losses neglected; the NIM region is between $z = 2.5\ \mu m$ and $z = 7.6\ \mu m$. The focal plane corresponds to $z = 10\ \mu m$ (white dashed line); the slit size is $w = 0.75\ \mu m$.

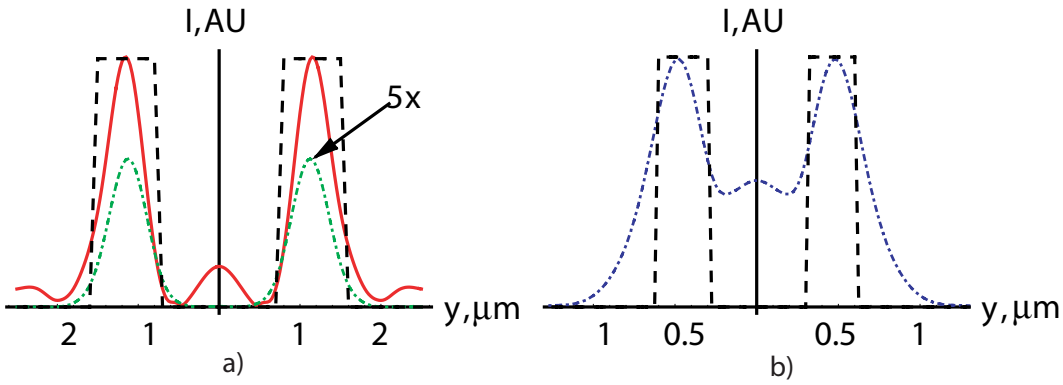

Figure 3.11: Imaging by a planar NIM-based lens. $n > 0$ region: Si-filled planar waveguide; $d = 0.3\ \mu$m; NIM region: planar waveguide with nanowire core material described in Fig. 3.5.1(b); (a) dashed line: emitted radiation; solid line: focal plane intensity distribution in system described in Fig. 3.10; dash-dotted line: same as solid line, but in the case of real (absorbing) NIM. (b) same as (a), but $w = 0.3\ \mu$m (corresponding to far-field resolution limit of the system).

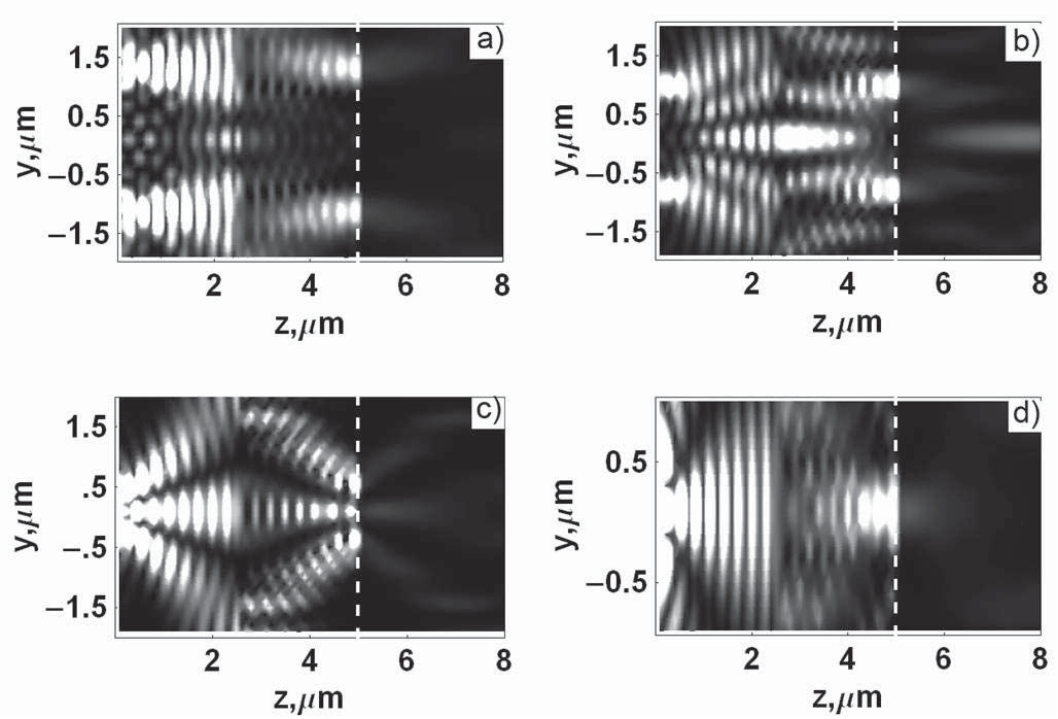

Figure 3.12: Planar waveguide NIM-based lens with absorption losses neglected. $\lambda_0 = 1.5$ μm; $n > 0$ material; Si-filled, $\epsilon = 13$; nanowire composite ($2.5 \leq 5$): $\epsilon_{\|} = 2.329 + 0.1i$; $\epsilon_{\perp} = -3.909 + 0.1i$. (a) The intensity distribution in the system with $d = 0.3$ μm; focal plane corresponds to $z = 5$ μm (back of lens); slit size $w = 0.8$ μm; (b) same as (a) but with $w = 0.6$ μm; (c) same as (a), but with $w = 0.3$ μm, corresponding to the far-field resolution limit of the system; (d) same as (a) with with $w = 0.15$ μm, below the resolution limit of the system.

Chapter 4 – Coupled NIM Waveguide System

In Chapter 3 we proposed a new approach to making a negative index material using a nonmagnetic, anisotropic dielectric filling inside a planar waveguide and demonstrated planar lens imaging through the system. The next logical step is to take a look at how different sized waveguides couple to our system. The goals are to find the transmission through and reflection from the system as a function of waveguide length and thickness, and to explore imaging through the system. This coupled approach effectively extends our two-dimensional imaging system into a three-dimensional one, where the imaging cross sections are now planes instead of one-dimensional lines as explained in Section 4.6. To begin, Section 4.1 considers a single boundary at the interface of two waveguides; a larger-sized waveguide with a positive index of refraction coupled to our NIM waveguide. We will refer to this as a single coupled waveguide system. We develop the algorithm to solve Maxwell's equations, match the appropriate boundary conditions, and determine the fields in all regions. A theory for the reflection coefficients from and transmission coefficients through the single coupled system is developed in Section 4.2. The theoretical results are compared with those from simulation. Next, we consider the coupled system where a smaller (nanoscale) waveguide is coupled on both the left and right ends to larger, micron-sized waveguides, referred to as a double coupled system. A relaxation technique is used to ensure convergence and matching of the fields for a given number of modes as explained in Section 4.3. For this double-boundary system we present results for the case where all the waveguides are composed of isotropic right-handed materials, as well as for the case where the smaller, internal waveguide is our NIM system in Sections 4.4-4.5. Finally, imaging though these systems is investigated.

4.1 Simulation Design

To calculate the propagation of the electromagnetic fields through the interface of two or more coupled planar waveguides of varied sizes, we developed the relaxation-type algorithm described below. The fields are defined in Sec. 3.1, as functions of

$x, y, z, \kappa, k_y, k_z, \epsilon_\parallel$, and $\epsilon_\perp$. The free space wave vector is $k = \frac{2\pi}{\lambda}$, where $\lambda = 1.5\ \mu$m, or the wavelength often used in telecommunications.

To ensure the correct sign of k_z for our calculations via equations similar to Eq. 3.29, it is necessary to explore the standard branch cut used in the complex Z-plane in order to find $\sqrt{{k_z}^2}$. Various computer algebra software programs use the conventional branch cut for $\sqrt{Z}$ in the complex plane along the negative part of the real axis $(-\infty, 0)$, allowing complex angles valued $-\pi < \theta < \pi$. For calculations manipulating k_z we desire a cut in the complex plane along the positive part of the real axis $(0, \infty)$, allowing complex angles $0 \leq \theta < 2\pi$. Hence, when Im(z) ≥ 0 we simply use the standard definition of the square root function and branch cut accordingly. When Im(z) < 0 we reflect the result of this square root function across the origin, thereby achieving our desired branch cut along the positive, real axis. It should be noted that we do not violate causality because we do not use this branch cut to determine the sign of n or any other computed complex values. We use it with the sole purpose of enforcing the correct sign for k_z.

We start by examining the coupling of an isotropic Si-filled waveguide to our left-handed metamaterial planar waveguide. Throughout this section, we will denote the isotropic waveguide with a minus, $^{(-)}$, superscript and the anisotropic, negative-index waveguide with a plus, $^{(+)}$, superscript, indicating the left and right sides of the interface respectively as seen in Fig. 4.1. The electric permittivities for the isotropic, dielectric-filled waveguide are the same ($\epsilon_\parallel = \epsilon_\perp$), while the effective permittivites for the negative index waveguide are specifically determined by the metamaterials described in Sec. 3.5 where $\epsilon_\parallel \neq \epsilon_\perp$ and $\epsilon_\perp < 0$. Absorption in this system only depends on ${\epsilon_\parallel}''$ and ${\epsilon_\perp}''$ because $\mu = 1$. For a single interface, the only size parameter to consider for the waveguides is their thickness in the x direction as they are assumed infinite in the y and z directions, surrounded above and below by an ideal conductor. The thickness of the isotropic waveguide (d_{out}) is always assumed to be equal to or larger than the anisotropic, NIM waveguide thickness (d_{in}) and both sizes are on the order of microns. Other parameters for the relaxation code include the number of modes, N, allowed in the waveguides, a constant wave vector in the y-direction, k_y, as well as the parallel and perpendicular permittivity values, κ arrays, and ν arrays for each waveguide region. Finally, the k_z array values for both TE and TM modes in each region are calculated as explained in Sec. 3.6.1.

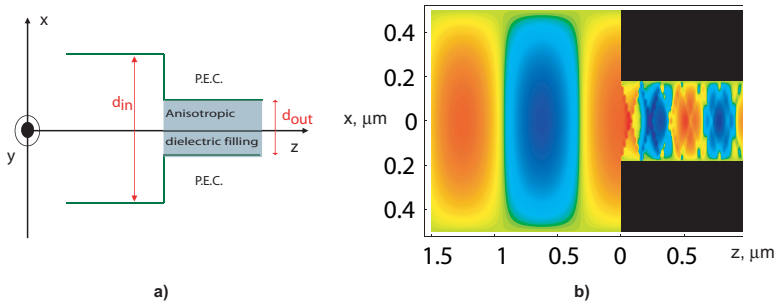

Figure 4.1: (a) Schematic to show coupling of a larger isotropic waveguide to our anisotropic NIM waveguide. (b) Direct coupling of planar waveguides. The $x-z$ cross-section of the system is shown with a single mode incident from an isotropic micro-scale waveguide to a nanoscale NIM waveguide where additional modes are excited.

The electric and magnetic fields in each waveguide region are represented as a combination of incident and reflected TE and TM modes of the form in Eq. 3.1. We assume a $\exp(-i\omega t)$ time dependence and an amplitude of $E_0^{(TM|TE)}$ for all waves but suppress it in the explicit field expressions below and throughout this paper. We assume the x dependence of $E_0^{(TM|TE)}$ is given by the symmetric (cos) mode. The z component of the TM $\vec{E}$ field can be written as,

$$E_z^{(TM,\pm)} = \sum_j \left(T_j^{(TM,\pm)} e^{ik_y y + ik_z z} + R_j^{(TM,\pm)} e^{ik_y y - ik_z z} \right) \cos(\kappa_j^{(\pm)} x) \tag{4.1}$$

where j is the modal index with range $1..N$, and the $\pm$ indicates the waveguide region where the field exists. $T_j^{(TM/TE,\pm)}$ and $R_j^{(TM/TE,\pm)}$ are $2N$-dimensional arrays containing the transmission and reflection coefficients for each mode polarization, respectively and depend only on the waveguide region;

$$R^{(+)} = \begin{pmatrix} r_1^{(TM,+)} \\ r_2^{(TM,+)} \\ \cdots \\ r_N^{(TM,+)} \\ r_1^{(TE,+)} \\ r_2^{(TE,+)} \\ \cdots \\ r_N^{(TE,+)} \end{pmatrix} \quad T^{(+)} = \begin{pmatrix} t_1^{(TM,+)} \\ t_2^{(TM,+)} \\ \cdots \\ t_N^{(TM,+)} \\ t_1^{(TE,+)} \\ t_2^{(TE,+)} \\ \cdots \\ t_N^{(TE,+)} \end{pmatrix} \tag{4.2}$$

$$R^{(-)} = \begin{pmatrix} r_1^{(TM,-)} \\ r_2^{(TM,-)} \\ \cdots \\ r_N^{(TM,-)} \\ r_1^{(TE,-)} \\ r_2^{(TE,-)} \\ \cdots \\ r_N^{(TE,-)} \end{pmatrix} \quad T^{(-)} = \begin{pmatrix} t_1^{(TM,-)} \\ t_2^{(TM,-)} \\ \cdots \\ t_N^{(TM,-)} \\ t_1^{(TE,-)} \\ t_2^{(TE,-)} \\ \cdots \\ t_N^{(TE,-)} \end{pmatrix} \tag{4.3}$$

There are a combined total of $8N$ T and R coefficients, including N TM and N TE modes for both reflection and transmission in both the $^{(+)}$ and $^{(-)}$ waveguide regions. Only $4N$ of these are unknown since we assume the incident radiation from the left, $T^{(TM/TE,-)}$, and from the right, $R^{(TM/TE,+)}$ for all N modes. The remaining coefficients are found by matching the electromagnetic fields for each mode at the boundary of the coupled waveguides to acquire $4N$ equations which can be solved, as shown in the following section. Once the coefficients are determined, all field components can be calculated using Eq. 3.1.

4.1.1 Boundary Conditions

In order to match the fields at the interface between the coupled waveguides, it is necessary to satisfy the boundary conditions listed in Sec. 3.4. We choose to enforce the the continuity of $\vec{D_\perp}(\vec{D_z})$, $\vec{H_\parallel}(\vec{H_x})$, and $\vec{E_\parallel}(\vec{E_x}, \vec{E_y})$ across the interface between the two waveguides with thicknesses d_{out} and d_{in}. The total fields representing these conditions are,

$$D_z: \quad \sum_j \epsilon_{\parallel}^{(-)} \left[R_j^{(TM,-)} \cos(\kappa_j^{(-)} x) + \frac{k_y}{{k_{z,j}}^{(TE,-)}} R_j^{(TE,-)} \cos(\kappa_j^{(-)} x) \right. \tag{4.4}$$

$$\left. + T_j^{(TM,-)} \cos(\kappa_j^{(-)} x) - \frac{k_y}{{k_{z,j}}^{(TE,-)}} T_j^{(TE,-)} \cos(\kappa_j^{(-)} x) \right]$$

$$= \sum_j \epsilon_{\parallel}^{(+)} \left[R_j^{(TM,+)} \cos(\kappa_j^{(+)} x) + \frac{k_y}{{k_{z,j}}^{(TE,+)}} R_j^{(TE,+)} \cos(\kappa_j^{(+)} x) \right.$$

$$\left. + T_j^{(TM,+)} \cos(\kappa_j^{(+)} x) - \frac{k_y}{{k_{z,j}}^{(TE,+)}} T_j^{(TE,+)} \cos(\kappa_j^{(+)} x) \right]$$

$$H_x: \quad \sum_j \left[\frac{{k_{z,j}^{(TE,-)}}^2 + k_y^2}{k k_{z,j}^{(TE,-)}} R_j^{(TE,-)} \cos(\kappa_j^{(-)} x) - \frac{{k_{z,j}^{(TE,-)}}^2 + k_y^2}{k k_{z,j}^{(TE,-)}} T_j^{(TE,-)} \cos(\kappa_j^{(-)} x) \right] \tag{4.5}$$

$$= \sum_j \left[\frac{{k_{z,j}^{(TE,+)}}^2 + k_y^2}{k k_{z,j}^{(TE,+)}} R_j^{(TE,+)} \cos(\kappa_j^{(+)} x) - \frac{{k_{z,j}^{(TE,+)}}^2 + k_y^2}{k k_{z,j}^{(TE,+)}} T_j^{(TE,+)} \cos(\kappa_j^{(+)} x) \right]$$

$$E_x: \quad \sum_j \left[\frac{i{k_{z,j}^{(TM,-)}}^2 + k_y^2}{k_{z,j}^{(TM,-)} \kappa_j^{(-)}} \frac{\epsilon_{\parallel}^{(-)}}{\epsilon_{\perp}^{(-)}} R_j^{(TM,-)} \sin(\kappa_j^{(-)} x) \right. \tag{4.6}$$

$$\left. - \frac{i{k_{z,j}^{(TM,-)}}^2 + k_y^2}{k_{z,j}^{(TM,-)} \kappa_j^{(-)}} \frac{\epsilon_{\parallel}^{(-)}}{\epsilon_{\perp}^{(-)}} T_j^{(TM,-)} \sin(\kappa_j^{(-)} x) \right]$$

$$= \sum_j \left[\frac{i{k_{z,j}^{(TM,+)}}^2 + k_y^2}{k_{z,j}^{(TM,+)} \kappa_j^{(+)}} \frac{\epsilon_{\parallel}^{(+)}}{\epsilon_{\perp}^{(+)}} R_j^{(TM,+)} \sin(\kappa_j^{(+)} x) \right.$$

$$\left. - \frac{i{k_{z,j}^{(TM,+)}}^2 + k_y^2}{k_{z,j}^{(TM,+)} \kappa_j^{(+)}} \frac{\epsilon_{\parallel}^{(+)}}{\epsilon_{\perp}^{(+)}} T_j^{(TM,+)} \sin(\kappa_j^{(+)} x) \right]$$

$$E_y: \quad \sum_j \left[-\frac{k_y}{k_{z,j}^{(TM,-)}} R_j^{(TM,-)} \cos(\kappa_j^{(-)} x) + R_j^{(TE,-)} \cos(\kappa_j^{(-)} x) \right. \tag{4.7}$$

$$\left. + \frac{k_y}{k_{z,j}^{(TM,-)}} T_j^{(TM,-)} \cos(\kappa_j^{(-)} x) + T_j^{(TE,-)} \cos(\kappa_j^{(-)} x) \right]$$

$$= \sum_j \left[-\frac{k_y}{k_{z,j}^{(TM,+)}} R_j^{(TM,+)} \cos(\kappa_j^{(+)} x) + R_j^{(TE,+)} \cos(\kappa_j^{(+)} x) \right.$$

$$\left. + \frac{k_y}{k_{z,j}^{(TM,+)}} T_j^{(TM,+)} \cos(\kappa_j^{(+)} x) + T_j^{(TE,+)} \cos(\kappa_j^{(+)} x) \right]$$

The boundary conditions in Eq. 3.15 must be satisfied for the dielectric-dielectric portion of the interface, but we need to further consider the dielectric-conductor portion lying directly above and below the smaller waveguide. The boundary conditions are modified for the $\vec{D}$ and $\vec{H}$ fields on that part of the interface due to the perfect conductor,

$$\begin{aligned} \hat{n} \cdot \vec{D} &= \sigma, \\ \hat{n} \times \vec{H} &= K, \end{aligned} \tag{4.8}$$

where σ is the surface charge density, and K is the surface current on the conductor [26]. The normal component of the $\vec{D}$ field across dielectric-conductor interface is satisfied with the surface charge density build up on the conductor. The charges inside the conductor are assumed to be so mobile as to have an instantaneous response to changes in the fields, creating a surface charge density, σ, resulting in a zero electric field inside the conductor. The same is true for the tangential (x) component of the $\vec{H}$ field. The surface charges move, reacting to the tangential magnetic field, always producing the correct surface current, $\vec{K}$, supporting zero magnetic field inside the perfect conductor [26]. Thus, both D_z and H_x can exist outside a perfect conductor but drop to zero abruptly inside and we do not have to enforce the field continuity over the dielectric-conductor interface like we do for the tangential $\vec{E}$ fields.

To decouple the boundary condition equations we use the orthogonality of the cos and sin functions. All of the field equations (Eqs. 4.4, 4.5, 4.6, 4.7) contain either $\cos(\kappa_j^{(\pm)} x)$ or $\sin(\kappa_j^{(\pm)} x)$ functions so we multiply each equation by a similar function containing a $\kappa_l^{(\pm)}$ value with a different index, l. When we integrate these functions over the appropriate d_{in} or d_{out} waveguide thickness, the κ parameters of the same type ($^{(+)}$ or $^{(-)}$) with different indices will disappear, leaving only those with the same indices, thus simplifying the above boundary condition equations. Overlapping the modes by integrating either $\cos(\kappa_j^{(\pm)} x)\cos(\kappa_l^{(\pm)} x)$ or $\sin(\kappa_j^{(\pm)} x)\sin(\kappa_l^{(\pm)} x)$ over the designated waveguide size, we create the following square, $N \times N$, matrices with elements calculated from:

$$I_{l,j}^{(\pm)} = \int_{-\frac{d_{(in)}}{2}}^{\frac{d_{(in)}}{2}} \cos(\kappa_j^{(\pm)} x) \cos(\kappa_l^{(+)} x) dx \tag{4.9}$$

$$J_{l,j}^{(\pm)} = \int_{-\frac{d_{(in/out)}}{2}}^{\frac{d_{(in/out)}}{2}} \sin(\kappa_j^{(\pm)} x) \sin(\kappa_l^{(-)} x) dx \tag{4.10}$$

$$K_{l,j}^{(\pm)} = \int_{-\frac{d_{(in/out)}}{2}}^{\frac{d_{(in/out)}}{2}} \cos(\kappa_j^{(\pm)} x) \cos(\kappa_l^{(-)} x) dx. \tag{4.11}$$

The I matrix will be substituted into the $\vec{D}_z$ and $\vec{H}_x$ field equations, the J matrix into the $\vec{E}_x$ field equation, and the K matrix into the $\vec{E}_y$ field equation. Note that the integration for the creation of the I matrix includes a multiplication by a (+)-side cos mode and goes symmmetrically over only the smaller waveguide thickness, d_{in}. This choice is made because the modified boundary conditions in Eq. 4.8 are satisfied for the rest of the interface. The integration for the J and K matrices, satisfying the E_x and E_y continuities respectively, includes a multiplication by a (-)-side mode, and has integration limits dependent on the side of the interface in consideration, either d_{in} or d_{out}. This is because these fields are tangential to the interface and must be continuous across the entire boundary, both dielectric-dielectric and dielectric-conductor portions. It is important to mention that the $\cos(\kappa_j x)$ and $\sin(\kappa_j x)$ functions are only orthogonal for different κ modes in the *same* size waveguides. Hence, $I_{l,j}^{(+)} = I_{l,l}^{(+)}$, $J_{l,j}^{(-)} = J_{l,l}^{(-)}$, and $K_{l,j}^{(-)} = K_{l,l}^{(-)}$ as they are diagonal matrices. The remaining matrices are not as nice to work with as they involve intergrals with modes of both waveguide regions and require numerical computing.

Including the above orthogonality matrices, $I^{(\pm)}, J^{(\pm)}, K^{(\pm)}$, the boundary conditions in Eqs.(4.4, 4.5, 4.6, 4.7) can be simplified,

$$D_z: \quad \sum_j \epsilon_{\|}^{(-)} \left[I_{l,j}^{(-)} r_j^{(TM,-)} + \frac{k_y}{k_{z,j}^{(TE,-)}} I_{l,j}^{(-)} r_j^{(TE,-)} + I_{l,j}^{(-)} t_j^{(TM,-)} - \frac{k_y}{k_{z,j}^{(TE,-)}} I_{l,j}^{(-)} t_j^{(TE,-)} \right]$$
$$= \epsilon_{\|}^{(+)} \left[I_{l,l}^{(+)} r_l^{(TM,+)} + \frac{k_y}{k_{z,l}^{(+)}} I_{l,l}^{(+)} r_l^{(TE,+)} + I_{l,l}^{(+)} t_l^{(TM,+)} - \frac{k_y}{k_{z,l}^{(TE,+)}} I_{l,l}^{(+)} t_l^{(TE,+)} \right] \tag{4.12}$$

$$H_x: \quad \sum_j \left[\frac{{k_{z,j}^{(TE,-)}}^2 + k_y^2}{k k_{z,j}^{(TE,-)}} I_{l,j}^{(-)} r_j^{(TE,-)} - \frac{{k_{z,j}^{(TE,-)}}^2 + k_y^2}{k k_{z,j}^{(TE,-)}} I_{l,j}^{(-)} t_j^{(TE,-)} \right]$$
$$= \left[\frac{{k_{z,l}^{(TE,+)}}^2 + k_y^2}{k k_{z,l}^{(TE,+)}} I_{l,l}^{(+)} r_l^{(TE,+)} - \frac{{k_{z,l}^{(TE,+)}}^2 + k_y^2}{k k_{z,l}^{(TE,+)}} I_{l,l}^{(+)} t_l^{(TE,+)} \right] \tag{4.13}$$

$$E_x: \quad \left[i \frac{{k_{z,l}^{(TM,-)}}^2 + k_y^2}{k_{z,l}^{(TM,-)} \kappa_l^{(-)}} \frac{\epsilon_{\|}^{(-)}}{\epsilon_{\perp}^{(-)}} J_{l,l}^{(-)} r_l^{(TM,-)} - i \frac{{k_{z,l}^{(TM,-)}}^2 + k_y^2}{k_{z,l}^{(TM,-)} \kappa_l^{(-)}} \frac{\epsilon_{\|}^{(-)}}{\epsilon_{\perp}^{(-)}} J_{l,l}^{(-)} t_l^{(TM,-)} \right]$$
$$= \sum_j \left[i \frac{{k_{z,j}^{(TM,+)}}^2 + k_y^2}{k_{z,j}^{(TM,+)} \kappa_j^{(+)}} \frac{\epsilon_{\|}^{(+)}}{\epsilon_{\perp}^{(+)}} J_{l,j}^{(+)} r_l^{(TM,+)} - i \frac{{k_{z,j}^{(TM,+)}}^2 + k_y^2}{k_{z,j}^{(TM,+)} \kappa_j^{(+)}} \frac{\epsilon_{\|}^{(+)}}{\epsilon_{\perp}^{(+)}} J_{l,j}^{(+)} t_l^{(TM,+)} \right] \tag{4.14}$$

$$E_y: \quad \left[-\frac{k_y}{k_{z,l}^{(TM)}} K_{l,l}^{(-)} r_l^{(TM,-)} + K_{l,l}^{(-)} r_l^{(TE,-)} + \frac{k_y}{k_{z,l}^{(TM)}} K_{l,l}^{(-)} t_l^{(TM,-)} + K_{l,l} t_l^{(TE,-)} \right]$$
$$= \sum j \left[-\frac{k_y}{k_{z,j}^{(TM)} K_{l,j}}^{(+)} r_l^{(TM,+)} + K_{l,j}^{(+)} r_l^{(TE,+)} + \frac{k_y}{k_{z,j}^{(TM)} K_{l,j}^{(+)} t_j}^{(TM,+)} + K_{l,j} t_j^{(TE,+)} \right] \tag{4.15}$$

4.1.2 Matrix Manipulation

We combine the above boundary condition equations to create eight large matrices, which can then be multiplied by the reflection and transmission coefficient arrays, Eqs. (4.2, 4.2, 4.3, 4.3), to arrive at two simplified linearly coupled matrix equations representing the boundray conditions:

$$\begin{cases} 1_R^{(-)} R^{(-)} + 1_T^{(-)} T^{(-)} = 1_R^{(+)} R^{(+)} + 1_T^{(+)} T^{(+)} \\ 2_R^{(-)} R^{(-)} + 2_T^{(-)} T^{(-)} = 2_R^{(+)} R^{(+)} + 2_T^{(+)} T^{(+)} \end{cases} \tag{4.16}$$

Eqs. (4.12, 4.13) comprise the first four matrices, $1_R^{(\pm)}$ and $1_T^{(\pm)}$ with the D_z equations making up the top half of the matrices and the H_x equations the bottom half. Eqs. (4.14, 4.15) make up the next four, $2_R^{(\pm)}$ and $2_T^{(\pm)}$ with E_x on top and E_y on bottom. The dimension of each of these matrices is therefore $2N \times 2N$, with TM modes in the left column and TE modes in the right column. They follow from:

$$1_R^{(\pm)} = \begin{pmatrix} \epsilon_\parallel^{(\pm)} I_{l,j}^{(\pm)} & \epsilon_\parallel^{(\pm)} \frac{k_y}{k_{z,j}^{(TE,\pm)}} I_{l,j}^{(\pm)} \\ 0 & \frac{k_{z,j}^{(TE,\pm)^2} + k_y^2}{k k_{z,j}^{(TE,\pm)}} I_{l,j}^{(\pm)} \end{pmatrix} \tag{4.17}$$

$$1_T^{(\pm)} = \begin{pmatrix} \epsilon_\parallel^{(\pm)} I_{l,j}^{(\pm)} & -\epsilon_\parallel^{\pm} \frac{k_y}{k_{z,j}^{(TE,\pm)}} I_{l,j}^{(\pm)} \\ 0 & -\frac{k_{z,j}^{(TE,\pm)^2} + k_y^2}{k k_{z,j}^{(TE,\pm)}} I_{l,j}^{(\pm)} \end{pmatrix} \tag{4.18}$$

$$2_R^{(\pm)} = \begin{pmatrix} i \frac{k_{z,j}^{(TM,\pm)^2} + k_y^2}{k_{z,j}^{(TM,\pm)} \kappa_j^{(TM,\pm)}} \frac{\epsilon_\parallel^{(\pm)}}{\epsilon_\perp^{(\pm)}} J_{l,j}^{(\pm)} & 0 \\ -\frac{k_y}{k_{z,j}^{(TM,\pm)}} K_{l,j}^{(\pm)} & K_{l,j}^{(\pm)} \end{pmatrix} \tag{4.19}$$

$$2_T^{(\pm)} = \begin{pmatrix} -i \frac{k_{z,j}^{(TM,\pm)^2} + k_y^2}{k_{z,j}^{(TM,\pm)} \kappa_j^{(TM,\pm)}} \frac{\epsilon_\parallel^{(\pm)}}{\epsilon_\perp^{(\pm)}} J_{l,j}^{(\pm)} & 0 \\ \frac{k_y}{k_{z,j}^{(TM,\pm)}} K_{l,j}^{(\pm)} & K_{l,j}^{(\pm)} \end{pmatrix} \tag{4.20}$$

Next we algebraically manipulate the system of equations (4.16) to solve for the desired coefficient arrays $R^{(-)}$ and $T^{(+)}$ in terms of the known arrays, $R^{(+)}$ and $T^{(-)}$. It is important to keep in mind that matrices $1_R^{(+)}, 1_T^{(+)}, 2_R^{(-)}$, and $2_T^{(-)}$ are diagonal and therefore easy to invert, whereas the others are not diagonal and require numerical computing to invert. We want to avoid inverting these complicated matrices because of the lengthy computing time involved to perform the row operations necessary to reduce the matrix. Also, cancellation errors may occur due to the small complex numbers involved and sometimes just determining whether or not the matrix is invertible is a computationally intensive process. Thus, solving the first equation in Eq. 4.16 for $T^{(+)}$,

$$T^{(+)} = \frac{1}{1_T^{(+)}} \left[1_R^{(-)} R^{(-)} + 1_T^{(-)} T^{(-)} - 1_R^{(+)} R^{(+)} \right]. \tag{4.21}$$

Putting this into the second equation in (4.16) and solving for $R^{(-)}$ gives,

$$R^{(-)} = \left[2_R^{(-)} - 2_T^{(+)} \left(1_T^{(+)} \right)^{-1} 1_R^{(-)} \right]^{-1} \tag{4.22}$$
$$\left[\left(2_R^{(+)} - 2_T^{(+)} \left(1_T^{(+)} \right)^{-1} 1_R^{(+)} \right) R^{(+)} + \left(2_T^{(+)} \left(1_T^{(+)} \right)^{-1} 1_T^{(-)} - 2_T^{(-)} \right) T^{(-)} \right]$$

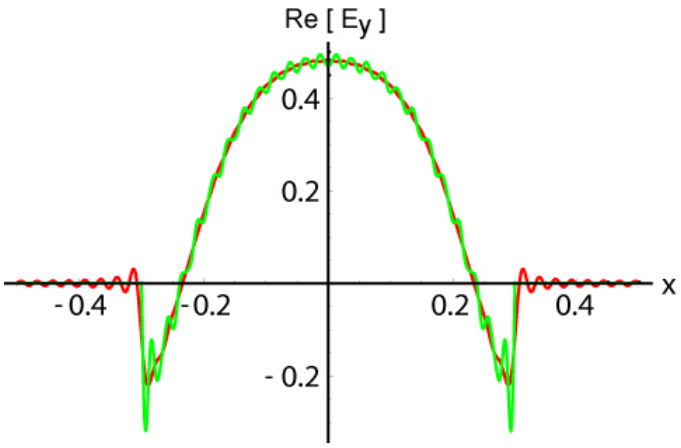

Figure 4.2: Cross-section plot of Re$[E_y]$ across the interface between a 1 μm thick Si waveguide and a 600 nm thick nanowire NIM waveguide. The red line represents the E_y field in the larger waveguide while the green line shows the field in the smaller waveguide.

The system can be excited with arbitrary electromagnetic modes from either the left side ($T^{(-)}$ known, $R^{(+)} = 0$), right side, ($R^{(+)}$ known, $T^{(-)} = 0$), or more generally from both directions. Once calculated, the arrays of coefficients above, along with the known coefficients, $T^{(-)}$ and $R^{(+)}$, are used in summations of the $\vec{E}$, $\vec{H}$, and $\vec{D}$ fields over the number of modes using Eq. 4.1. Summing the fields over all of the modes obtains the total of each field in each waveguide region. With the total fields calculated, we can verify that the boundary conditions are satisfied by plotting a cross section of the the real part of each field component on either side of the interface to ensure they match. Fig. 4.2 demonstrates the real part of the E_y field matching across the interface (along the x-direction) of

a system coupling a 1 μm thick Si waveguide to a 600 nm thick NIM, nanowire core, waveguide with $n = -4.4 + .17i$. The first TM mode is assumed incident with $k_y = 5$ or an incident angle of $\theta \approx -0.27$. Note that the fields match over the entire size of the smaller (NIM) waveguide as expected. The red line represents the E_y field in the Si waveguide and corresponding to the boundary conditions in Eq. 3.15 this field must go to zero at the interface beyond the dimesnsions of d_{in} as it borders a conductor. The green line represents the E_y field in the NIM waveguide.

Figure 4.1 (b) shows the single coupling of a 5 μm-sized isotropic air-filled waveguide to the same as above nanowire-core NIM waveguide which is 500 nm thick. The intensity of the $\vec{D}$ field is plotted for the $x - z$ cross-section at $y = 0$ with only the first TM mode incident from the left with an angle $\theta = 0$. Additional modes are excited inside the NIM waveguide due to mode coupling as illustrated by the X like patterns.

4.2 Theory for Reflection and Transmission Coefficients

As mentioned at the start of this chapter, the goal is to find a theory for transmission through and reflection from the proposed anisotropic, NIM, planar waveguide system as a function of the waveguide dimensions. The field of resonant light interaction with subwavelength structures has been the focus of research for some time but has increased recently with the promising applications of lithography, biosensing, and optical data storage and computing. Hans Bethe theoretically studied the diffraction of electromagnetic radiation by a hole of size smaller than the incident radiation wavelength in 1944 [97]. His prediction was that the transmission through the hole in infinitely thin metal was $(r\lambda)^4$, where r is the radius of the hole. More recently, near-field optics has moved beyond the simple Bethe theory both theoretically [98, 99, 100, 101, 102] and experimentally [103, 104, 105, 106]. Numerical results have shown that it is possible for the transmission of a subwavelength hole of a certain size to become as high as 1.8 [100]. Transmission through arrays of small subwavelength cylindrical holes in thin metallic films has been studied with results up to twice Bethe's prediction [104, 107, 108, 109]. Another group reports on near-field optical transmission through of a large number of subwavelength holes with microscopically random separation distances, sizes, and shapes in a thin gold

film [110]. Other experiments have produced extraordinary near-field transmission with one-dimensional arrays of slits in metal films [99, 103] and flat arrays of metal films surrounded by periodic dielectrics [32, 105]. All of these periodic structures obtain enhanced transmission peaks that are generally thought to be the effect of the coupling of the incident light to surface plasmons using the grating of the surface for excitation [24, 110]. Although several analytical theories have been developed proposing that the high transmission is primarily due to waveguide mode resonance and the diffraction of evanescent waves produced by subwavelength features at the surface instead of by surface plasmon excitation [98, 111]. Developing the theory for transmission and reflection for the proposed NIM coupled waveguide system will augment this exciting field.

4.2.1 Derivation

Here we consider the transmission and reflection through the single-coupled waveguide system in the limiting case where $k_y = 0$ and $d_{in} \ll d_{out}$. However, to generalize the mode type, we found it convenient and necessary to index our κ parameter differently from Section 3.1, accounting for both cos and sin modes. Now,

$$\begin{aligned} {\kappa_j}^{(-)} &= \frac{j\pi}{d_{out}}, \\ {\kappa_j}^{(+)} &= \frac{j\pi}{d_{in}}. \end{aligned} \tag{4.23}$$

Thus, ${\kappa_j}^{(+)} \gg {\kappa_j}^{(-)}$ due to the considered limiting case. Accordingly, the I, J, and K matrices may be simplified as shown here,

$$\begin{aligned} {I_{lj}}^{(+)} &= \frac{\delta_{lj}}{2} d_{in} \\ {I_{lj}}^{(-)} &= \frac{2}{{\kappa_l}^{(+)}} (-1)^{l+1} \end{aligned} \tag{4.24}$$

$$
\begin{aligned}
{J_{lj}}^{(+)} &= 0 \\
{J_{lj}}^{(-)} &\simeq \frac{\delta_{lj}}{2} d_{out}
\end{aligned}
\tag{4.25}
$$

$$
\begin{aligned}
{K_{lj}}^{(+)} &\simeq {I_{lj}}^{(-)} \\
{K_{lj}}^{(-)} &= \frac{\delta_{lj}}{2} d_{out}
\end{aligned}
\tag{4.26}
$$

Putting these into Eqs. (4.17, 4.18, 4.19, 4.20), and separating out the $^{(+)}$ and $^{(-)}$ matrices there are a total of 8, $2N \times 2N$ dimensional matrices:

$$
1_R^{(-)} = \begin{pmatrix} \epsilon_{\parallel}^{(-)} \frac{2(-1)^{(l+1)}}{{\kappa_l}^{(+)}} & 0 \\ 0 & \frac{k_{z,j}^{(TE,-)} 2(-1)^{(l+1)}}{k {\kappa_l}^{(+)}} \end{pmatrix} \tag{4.27}
$$

$$
1_R^{(+)} = \begin{pmatrix} \epsilon_{\parallel}^{(-)} \frac{\delta_{lj} d_{in}}{2} & 0 \\ 0 & \frac{k_{z,j}^{(TE,+)} \delta_{lj} d_{in}}{2k} \end{pmatrix} \tag{4.28}
$$

$$
1_T^{(-)} = \begin{pmatrix} \epsilon_{\parallel}^{(-)} \frac{2(-1)^{(l+1)}}{{\kappa_l}^{(+)}} & 0 \\ 0 & -\frac{k_{z,j}^{(TE,-)} 2(-1)^{(l+1)}}{k {\kappa_l}^{(+)}} \end{pmatrix} \tag{4.29}
$$

$$
1_T^{(-)} = \begin{pmatrix} \epsilon_{\parallel}^{(+)} \frac{\delta_{lj} d_{in}}{2} & 0 \\ 0 & -\frac{k_{z,j}^{(TE,-)} \delta_{lj} d_{in}}{2k} \end{pmatrix} \tag{4.30}
$$

$$
2_R^{(-)} = \begin{pmatrix} i \frac{k_{z,j}^{(TM,-)}}{\kappa_j^{(TM,-)}} \frac{{\epsilon_{\parallel}}^{(-)}}{{\epsilon_{\perp}}^{(-)}} \frac{\delta_{lj} d_{out}}{2} & 0 \\ 0 & \frac{\delta_{lj} d_{out}}{2} \end{pmatrix} \tag{4.31}
$$

$$
2_R^{(+)} = \begin{pmatrix} 0 & 0 \\ 0 & \frac{2}{{\kappa_l}^{(+)}} (-1)^{(l+1)} \end{pmatrix} \tag{4.32}
$$

$$
2_T^{(-)} = \begin{pmatrix} -i \frac{k_{z,j}^{(TM,-)}}{\kappa_j^{(TM,-)}} \frac{{\epsilon_{\parallel}}^{(-)}}{{\epsilon_{\perp}}^{(-)}} \frac{\delta_{lj} d_{out}}{2} & 0 \\ 0 & \frac{\delta_{lj} d_{out}}{2} \end{pmatrix} \tag{4.33}
$$

$$2_T^{(+)} = \begin{pmatrix} 0 & 0 \\ 0 & \frac{2}{\kappa_l{}^{(+)}}(-1)^{(l+1)} \end{pmatrix} \tag{4.34}$$

While these matrices now look simply 2×2 dimensional, they are indeed still of size $2N \times 2N$. The entries with δ_{lj} are diagonal matrices, while the other non-zero matrix elements are singular matrices. To continue, we will now consider the TE and TM modes separately, as the mode polarizations decouple inside the waveguide. Note that the TEM mode can be considered as a specific TM mode case when $\kappa = 0$ and $E_z \propto \sin(\kappa x)$. Starting with the TE modes, the boundary condition Eqs. in (4.16) can be rewritten as:

$$\begin{cases} \dfrac{k_{z,j}{}^{(TE,-)} 2(-1)^{(l+1)}}{\kappa_l{}^{(+)}} \left(-T^{(-)} + R^{(-)}\right) = \dfrac{k_{z,j}{}^{(TE,+)} \delta_{lj} d_{in}}{2} \left(-T^{(+)} + R^{(+)}\right) \\ \dfrac{\delta_{lj} d_{out}}{2} \left(T^{(-)} + R^{(-)}\right) = \dfrac{2(-1)^{(l+1)}}{\kappa_j{}^{(+)}} \left(T^{(+)} + R^{(+)}\right) \end{cases} \tag{4.35}$$

When incident radiation is assumed from only the first mode on the left side; ($T_1 = \langle 1, 0, 0, 0, \cdots \rangle$; $R^{(+)} = 0$) the equations in (4.35) reduce to:

$$\begin{cases} \dfrac{k_{z,l}{}^{(TE,-)} (-1)^{(l+1)}}{\kappa_l{}^{(+)}} \left(-T^{(-)} + R^{(-)}\right) = -\dfrac{k_{z,l}{}^{(TE,+)} \delta_{lj} d_{in}}{4} T^{(+)} \\ \delta_{lj} \dfrac{d_{out}}{4} \left(T^{(-)} + R^{(-)}\right) = \dfrac{(-1)^{(l+1)}}{\kappa_j{}^{(+)}} T^{(+)} \end{cases} \tag{4.36}$$

Solving Eq. 4.36 for $R_j^{(-)}$ gives,

$$R_j{}^{(TE,-)} = \frac{4}{d_{out}} \left[\frac{(-1)^{(j+1)}}{\kappa_j{}^{(+)}} \sum_k T_k{}^{(TE,+)} \right] - T_j{}^{(TE,-)}. \tag{4.37}$$

Combining Eqs. (4.37, 4.36) obtains,

$$\frac{k_{z,l}{}^{(TE,-)}}{\kappa_l{}^{(+)}} (-1)^{(l+1)} \sum_j \left[-2T_j{}^{(TE,-)} + \frac{4}{d_{out}} \sum_k \frac{(-1)^{(j+1)}}{\kappa_j{}^{(+)}} T_k{}^{(TE,+)} \right] = \frac{-k_{z,l}{}^{(TE,+)} d_{in}}{4} T_l{}^{(TE,+)}. \tag{4.38}$$

Finally, solving this for ${T_l}^{(+)}$ reveals the desired expression for the transmission coefficients of the TE modes as a function of *all* the incident modes,

$$\begin{aligned} {T_l}^{(TE,+)} &\simeq 8\frac{{k_{z,l}}^{TE,-}}{{\kappa_l}^{(+)}}(-1)^{(l+1)}\frac{1}{d_{in}{k_{z,l}}^{(TE,+)}}\sum_j {T_j}^{(TE,-)} \\ &\quad -\frac{16}{{k_{z,l}}^{(TE,+)}d_{out}}\sum_j\frac{(-1)^{(j+1)}}{{\kappa_j}^{(+)}d_{in}}\sum_k {T_k}^{(TE,+)} \end{aligned} \tag{4.39}$$

We can analyze this result further by introducing b_l and a_l so that;

$$a_l = \frac{16}{{k_{z,l}}^{(TE,+)}d_{out}}\sum_j\frac{(-1)^{(j+1)}}{{\kappa_j}^{(+)}d_{in}}, \tag{4.40}$$

$$b_l = 8\frac{{k_{z,l}}^{TE,-}}{{\kappa_l}^{(+)}}(-1)^{(l+1)}\frac{1}{d_{in}{k_{z,l}}^{(TE,+)}}\sum_j {T_j}^{(-)}. \tag{4.41}$$

Now Eq. 4.39 can be written as,

$${T_l}^{(TE,+)} \simeq b_l - a_l\sum_k {T_k}^{(TE,+)}, \tag{4.42}$$

or written in the more revealing matrix form,

$$\begin{bmatrix} a_1+1 & a_1 & a_1 & \cdots \\ a_2 & a_2+1 & a_2 & \cdots \\ a_3 & a_3 & a_3+1 & \cdots \\ \vdots & \vdots & \vdots & \cdots \end{bmatrix}\begin{bmatrix} T_1^{(+)} \\ T_2^{(+)} \\ T_3^{(+)} \\ \vdots \end{bmatrix} = \begin{bmatrix} b_1 \\ b_2 \\ b_3 \\ \vdots \end{bmatrix}. \tag{4.43}$$

Numerically we found the $a_l \approx 0$, leaving ${T_l}^{(TE,+)} \approx b_l$. This is the result we used to verify the analytic TE transmission and reflection derived coefficients against the numerically calculated ones in the following section.

Similar analysis for the TM modes indicates that the approximation of $J^{(+)}$ (4.25) yields a disagreement in the numerical simulations so we reduce the $2_R^{(+)}$

and $2_T^{(+)}$ matrices (Eqs. 4.32, 4.34) to;

$$2_R^{(+)} = \begin{pmatrix} i\frac{{k_{z,j}}^{(TM,+)}}{\kappa_j{}^{(+)}}\frac{\epsilon_\parallel^{(+)}}{\epsilon_\perp^{(+)}}[J^{(+)}]_{l,j} & 0 \\ 0 & \frac{2}{\kappa_l{}^{(+)}}(-1)^{(l+1)} \end{pmatrix} \tag{4.44}$$

$$2_T^{(+)} = \begin{pmatrix} -i\frac{{k_{z,j}}^{(TM,+)}}{\kappa_j{}^{(+)}}\frac{\epsilon_\parallel^{(+)}}{\epsilon_\perp^{(+)}}[J^{(+)}]_{l,j} & 0 \\ 0 & \frac{2}{\kappa_l{}^{(+)}}(-1)^{(l+1)} \end{pmatrix} \tag{4.45}$$

This alteration does not effect the above TE calculations because the $J^{(+)}$ matrix is located only in the first column of Eqs. (4.32, 4.34), and therefore is only relavant for the TM modes. Again assuming that $R^{(+)} = 0$ for all moes and using the delta function to simplify things, the boundary conditions in Eq. 4.16 for the TM modes can be written in equation form as,

$$\begin{cases} \sum_j \frac{\epsilon_\parallel^{(-)} 2(-1)^{(l+1)}}{\kappa_l^{(+)}} \left(T_j^{(TM,-)} + R_j^{(TM,-)}\right) = \frac{\epsilon_\parallel^{(+)} d_{in}}{2} \left(R_l^{(TM,+)} + T_l^{(TM,+)}\right) \\ \sum_j \frac{ik_{z,j}{}^{(TM,+)}}{\kappa_j^{(+)}} \frac{\epsilon_\parallel^{(+)}}{\epsilon_\perp^{(+)}} \left[J^{(+)}\right]_{l,j} \left(T_j^{(TM,+)}\right) = i\frac{{k_{z,l}}^{(TM,-)} d_{out}}{2\kappa_l^{(-)}} \frac{\epsilon_\parallel^{(-)}}{\epsilon_\perp^{(-)}} \left(R_l^{(TM,-)} - T_l^{(TM,-)}\right) \end{cases} \tag{4.46}$$

Solving for $R_l^{(TM,-)}$ from the second equation in this system gives,

$$R_l^{(TM,-)} = T_l^{(TM,-)} - \frac{\kappa_l^{(-)}}{ik_{z,l}{}^{(TM,-)}} \frac{2}{d_{out}} \frac{\epsilon_\perp^{(-)}}{\epsilon_\parallel^{(-)}} \sum_j \left[i\frac{{k_{z,j}}^{(TM,+)}}{\kappa_j^{(+)}} \frac{\epsilon_\parallel^{(+)}}{\epsilon_\perp^{(+)}} \left[J^{(+)}\right]_{l,j} \left(T_j^{(TM,+)}\right) \right]. \tag{4.47}$$

Again, putting this relationship for the reflection coefficients into the first equation in Eq. 4.46 and solving for single l mode of transmission, $T_l{}^{(+)}$, reveals the desired expression for the transmission coefficients of the TM modes,

$$\begin{aligned} T_l^{(TM,+)} \simeq & \sum_j \frac{8(-1)^{(l+1)}}{d_{in}\kappa_l^{(+)}} \frac{\epsilon_\parallel^{(-)}}{\epsilon_\parallel^{(+)}} \left(T_j^{(TM,-)}\right) - \\ & \sum_j \left[\frac{8(-1)^{(l+1)}\kappa_j^{(-)}}{d_{in}d_{out}\kappa_l^{(+)}{k_{z,j}}^{(TM,-)}} \frac{\epsilon_\perp^{(-)}}{\epsilon_\perp^{(+)}} \sum_k \frac{{k_{z,k}}^{(TM,+)}}{\kappa_k^{(+)}} \left[J^{(+)}\right]_{j,k} \left(T_k^{(TM,+)}\right) \right]. \end{aligned} \tag{4.48}$$

Again, we found the second term in this expression for the transmission coefficients to be insignificant and approximate the TM transmission coefficients with the first term only. The following section compares these analytic results to numerically calculated results for the transmission and reflection through the proposed system of single coupled waveguides.

4.2.2 Results: Simulated versus Analytic

We analyze the transmission coefficients of the modes through and reflection coefficients from a single coupled waveguide as pictured in Figure 4.1 assuming a single normally incident mode (either TE or TM). When the radiation is normally incident the modes decouple and there is no mode mixing. Therefore, with a single TM incident mode, multiple TM modes may be transmitted and reflected but no TE modes will be excited and vice versa. The external waveguide thicknesss is varied from 2 μm to 50 μm while the internal waveguide thickness (d_{in} = 500 nm), the incident radiation wavelength is λ = 1.5 μm, and 60 waveguide modes remain constant for all the simulations below. The isotropic system considered has material parameters $\epsilon_\perp = \epsilon_\parallel = 2.0$ inside the smaller waveguide coupled on the left to a vacuum ($\epsilon_\perp = \epsilon_\parallel = 1.0$). While the anisotropic, nanowire core NIM system has electric permittivities $\epsilon_\perp = -3.909 + 0.1i$, $\epsilon_\parallel = 2.329 + 0.1i$ and is coupled to a larger Si waveguide with $\epsilon_\perp = \epsilon_\parallel = 13.0$. In all the figures below, the blue dots display the absolute value, or amplitude, of the numerically simulated transmission (or reflection) for selected modes, and the red line conveys the same for the analytical functions derived in Section 4.2.1.

4.2.2.1 Transmission Results

The transmission results can be summarized by three figures. Figure 4.3 contains plots for the anisotropic (a) and isotropic (b) single coupled waveguide systems with a single TM mode incident from an external waveguide of thickness 20 μm. The second TM mode was chosen as it is the first propagating mode inside the NIM waveguide. The simulation and theory agree nicely. Figure 4.4 shows the same TM mode transmission from a waveguide of thickness 10 μm. There appears to be a resonance occurring at about the third mode for both the anisotropic and

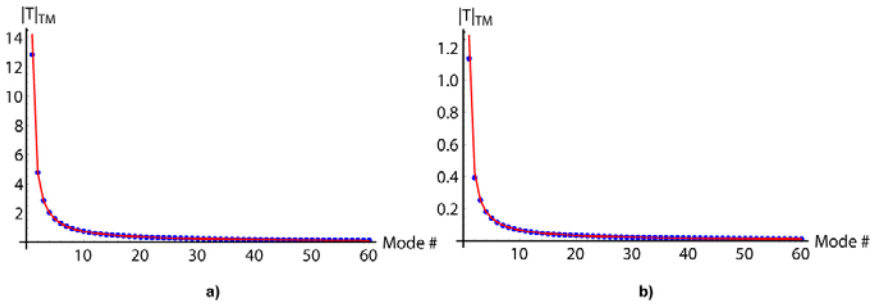

Figure 4.3: Amplitude of TM modal transmission for simulated (blue dots) and theoretical (red line) data for the single coupled waveguide system, $d_{in} = 500$ nm and $d_{out} = 20$ μm, for (a) anisotropic smaller waveguide and (b) isotropic system.

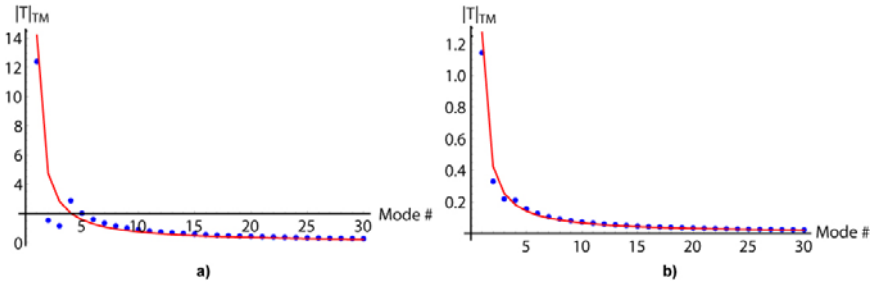

Figure 4.4: Amplitude of TM modal transmission for simulated (blue dots) and theoretical (red line) data for the single coupled waveguide system, $d_{in} = 500$ nm and $d_{out} = 10$ μm, for (a) anisotropic smaller waveguide and (b) isotropic system.

isotropic waveguides. This resonance needs to be further investigated as it only appears for external waveguide sizes < 20 μm when the coupled waveguide size is 500 nm. The case for TE mode incidence (1st mode chosen) is shown in Figure 4.5 for both systems with external waveguide size (d_{out}) of 10 μm. Once again, the theory and simulation agree, except for the lowest order modes. This could be due to the terms we approximated near zero in the expressions for transmission of the TM and TE modes above.

4.2.2.2 Reflection Results

Similarly, the reflection results are outlined in several figures. Figure 4.7 displays the amplitude of reflection of the TM modes for an (a) anisotropic and (b) isotropic single coupled waveguide system with only the second TM mode incident from the larger wavguide, $d_{out} = 10$ μm. The results match perfectly for the reflection of the

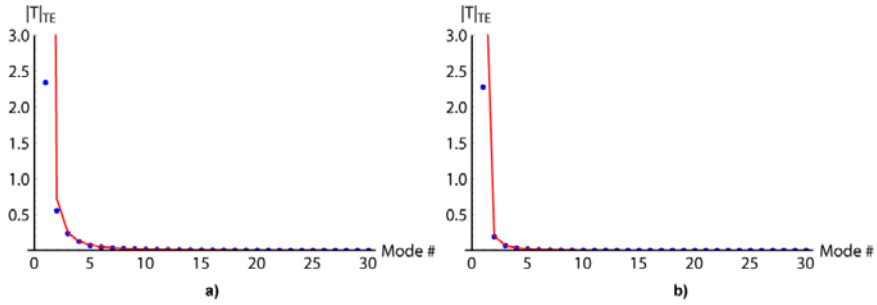

Figure 4.5: Amplitude of TE modal transmission for simulated (blue dots) and theoretical (red line) data for the single coupled waveguide system, $d_{in} = 500$ nm and $d_{out} = 10$ μm, for (a) anisotropic smaller waveguide and (b) isotropic system.

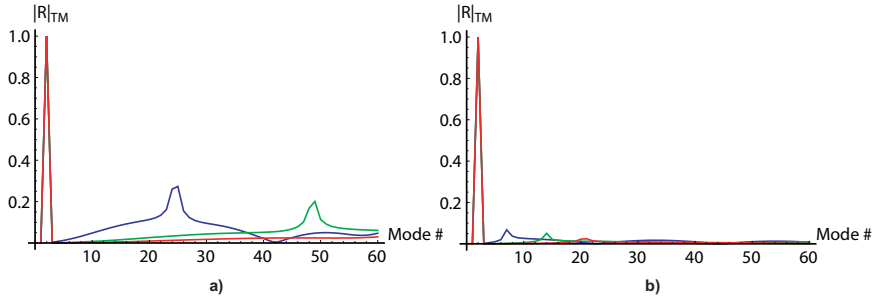

Figure 4.6: Amplitude of simulated TM modal reflection for coupled waveguides with $d_{in} = 500$ nm and $d_{out} = 10,\ 20$, and 30 μm corresponding to the blue, green, and red lines respectively; (a) anisotropic smaller waveguide and (b) isotropic system.

second mode but a resonance is apparent for larger modes in the simulated data for both systems. Inspecting only the TM reflection data from our simulations in both the isotropic and NIM systems for external waveguide sizes, $d_{out} = 10,\ 20$, and 30 μm, we found the resonance to be size-dependent as seen in Figure 4.6. The peaks are larger for small waveguides and occur at lower order modes for the isotropic waveguide system. In the derivation above, the reflection modes depend on the theoretical transmission modes (Eqs. 4.37, 4.47), hence the resonance peak is expected as it appeared in the transmission results as well. TE mode reflection is shown in Figure 4.8 for $d_{out} = 10$ μm with the first TE mode normally incident. Here the isotropic results agree except for the first mode, while the anisotropic results *only* agree for the first mode. This is suprising for the anisotropic case because the transmission results disagreed for the lower order modes, but matched

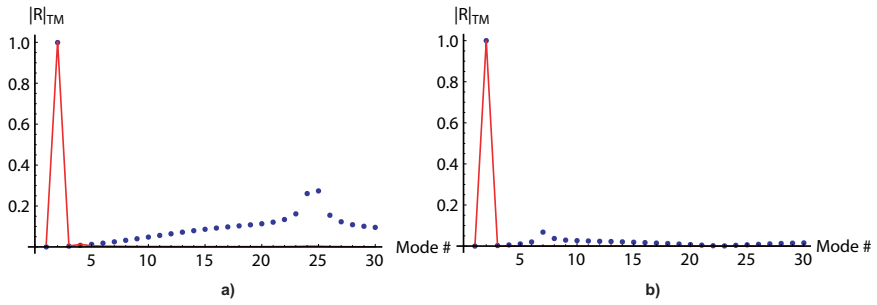

Figure 4.7: Amplitude of TM modal reflection for simulated (blue dots) and theoretical (red line) data for the single coupled waveguide system, $d_{in} = 500$ nm and $d_{out} = 10$ μm, for (a) anisotropic smaller waveguide and (b) isotropic system.

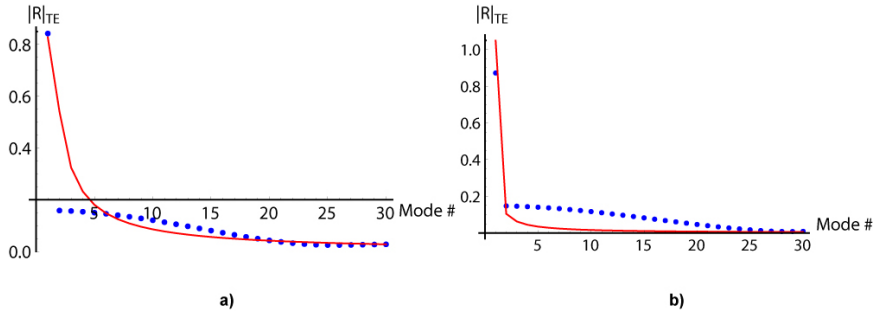

Figure 4.8: Amplitude of TE modal reflection for simulated (blue dots) and theoretical (red line) data for the single coupled waveguide system, $d_{in} = 500$ nm and $d_{out} = 10$ μm, for (a) anisotropic smaller waveguide and (b) isotropic system.

for the higher numbered modes. This behavior should be examined further as it is probably due to theoretical approximations, although that is not immediately evident.

4.3 Relaxation Method for Multiple Coupled Waveguides

A practical extension of the above simulations is to calculate the propagation of the electromagnetic fields from a micron-sized positive index waveguide, through the proposed nanoscale NIM system, back into another micron-sized positive index waveguide. In order to calculate the fields transmitting through and reflecting from multiple interfaces, we developed the relaxation-type algorithm described below. The $^{(-)}$ and $^{(+)}$ superscripts will still denote the isotropic and anisotropic waveguide parameters respectively, only now the anisotropic waveguide is sandwiched between

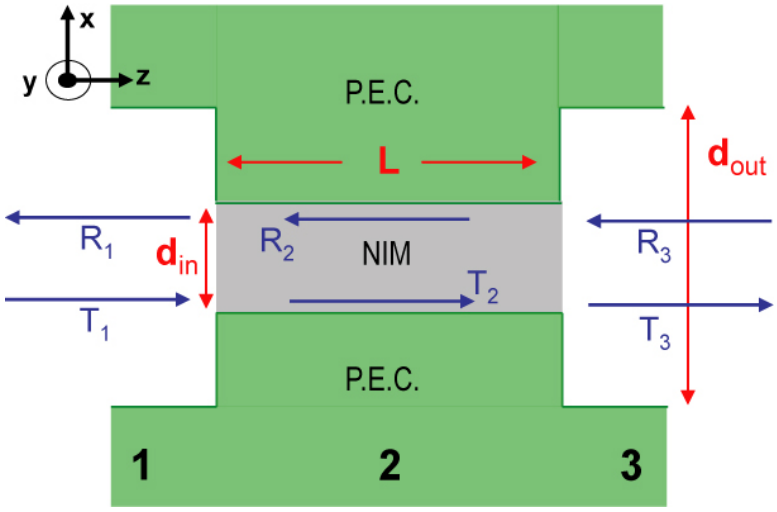

Figure 4.9: Schematic configuration (side-view) of the non-magnetic NIM waveguide coupled between two larger isotropic waveguides, surrounded above and below by a perfect electric conductor (PEC). The red double arrows dictate the sizes of the waveguides, while the blue arrows represent the incoming, reflected, and transmitted wave propagation with correspondingly labeled coefficients.

two isotropic waveguides. A schematic of this system is shown in Fig. 4.9.

The first step is to develop the transfer theory for the second interface, which is an exact inverse of the coupled interface derived in the previous section. Now the smaller NIM waveguide is on the left-hand side and the larger, positive-index waveguide on the right, therefore the known coeffiecient arrays are $T^{(+)}$ and $R^{(-)}$ for this interface, while the unknown arrays are $R^{(+)}$ and $T^{(-)}$ (see Fig. 4.9). Conveniently, the previously developed boundary conditions and the matrices created to combine the boundary condition equations remain the same for this inverted coupling. The system of equations in Eq. (4.16) can again be algebraically manipulated to now solve for the unknowns at this interface starting with $R^{(+)}$:

$$R^{(+)} = \frac{1}{1_R^{(+)}} \left[1_R^{(-)} R^{(-)} + 1_T^{(-)} T^{(-)} - 1_T^{(+)} T^{(+)} \right], \tag{4.49}$$

$$T^{(-)} = \frac{1}{\left[2_T^{(-)} - 2_R^{(+)}\left(1_R^{(+)}\right)^{-1} 1_T^{(-)}\right]} \left[\left(2_R^{(+)}\left(1_R^{(+)}\right)^{-1} 1_R^{(-)} - 2_R^{(-)}\right) R^{(-)} + \left(2_T^{(+)} - 2_R^{(+)}\left(1_R^{(+)}\right)^{-1} 1_T^{(+)}\right) T^{(+)}\right] \tag{4.50}$$

where again only the diagonal, easily invertable matrices are necessarily inverted.

To compute the fields through the system we start at the first interface, assuming incident radiation only from the left ($R^{(+)} = 0$), and calculate the transmission and reflection coefficients using Eqs. (4.21, 4.22). As the electromagnetic fields propagate in the z direction through the NIM from the first interface to the second, their phase changes accordingly with propagation constant, k_z. Therefore it is necessary to translate the transmission coefficients via a multiplicative mode-dependant term, $\exp(ik_{z,j}\Delta z)$, where Δz is the length of the NIM, to achieve an accurate value before performing calculations at the second interface. After the $R^{(+)}$ and $T^{(-)}$ coefficients have been determined at the back interface, the reflection ($R^{(+)}$) coefficients must be translated back in the $-z$ direction with a $\exp(-ik_{z,j}\Delta z)$ term. We then use these reflection coefficients from the right side of the first interface to re-calculate the coefficients at that interface and start the process over. We continue this loop between interfaces until a convergent solution to Maxwell's equations is found. The requirements for convergence are discussed in the next section.

4.3.1 Convergence of the Relaxation Method

The relaxation scheme presented above is necessary to reconcile the growing and decaying exponential terms ($\exp(ik_{z,j}\Delta z)$, $\exp(-ik_{z,j}\Delta z)$) utilized to transfer the coefficients along the NIM waveguide. Calculations, in particular, sums and differences of the these modes that have a relatively large imaginary component of their propagation constant, k_z'', in the nanoscale waveguide may result in enormous spreads in magnitude. Such a large magnitude difference in exponentially small and large terms may lead to a loss in accuracy due to the finite machine precision of the computer. Therefore, care must be taken to ensure the convergence of the relaxation method with consideration primarily on two factors: 1) the number of

times the relaxation loop is excecuted, and 2) using an adequate number of modes within the system.

The relaxation loop should be iterated through until the absolute values of the coefficients from the previous run-through match the absolute values of the current coefficients to within a very small error. To do this, the coefficient values are stored (${T_{iold}}^{(+)}$) before they are translated and compared at the start of the next iteration with the following expression:

$$\Delta T^{(+)} = \frac{\sum_i |{T_{iold}}^{(+)} - T_i^{(+)}|^2}{\sum_i |T_i^{(+)}|^2} \tag{4.51}$$

Once $\Delta T^{(+)} \lessapprox 10^{-25}$ the iteration loop may be exited. A similar definition and requirement is used to determine the convergence of the $R^{(+)}$ coefficients at the second interface. This method guarantees the solution is self-consistent.

Secondly, the total number of modes within the system must be high enough so that the fields on either side of the interfaces agree, satisfying the required boundary conditions. To verify that this occurs, we plot the cross-section along the x direction of the D_z, H_y, E_x and E_y fields at either side of the interface, with $y = 0$, for both z locations of the boundaries in question. Typically we find adequate matching of the fields for as low as $N = 20$ waveguide modes, but chose to run the simulations with a total of $N = 40$, 60, or 80 modes for better accuracy as determined by energy flux calculations.

4.3.2 Energy Flux Calculations for Validation

Conservation of energy can be used to validate the simulations and relaxation coding technique described above. We start by calculating the Poynting vector components separately for TE and TM modes for the incoming, reflected, and transmitted waves through the system. This is straightforward for the single interface coupling of two waveguides, however for double interface coupling as described in Section 4.3, we only consider the waves in the far left and far right waveguide regions and ignore the internal waveguide modes for this calculation. The energy flux vector components for the TE and TM mode polarizations are given by,

$$
\begin{aligned}
S_{TM} = \quad & \{-\tfrac{1}{\kappa {k_z}^2} i |A_j|^2 \epsilon_\parallel k \left(k_y^2 + k_z^2\right) \cos(\kappa x) \sin(\kappa x), \\
& \tfrac{1}{\epsilon_\perp \kappa^2 {k_z}^2} |A_j|^2 |\epsilon_\parallel|^2 \left(k_y^2 + k_z^2\right) k k_y \sin(\kappa x)^2, \\
& \left(k_y^2 + k_z^2\right) \tfrac{|A_j|^2 |\epsilon_\parallel|^2 k^2 \sin(\kappa x)^2}{\epsilon_\perp k \kappa^2 k_z}\}
\end{aligned} \tag{4.52}
$$

$$
\begin{aligned}
S_{TE} = \quad & \{-\tfrac{1}{k {k_z}^2} i |A_j|^2 \kappa \left(k_y^2 + k_z^2\right) \cos(\kappa x) \sin(\kappa x), \\
& \tfrac{1}{k {k_z}^2} |A_j|^2 k_y \left(k_y^2 + k_z^2\right) \cos(\kappa x) \cos(\kappa x), \\
& \tfrac{|A_j|^2 \left(k_y^2 + k_z^2\right) \cos(\kappa x) \cos(\kappa x)}{k k_z}\},
\end{aligned} \tag{4.53}
$$

where A_j represents either the transmission or reflection coefficient for a given mode with index, j. Each component expression in Eqs. (4.52, 4.53) can be simplified by assigning $\kappa = \frac{M\pi}{d}$ where M is an integer and d is the waveguide thickness, and then integrating the cos and sin functions symmetrically over d. Doing this reveals the zero x-component flux for both polarizations, as well as a zero y-component flux when considering normal incidence radiation ($k_y = 0$). Since our interest lies in the transmission of radiation in the z direction, we focus on the z-component of the energy flux shown here:

$$
S_{z,TM} = \quad \tfrac{|A_j|^2 |\epsilon_\parallel|^2 k \left(k_y^2 + k_z^2\right)}{2 \epsilon_\perp k_z \kappa^2} \tag{4.54}
$$

$$
S_{z,TE} = \quad \tfrac{|A_j|^2 \left(k_y^2 + k_z^2\right)}{2 k k_z}. \tag{4.55}
$$

For each mode polarization, we then sum over all modes, using appropriate coefficients for each waveguide region, to get a total energy flux for both TE and TM modes. The question arises why we do not consider the cross terms involving both TE and TM modes. The z component of this cross-term flux actually disappears. Starting from the total energy flux defined by the Poynting vector (ignoring constant prefactors), $\vec{S} = [\vec{E} \times \vec{H}]$ the total flux can be written,

$$
\begin{aligned}
\vec{E} \times \vec{H} &= (E^{(TM)} + E^{(TE)}) \times (H^{(TM)} + H^{(TE)})^* \\
&= (E^{(TM)} \times H^{(TM)^*}) + (E^{(TE)} \times H^{(TM)^*}) \\
&\quad + (E^{(TM)} \times H^{(TE)^*}) + (E^{(TE)} \times H^{(TE)^*})
\end{aligned} \tag{4.56}
$$

where the first and last terms are the TM and TE modal fluxes from Eqs.(4.53, 4.52) respectively. The z component of the first cross term is easily shown to be zero from looking at Eq. 3.1 and noting that the x component is zero in both E^{TE} and H^{TM}. The second cross term z component,

$$(E^{(TM)} \times H^{(TE)^*})_z = E_x^{(TM)} H_y^{(TE)^*} - E_y^{(TM)} H_x^{(TE)^*}$$

is slightly trickier but can be shown to cancel out as well. After some algebra using Eqs.(3.3, 3.4), keeping in mind that $\kappa^{(TM)} = \kappa^{(TE)}$, $E_0^{(TM)} = E_0^{(TE)} = E_0$, and assuming $E_0 \propto \cos(\kappa x)$ will show a cancellation of terms. Since the cross terms disappear, we can simply add the summed TE and TM fluxes together in each waveguide region to obtain a total incident, transmitted, and reflected flux. Dividing both the total transmitted and reflected flux by the total incoming flux reveals two ratios that when summed together should equal unity in a lossless system. These ratios must be multiplied by a factor of the ratio of waveguide sizes when the sizes differ in the regions of calculated flux, such as for the single coupled system. This simple calculation determines that the simulations are truly physical and aids in checking accuracy of the computations.

4.4 Isotropic RHM Results

Since the general behavior of right-handed, conventional media inside a waveguide is well-known, the following calculations were done with several expectations in mind. These expectations include finding the transmission through the waveguide to be cut off as a function of waveguide radius and also that the transmitted field would fall subject to the diffraction limit.

We consider the isotropic system consisting of a 5 μm long internal waveguide filled with air ($\epsilon_\parallel = \epsilon_\perp = 1.0$), coupled on both sides to a 1 μm-thick silicon outer waveguide, with electric permittivities $\epsilon_\parallel = \epsilon_\perp = 13.0$. Absorption is neglected. Using 80 waveguide modes and assuming only the first TM mode of radiation is incident from the left, a series of simulations are done varying the external waveguide thickness, d_{out}, and the internal (air) waveguide thickness, d_{in}. For each simulation performed, d_{out} is held constant as the relaxation technique is conducted for values of d_{in} ranging from 1 nm to d_{out} in increments of 0.5 nm.

The total incident flux from the left-most waveguide (region 1 in Fig 4.9), as well as the transmitted and reflected fluxes from region 3 are exported and stored in corresponding data files for each simulation.

Compiling the simulation results and plotting the transmission through the isotropic coupled system as a function of internal waveguide widths reveals noticable transmission values for d_{in} greater than 700 nm as shown in (a) of Fig. 4.10. The plot in Fig. 4.10 (b) shows the optical range of interest, internal waveguide sizes between 400 nm and 700 nm, where it appears there is no transmission as expected. Taking a closer look at this range, we find that although the transmission is near zero, the ln-ln plot of transmission intensity as a function of internal waveguide size reveals a power-law relationship as shown in Fig. 4.11. Further work needs to be done to verify the convergence of the values taking into account numerical precision because transmission values are extremely small.

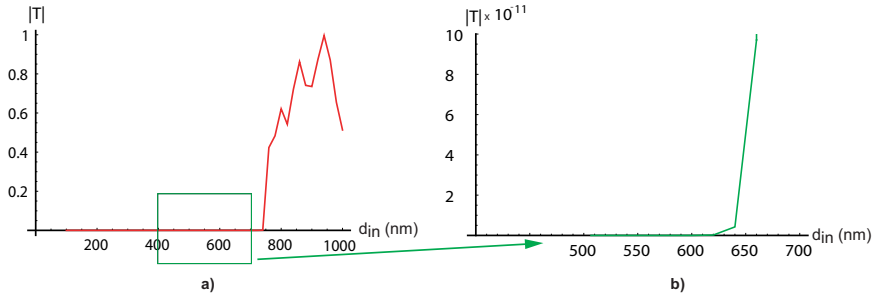

Figure 4.10: Transmission through an isotropic coupled planar waveguide system with an external waveguide size of 1000 nm as a function of internal waveguide size for (a) the entire d_{out} range and (b) the 500 nm to 700 nm range.

4.5 Anisotropic NIM Results

The more interesting case to study is when the proposed NIM, anisotropic dielectric-filled waveguide is coupled between a micron-sized silicon waveguide ($\epsilon_{\|} = \epsilon_{\perp} = 13.0$). The calculated permittivities of the nanowired metamaterial inside the left-handed waveguide include a small absorption; $\epsilon_{\|} = 2.329 + 0.1i$ and $\epsilon_{\perp} = -3.909 + 0.1i$. The resulting index of refraction, n, depends on both d_{in} and the mode number from $\varkappa$ in the definitions (3.7) and (3.8). The index of refraction ranges from $-9.5 + .33i$ to $-1.4 + .1i$ for the first TM mode and $-5.47 + .2i$ to $-2.13 + .11i$ for the second TM mode as d_{in} is varied from 1 nm to 1000 nm.

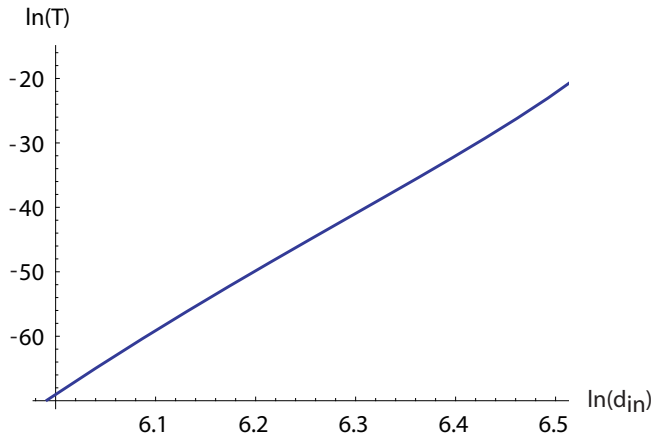

Figure 4.11: Ln-ln plot of transmission through an isotropic planar waveguide system as a function of internal waveguide size to reveal a power law relationship for the transmission.

Assuming only the first TM mode is normally incident ($k_y = 0$) from the left with wavelength, $\lambda = 1500$ nm, a series of simulations are done varying the length of the NIM waveguide, Δz, the external waveguide thickness, d_{out}, and the internal (NIM) waveguide thickness, d_{in}. For each simulation performed, Δz and d_{out} are held constant as the relaxation technique is conducted for values of d_{in} ranging from 1 nm to d_{out} in increments of .5 nm. Again, the total incident flux from region 1, and transmitted and reflected flux calculations from region 3 are exported and stored in corresponding data files for each simulation. We can use this data to analyze transmission through the coupled NIM waveguide system.

4.5.1 Modal Peaks

Figure 4.12 plots transmission through the system as a function of internal waveguide size. Note that transmission occurs for waveguide sizes smaller than $\lambda/2$, in contrast to the results from the isotropic system studied above. In (a) we suspect the two peaks to be due to the two most prominant TM modes: the first and second order modes. A revealing three dimensional surface plot of the transmission is shown in (b) of Figure 4.13, where the natural log of the transmission is plotted as a function of waveguide length, L, and internal waveguide size, d_{in}. The peak ridges are colored accordingly to match those in Figure 4.12 (a). Simulations calculating k_z'' for the dominate propagating mode of given waveguide sizes indicate

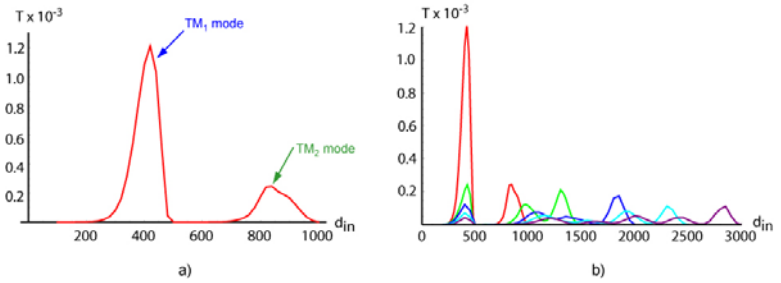

Figure 4.12: Transmission through the anisotropic NIM internal waveguide as a function of internal waveguide size. (a) Internal waveguide size of 1000 nm. The first peak at $d_{in} \approx 400$ nm is proved to be due to the first TM mode while the second peak at $d_{in} \approx 800$ nm is due to the second TM mode. (b) Transmisson peaks corresponding to internal waveguides sizes of 1000 nm (red), 1500 nm (green), 2000 nm (blue), 2500 nm (turquois), 3000 nm (purple).

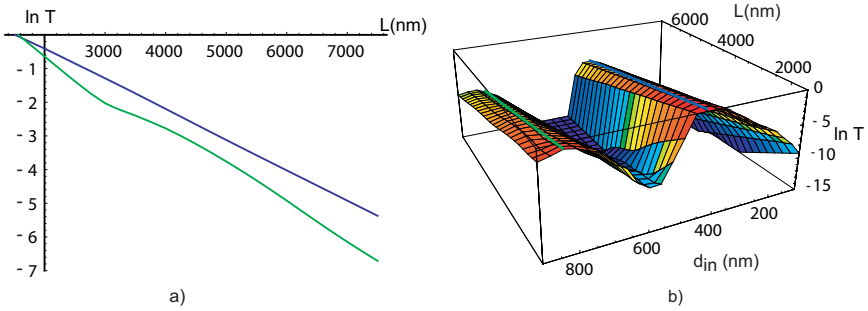

Figure 4.13: (a) The semi-log plot of transmission through the anisotropic NIM internal waveguide for $d_{in} = 400$ nm (blue) and $d_{in} = 800$ nm (green) as a function of internal waveguide length. (b) The three-dimensional surface plot of $ln(T)$ as a function of L and d_{in} where the peaks correspond to the lines in (a).

that the transmission peaks occur at the minima of k_z'', or when the dissipation of the wave is smallest. The plot in Figure 4.12 (b) shows the transmission peaks corresponding to various internal waveguide sizes ranging from $d_{in} = 1000$ nm to 3000 nm in increments of 500 nm. The primary peaks align nicely, while the secondary peak appears to converge to what we suspect to be the minimum k_z'' for the second most dominant TM mode. The relationship between the transmission peaks and the dissipation minimum should be further explored.

4.5.2 Exponential Dependence of Transmission

The three dimensional surface plot in Figure 4.13 (b) provides insight to the NIM waveguide length dependence of the transmission. The linear relationship seen in the semi-log plot in (a) reveals an exponential relationship between the transmission of the electromagnetic fields through our NIM waveguide as a function of waveguide length. The slope, m, of the blue (top) line, corresponding to the peak located at $d_{in} \sim 400$ nm, is numerically calculated to be -9.0×10^{-4}, while the slope of the green (bottom) line, corresponding to the peak located at $d_{in} \sim 800$ nm, is -1.1×10^{-3}. Since the transmission is proportional to the intensity of the electromagnetic field, and the intensity is proportional to the square of the field's magnitude, simple logarithmic math shows that m /2 of for each line is directly related to the field decay as a function of waveguide length. The absorption of the field can be found by inspecting the imaginary part of the propagating wave vector which in this case is k_z''. In order verify the relationship between slope and field attenuation, we found the values for k_z'' for both the first and second TM modes inside the NIM waveguide, as we believe the transmission peaks to correspond to these modes. For the first TM mode, ${k_{z,1}}'' = 4.5 \times 10^{-4}i$ and for the second, ${k_{z,2}}'' = 5.5 \times 10^{-4}i$. It is apparent that these numeric values are almost exactly equal to half of the slope values, m, listed above for the coinciding modal lines in the semi-log plot. This result confirms that the transmission peaks correlate directly to the prominant propagating modes inside the NIM waveguide.

4.6 Imaging through Coupled System

As an extension of the planar lens imaging described in Section 3.6 we model the imaging through the proposed coupled waveguide system, with the internal waveguide being a NIM. The problem now becomes three-dimensional as we want to measure the imaging in multiple $y - z$ planes. We assume an incident mode for all y values, but only a single x-direction mode. The arrays for k_z values as well as the reflection and transmission coefficients are now two-dimensional. We loop over the k_y values and calculate the $2N \times 2N$ matrices representing the boundary conditions for each k_y. The transmission and reflection coefficients are calculated and appended to appropriate arrays before the loop is iterated. After a solution

converges, the fields are calculated in each waveguide region summing over the transmission and reflection mode coefficients. The field distribution is illustrated by performing a density plot of the field intensity throughout the system for a single $y-z$ plane. A particular imaging plane is shown in Figure 4.14 using a single slit source and 15 waveguide modes for the simulation. The system consists of a 400 nm nanolayer NIM core lens with effective index of refraction, $n = -2.084 + 0.17i$, coupled on either end to a 1 μm thick silicon waveguide.

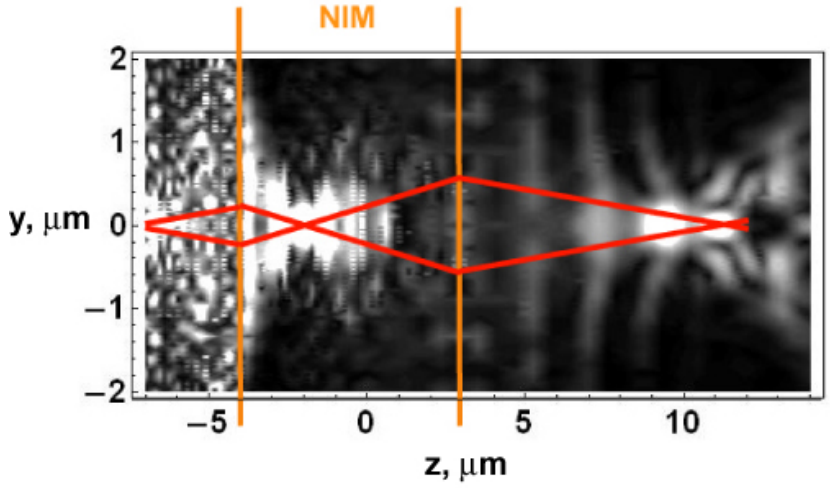

Figure 4.14: Imaging by a planar NIM-based lens coupled between two 1 μm thick Si-filled planar waveguides; Single slit source $w = 0.25$ μm located at $z = -7$ μm; NIM region thickness $d = 0.4$ μm: planar waveguide with nanolayer core material described in Fig. 3.5.1 with small absorption. The NIM region is between $z = -4$ μm and $z = 3$ μm.

4.7 Concluding Remarks

This purpose of this chapter was to explore the single and double coupling of micro-scale isotropic planar waveguides to and from the proposed subwavelength NIM waveguides. We began by describing the details of our simulation design to calculate the propagation of the electromagnetic fields through the a single

interface of two different-sized coupled planar waveguides in Section 4.1. Assuming an existing number of waveguide modes, solving the boundary equations derived from Maxwell's equations for each mode, and then summing over all TE and TM modes, the total field in each region can be constructed. This method includes large matrices and arrays which become numerically intensive.

Section 4.2 walks through the analytical derivation of expressions for the transmission through and reflection from such a single coupled waveguide system separately for the TE and TM modes as they decouple with normal radiation incidence. We present results of the theory compared to our numerical simulations for a several system configurations. The transmission data agrees nicely for higher order modes for all d_{out} values of both TE and TM cases. For TM transmission with $d_{out} < 20$ μm a resonance peak occurs within the lower modes of the simulated data differing from the derived theory in both the anisotropic and isotropic systems. This resonance occurs in the higher modes of the TM reflection data while the lower modes match almost perfectly. Both transmission and reflection of the lower TE modes disagree with the theory (an exception being the first reflected TE mode). Further investigation of our theoretical derivations including exploration of the numerical precision of the approximated term could lead to improved results.

An extension of the single waveguide coupling is to join the nanoscale NIM waveguide on both sides with isotropic micron-sized waveguides. We developed a relaxation technique to iterate between the interfaces, satisfying the boundary conditions at each intereface until a convergent solution for the fields is found. We verify our solutions are physical with energy flux calculations on either side of the system. Results are compared for transmission through a completely isotropic double coupled setup versus the configuration with an internal anisotropic, NIM waveguide. Transmission through the anisotropic system is 27 orders of magnitude greater than transmission through isotropic media for smaller (~ 400 nm) waveguide thickness. Transmission peaks occur at specific internal waveguide sizes and an exponential dependence of the transmission intensity on waveguide length is verified. While the location of these peaks vary in d_{in} depending on the external waveguide size chosen, they are strongly linked to the dominant propagating modes in the NIM waveguide. Lastly, we outline an algorithm for simulating imaging through a particular NIM coupled waveguide system and produce a corresponding density plot of the electromagnetic field intensity.

Bibliography

[1] V.A. Podolskiy and E.E. Narimanov. Strongly anisotropic waveguide as a non-magnetic left-handed system. *Phys. Rev. B*, 71:201101(R)–1–4, 2005.

[2] V.G. Veselago. The electrodynamics of substances with simultaneously negative values of ϵ and μ. *Soviet Physics Uspekhi*, 10:509–514, 1968.

[3] John B. Pendry and David R. Smith. Reversing Light with Negative Refraction. *Physics Today*, pages 37–43, Jun 2004.

[4] J. B. Pendry. Negative refraction makes a perfect lens. *Phys. Rev. Lett.*, 85(18):3966, 2000.

[5] N. Fang, H. Lee, C. Sun, and X. Zhang. Sub-Diffraction-Limited Optical Imaging with a Silver Superlens. *Science*, 308:534–537, April 2005.

[6] W. Cai, U.K. Chettiar, A.V. Kildishev, and V.M Shalaev. Optical cloaking with metamaterials. *Nature Photonics*, 1:224–227, April 2007.

[7] H. Shin and S. Fan. All-angle negative refraction for surface plasmon waves using a metal-dielectric-metal structure. *Phys. Rev. Lett.*, 96:073907, 2006.

[8] Mukesh P. Joshi, Haridas E. Pudavar, J. Swiatkiewicz, P. N. Prasad, and B. A. Reianhardt. Three-dimensional optical circuitry using two-photon-assisted polymerization. *Applied Physics Letters*, 74(2):170–172, 1999.

[9] H. Nishihara, M. Haruna, and T. Suhara. *Optical Integrated Circuits*. McGraw-Hill Professional, 1989.

[10] F. B. McCormick and Michael E. Prise. Optical circuitry for free-space interconnections. *Appl. Opt.*, 29:2013, 1990.

[11] M. Born and E Wolf. *Principles of Optics*. Oxford, 1989.

[12] E. Abbe. *Arch. Mikrosk. Anat.*, 9:413, 1873.

[13] David M. Walba. Fast Ferroelectric Liquid-Crystal Electrooptics. *Science*, 270(5234):250, 1995.

[14] Sergei F. Mingaleev and Yuri S. Kivshar. Nonlinear transmission and light localization in photonic-crystal waveguides. *J. Opt. Soc. Am. B*, 19:2241–2249, 2002.

[15] Qianfan Xu, Bradley Schmidt, Sameer Pradhan, and Michal Lipson. Micrometre-scale silicon electro-optic modulator. *Nature*, 435:325, 2005.

[16] Mehmet Fatih Yanik, Shanhui Fan, Marin Soljačić, and J. D. Joannopoulos. All-optical transistor action with bistable switching in a photonic crystal cross-waveguide geometry. *Opt. Lett.*, 28(24):2506–2508, 2003.

[17] L.D. Landau, E.M. Lifshitz, and L.P. Pitaevskii. *Course of Theoretical Physics*. Reed Ltd, Oxford, 2nd edition, 1996.

[18] Cheng-Wei Qiu, Hai-Ying Yao, Le-Wei Li, Said Zouhdi, and Tat-Soon Yeo. Routes to left-handed materials by magnetoelectric couplings. *Physical Review B*, 75(24):245214, 2007.

[19] Horace Lamb. *Proc. London Math Soc.*, 1:473–479, 1904.

[20] Henry Pocklington. *Nature*, 71:607, 1905.

[21] Arthur Schuster. *An Introduction to the Theory of Optics*. Edward Arnold, London, 1904.

[22] Dmitriy Sivukhin. *V. Opt. Spektrosk*, 3:308–312, 1957.

[23] Michael P. Marder. *Condensed Matter Physics*. John Wiley and Sons Inc., corrected printing edition, 2000.

[24] H. Raether. *Excitation of Plasmons and Interband Transitions by Electrons*. Springer, Berlin, 1st edition, 1980.

[25] R. Wangberg, J. Elser, E.E. Narimanov, and V.A. Podolskiy. Nonmagnetic nanocomposites for optical and infrared negative-refractive-index media. *J. Opt. Soc. Am. B*, 23:498, 2006.

[26] J.D. Jackson. *Classical Electrodynamics*. John Wiley and Sons Inc., 3rd edition, 1999.

[27] S Anantha Ramakrishna. Optical negative-index metamaterials. *Rep. Prog. Phys.*, 68:449–521, 2005.

[28] Zhang, Yong, B. Fluegel, and A. Mascarenhas. Total negative refraction in real crystals for ballistic electrons and light. *Phys. Rev. Lett.*, 91(15):157404, Oct 2003.

[29] P.A. Belov. Backward waves and negative refraction in uniaxial dielectrics with negative dielectric permittivity along the anisotropy axis. *Microwave Opt. Tech. Lett.*, 37:259–263, 2003.

[30] David R. Smith and John B. Pendry. Homogenization of metamaterials by field averaging (invited paper). *J. Opt. Soc. Am. B*, 23(3):391–403, 2006.

[31] John B. Pendry. Negative Refraction. *Contemporary Physics*, 45:191, 2004.

[32] J.T. Shen and P.M Platzmann. Near Field Imaging with Negative Dielectric Constant Lenses. *Appl. Phys. Lett.*, page 3286, 2002.

[33] L.D. Landau and E.M. Lifshitz. *Electrodynamics of Continuous Media*. Pergamon Press, Oxford, 2nd edition, 1984.

[34] J. Elser, V.A. Podolskiy, I. Avrutsky, and I. Salakhutdinov. Nonlocal effects in effective-medium response of nanolayerd metamaterials. *App. Phys. Lett.*, 90:191109, 2007.

[35] S. Foteinopoulou and C. M. Soukoulis. Negative refraction and left-handed behavior in two-dimensional photonic crystals. *Phys. Rev. B*, 67(23):235107, Jun 2003.

[36] P.V. Parimi, W.T. Lu, Plarenta Vodo, and Srinivas Sridhar. Photonic crystals: Imaging by flat lens using negative refraction. *Nature*, 426:404, 2003.

[37] Alexey Sukhovich, Li Jing, and John H. Page. Negative refraction and focusing of ultrasound in two-dimensional phononic crystals. *Physical Review B (Condensed Matter and Materials Physics)*, 77(1):014301, 2008.

[38] John B. Pendry. Calculating Photonic Band Structure. *Phys. Condens. Matter*, 8:1085, 1996.

[39] E. Yablonovitch. Photonic Band-gap Crystals. *Phys. Condens. Matter*, 5:2443, 1993.

[40] A.K. Sarychev and V.M. Shalaev. *Phys. Rep.*, 335:275, 2000.

[41] J B Pendry, A J Holden, D J Robbins, and W J Stewart. Low frequency plasmons in thin-wire structures. *Journal of Physics: Condensed Matter*, 10(22):4785–4809, 1998.

[42] J.B. Pendry, A.J. Holden, W.J. Stewart, and I. Youngs. Extremely Low Frequency Plasmons in Metallic Mesostructures. *Phys. Rev. Lett.*, 76(25):4773–4776, Jun 1996.

[43] D.F. Sievenpiper, M.E. Sickmiller, and E. Yablonovitch. 3D Wire Mesh Photonic Crystals. *Phys. Rev. Lett.*, 76(14):2480–2483, Apr 1996.

[44] J.B. Pendry, A.J. Holden, D.J. Robbins, and W.J. Stewart. Magnetism from conductors and enhanced nonlinear phenomena. *Microwave Theory and Techniques, IEEE Transactions on*, 47(11):2075–2084, Nov 1999.

[45] D. R. Smith, Willie J. Padilla, D. C. Vier, S. C. Nemat-Nasser, and S. Schultz. Composite medium with simultaneously negative permeability and permittivity. *Phys. Rev. Lett.*, 84(18):4184–4187, May 2000.

[46] C. G. Parazzoli, R. B. Greegor, K. Li, B. E. C. Koltenbah, and M. Tanielian. Experimental verification and simulation of negative index of refraction using snell's law. *Phys. Rev. Lett.*, 90(10):107401, Mar 2003.

[47] R. A. Shelby, D. R. Smith, and S. Schultz. Experimental Verification of a Negative Index of Refraction.

[48] W.J. Padilla, D.N. Basov, and D.R. Smith. Negative refractive index metamaterials. *Materials Today*, 9:28, 2006.

[49] Zhang. Midinfrared resonant magnetic nanostructures exhibiting a negative permeability. *Phys. Rev. Lett.*, 94:037402, 2005.

[50] S. Linden. Magnetic response of metamaterials at 100terahertz. *Science*, 306:1351–1353, 2004.

[51] C. Enkrich. Magnetic metamaterials at telecommunication and visible frequencies. *Phys. Rev. Lett.*, 95:203901, 2005.

[52] H.K. Yuan, U. K. Chettiar, W. Cai, A. V. Kildishev, A. Boltasseva, V. P. Drachev, and V. M. Shalaev. A negative permeability material at red light. *Opt. Express*, 15:1076–1083, 2006.

[53] Alexander A. Govyadinov, Viktor A. Podolskiy, and M. A. Noginov. Active metamaterials: Sign of refractive index and gain-assisted dispersion management. *Applied Physics Letters*, 91(19):191103, 2007.

[54] Tom G. Mackay and Akhlesh Lakhtakia. Comment on "negative refraction at optical frequencies in nonmagnetic two-component molecular media". *Phys. Rev. Lett.*, 96(15):159701, 2006.

[55] Yi-Fan Chen, Peer Fischer, and Frank W. Wise. Negative refraction at optical frequencies in nonmagnetic two-component molecular media. *Phys. Rev. Lett.*, 95(6):067402, 2005.

[56] Martin W McCall, Akhlesh Lakhtakia, and Werner S Weiglhofer. The negative index of refraction demystified. *European Journal of Physics*, 23(3):353–359, 2002.

[57] V.Pokrovsky and A.Efros. *Solid State Comm.*, 124:283, 2002.

[58] S. A. Ramakrishna and O. J. Martin. Resolving the wave vector in negative refractive index media. *Opt. Lett.*, 30:2626, 2005.

[59] Yi-Fan Chen, Peer Fischer, and Frank W. Wise. Chen, Fischer, and Wise reply:. *Physical Review Letters*, 96(15):159702, 2006.

[60] M. A. Noginov, V. A. Podolskiy, G. Zhu, M. Mayy, M. Bahoura, J. A. Adegoke, B. A. Ritzo, and K. Reynolds. Compensation of loss in propagating surface plasmon polariton by gain in adjacent dielectric medium. *Opt. Express*, 16(2):1385–1392, 2008.

[61] V.M. Shalaev. Negative index of refraction in optical metamaterials. *Opt. Lett.*, 30:3356–3358, 2005.

[62] V.A. Podolskiy, A.K. Sarychev, and V.M. Shalaev. Plasmon modes in metal nanowires and left-handed materials. *J. Nonlin. Opt Phys. Mater.*, 11:65–74, 2002.

[63] R. A. Shelby, D. R. Smith, S. C. Nemat-Nasser, and S. Schultz. Microwave transmission through a two-dimensional, isotropic, left-handed metamaterial. *Applied Physics Letters*, 78(4):489, 2001.

[64] A.A. Houck, J.B. Brock, and I.L Chuang. Experimental observations of a left-handed material that obeys snell's law. *Phys. Rev. Lett.*, 90(13):137401, Apr 2003.

[65] S. Zhang. Experimental demonstration of near-infrared negative-index metamaterials. *Phys. Rev. Lett.*, 95:137404, 2005.

[66] S. Zhang. Demonstration of metal-dielectric negative-index metamaterials with improved performance at optical frequencies. *J. Opt. Soc. Am. B.*, 23:434–438, 2006.

[67] G. Dolling. Low-loss negative-index metamaterial at telecommunications wavelengths. *Opt. Lett.*, 31:1800–1802, 2006.

[68] J. B. Pendry. A Chiral Route to Negative Refraction. *Science*, 306:1353, Nov 2004.

[69] V. M. Agranovich, Yu. N. Gartstein, and A. A. Zakhidov. Negative refraction in gyrotropic media. *Physical Review B*, 73(4):045114, 2006.

[70] Cheng-Wei Qiu, Le-Wei Li, Hai-Ying Yao, and Said Zouhdi. Properties of faraday chiral media: Green dyadics and negative refraction. *Physical Review B*, 74:115110, 2006.

[71] Cheng-Wei Qiu, Hai-Ying Yao, Le-Wei Li, Said Zouhdi, and Tat-Soon Yeo. Backward waves in magnetoelectrically chiral media: Propagation, impedance, and negative refraction. *Physical Review B*, 75:155120, 2007.

[72] V.A. Podolskiy and E.E. Narimanov. Near-sighted superlens. *Opt. Letters*, 30(1):75–77, 2005.

[73] J. W. Lee, M. A. Seo, J. Y. Sohn, Y. H. Ahn, D. S. Kim, S. C. Jeoung, Ch. Lienau, and Q-Han Park. Invisible plasmonic meta-materials through impedance matching to vacuum. *Opt. Express*, 13(26):10681–10687, 2005.

[74] Nicholas Kuhta, Viktor Podolskiy, and Alexei Efros. Far-field imaging by a planar lens: Diffraction versus superresolution. *Phys. Rev. B*, 76:205102, Nov 2007.

[75] R.H. Ritchie. Plasma Losses by Fast Electrons in Thin Films. *Phys. Rev.*, 106:874–881, 1957.

[76] W.L. Barnes, A. Dereux, and T.W. Ebbesen. Surface plasmon subwavelength optics. *Nature*, 424:824, 2003.

[77] E. Cubukcu, K. Aydin, E. Ozbay, S. Foteinopolou, and C.M. Soukoulis. Subwavelength Resolution in a Two-Dimensional Photonic-Crystal-Based Superlens. *Phys. Rev. Lett.*, 91(20):207401, Nov 2003.

[78] Viktor Podolskiy, Nicholas Kuhta, and Graeme Milton. Optimizing the superlens: Manipulating geometry to enhance the resolution. *App. Phys. Lett.*, 87:231113, 2005.

[79] David J. Griffiths. *Introduction to Electrodynamics*. Prentice Hall, Inc., 3rd edition edition, 1999.

[80] Jie Lu, Tomasz Grzegorczyk, Yan Zhang, Joe Pacheco Jr., Bae-Ian Wu, Jin Kong, and Min Chen. Čerenkov radiation in materials with negative permittivity and permeability. *Opt. Express*, 11(7):723–734, 2003.

[81] Chiyan Luo, Mihai Ibanescu, Steven G. Johnson, and J. D. Joannopoulos. Cherenkov radiation in photonic crystals. *Science*, 299:368, 2003.

[82] N. Garcia and M. Nieto-Vesperinas. Left-handed materials do not make a perfect lens. *Phys. Rev. Lett.*, 88(20):207403, 2002.

[83] J.B. Pendry. Comment on ıleft-handed materials do not make a perfect lensȷ. *Phys. Rev. Lett.*, 91(9):099701, 2003.

[84] M. Nieto-Vesperinas and N. Garcia. Nieto-vesperinas and garcia reply:. *Phys. Rev. Lett.*, 91(9):099702, 2003.

[85] P. M. Valanju, R. M. Walser, and A. P. Valanju. Wave refraction in negative-index media: Always positive and very inhomogeneous. *Phys. Rev. Lett.*, 88(18):187401, 2002.

[86] Leonid V. Alekseyev and Evgenii Narimanov. Slow light and 3D imaging with non-magnetic negative index systems. *Opt. Express*, 14:11184–11193, 2006.

[87] A. Lewis, H. Taha, A. Strinkovski, A. Manevitch, A. Khatchatouriant, R. Deckhter, and E. Ammann. Near-field optics: from subwavelength illumination to nanometric shadowing. *Nat. Biotechnol.*, 21:1378, 2003.

[88] A.A Govyadinov and V.A. Podolskiy. Metamaterial photonic funnels for subdiffraction light compression and propagation. *Phys. Rev. B*, 73:155108, 2006.

[89] K.F Riley, M.P. Hobson, and S.J Bence. *Mathematical Methods for Physics and Engineering*. Cambridge University Press, 2nd edition, 2002.

[90] V.A. Podolskiy, L. Alekseyev, and E.E. Narimanov. Strongly anisotropic media: the thz perspectives of left-handed materials. *J. Mod. Opt.*, 52(16):2343–2349, 2005.

[91] P.Yeh, A.Yariv, and C.Hong. *J. Opt. Soc. Am.*, 67:423, 1977.

[92] A.A Govyadinov and V.A. Podolskiy. Subdiffraction light propagation in fibers with anisotropic cores. *J. Mod. Opt.*, 53:2315, 2006.

[93] J. Elser, R. Wangberg, V.A. Podolskiy, and E.E. Narimanov. Nanowire metamaterials with extreme optical anisotropy. *Appl. Phys. Lett.*, 89:261102, 2006.

[94] For details see COMSOL Multiphysics User's Guide and Electromagnetics Module User's Guide; COMSOL AB (1994-2005); www.comsol.com.

[95] A. Alu and N. Engheta. Guided modes in a waveguide filled with a pair of single-negative (sng), double-negative (dng), and/or double-positive (dps) layers. *IEEE Trans. Microwave Theory Tech.*, 52:199, 2004.

[96] Xiang Zhang and Zhaowei Liu. Superlenses to overcome the diffraction limit. *Nat. Mat.*, 7:435–441, 2008.

[97] H.A. Bethe. Theory of diffraction by small holes. *The Physical Review*, 66:163, 1944.

[98] Henri Lezec and Tineke Thio. Diffracted evanescent wave model for enhanced and suppressed optical transmission through subwavelength hole arrays. *Opt. Express*, 12:3629–3651, 2004.

[99] Yong Xie, Armis Zakharian, Jerome Moloney, and Masud Mansuripur. Transmission of light through a periodic array of slits in a thick metallic film. *Opt. Express*, 13(12):4485–4491, 2005.

[100] L Alverez and M Xiao. *J. Microsc.*, 202:351, 2000.

[101] L Alverez and M Xiao. *J. Vac. Sci. Technol. B*, 18:82, 2000.

[102] A. Roberts. *J. Opt. Soc. Am.*, 4:1970, 1987.

[103] J. A. Porto, F. J. García-Vidal, and J.B. Pendry. Transmission resonances on metallic gratings with very narrow slits. *Phys. Rev. Lett.*, 83(14):2845–2848, 1999.

[104] W. L. Barnes, W. A. Murray, J. Dintinger E., Devaux, and T. W. Ebbesen. Surface plasmon polaritons and their role in the enhanced transmission of light through periodic arrays of subwavelength holes in a metal film. *Phys. Rev. Lett.*, 92:107401, 2004.

[105] Nicolas Bonod, Stefan Enoch, Lifeng Li, Popov Evgeny, and Michel Neviere. Resonant optical transmission through thin metallic films with and without holes. *Opt. Express*, 11(5), 2003.

[106] Tineke Thio, K. M. Pellerin, R. A. Linke, H. J. Lezec, and T. W. Ebbesen. Enhanced light transmission through a single subwavelength aperture. *Opt. Lett.*, 26(24):1972–1974, 2001.

[107] T. W. Ebbesen, H. J. Lezec, H. F. Ghaemi1, T. Thio, and P. A. Wolff. Extraordinary optical transmission through sub-wavelength hole arrays. *Nature*, 391:667, 1998.

[108] H. F. Ghaemi, T. Thio, D. E. Grupp, T. W. Ebbesen, and H. J. Lezec. Surface plasmons enhance optical transmission through subwavelength holes. *Phys. Rev. B*, 58(11):6779–6782, 1998.

[109] Tae Jin Kim, Tineke Thio, T. W. Ebbesen, D. E. Grupp, and H. J. Lezec. Control of optical transmission through metals perforated with subwavelength hole arrays. *Opt. Lett.*, 24(4):256–258, 1999.

[110] Mufei Xiao and Nikifor Rakov. Enhanced optical near-field transmission through subwavelength holes randomly distributed in a thin gold film. *J. Phys. Condens. Matter*, 15:133, 2003.

[111] Cao, Qing, Lalanne, and Philippe. Negative role of surface plasmons in the transmission of metallic gratings with very narrow slits. *Phys. Rev. Lett.*, 88(5):057403, 2002.